SOVIET ATOMIC ENERGY

АТОМНАЯ ЭНЕРГИЯ
(ATOMNAYA ÉNERGIYA)

TRANSLATED FROM RUSSIAN

$\frac{c}{b}$ **CONSULTANTS BUREAU, NEW YORK**
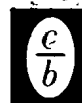
SOVIET ATOMIC ENERGY

Soviet Atomic Energy is abstracted or indexed in Chemical Abstracts, Chemical Titles, Pollution Abstracts, Science Research Abstracts, Parts A and B, Safety Science Abstracts Journal, Current Contents, Energy Research Abstracts, and Engineering Index.

SOVIET ATOMIC ENERGY

A translation of *Atomnaya Énergiya*

April, 1986

Volume 59, Number 4   October, 1985

CONTENTS

Engl./Russ.

CONTENTS

(continued)

Engl./Russ.

AN ASYMPTOTIC ESTIMATE FOR OPTIMAL REACTOR REFUELLING STRATEGY

V. D. Simonov

UDC 621.039.003

Mass production and standardization do not rule out the possibility of improvement of the technicoeconomic indicators of operating and projected generating units of nuclear power stations by improving the reactor internal fuel cycle (IFC). Even with standardized fuel enrichment and unified reactor and fuel-element design, we have a certain freedom in choosing the quantity and the composition of the fuel, which makes it possible to adapt the IFC to specific operating conditions of the various units.

Various factors, such as capital investment in power-generating units with identical reactors, the load coefficient and the load curve, or the down time associated with refuelling and equipment maintenance, may vary not only for different nuclear power stations but even within the same station. Systems with identical nuclear power stations may also be characterized by different operating conditions. Therefore, the IFC must be designed for each reactor separately, taking into considerations the specific operating features of the generating unit. If unanticipated effects are observed during reactor operation or, alternatively, anticipated effects are not observed, the IFC strategy must be adjusted in accordance with the actual situation.

In this context, it is difficult to overestimate the role of asymptotic estimates as a starting point in the search for an economically optimal IFC strategy. These estimates ensure fast orientation under conditions when we have to allow for the impact of many interdependent factors; the easiest couse is to chart a steady-state refuelling strategy and to determine the initial charge composition which is best suited for this strategy.

Asymptotic estimates clearly do not exhaust the economic performance analysis of the IFC. They are insufficient in order to arrive at a strictly optimal decision. Yet they provide the most efficient technique for identifying a bounded region of variables where the optimal strategy is located.

Let us consider the main aspects associated with the derivation of such estimates for a shell-type heterogeneous reactor with an open fuel cycle.

THE IFC ECONOMIC CRITERION

The economic indicator which enables us to assess the IFC performance is determined by the structural features of the power system in which the particular generating unit is included. For a basic-mode reactor, we can identify two cases which should rely on essentially different criteria.

1. The power system includes a sufficient number of identical units, so that when a particular unit is shut down for scheduled refuelling or maintenance, another generating unit steps in, for which refuelling or maintenance has been completed by that time. In this case, scheduled shutdown of any reactor has no effecton the contractual commitments to users or on power-generation costs. A suitable economic criterion for coordinated scheduling of generating capacity and generating conditions is therefore provided by the discounted specific power-generation costs of the various units (DSC) [1].

2. The power system is designed in such a way that capacity shortfall following the shutdown of any unit may be made up, but the cost of the alternative power is higher than the power-generation cost of the original unit. It is determined by the so-called closing power costs in the given system [2].

In this case we are actually considering the profitability of alternative ways to meet a given load schedule. A suitable criterion is the sum of discounted generating unit costs and closing costs charged for the alternative power during shutdown.

789

second
case above, but the closing costs are replaced with the penalties for failure to supply the
demand.

MODELING THE FUEL BURNUP PROCESS

IFC optimization requires a mathematical model of fuel burnup which should express the
economic indicators and the given constraints as functions of the unknown independent vari-
ables. Multidimensional programs simulating in detail the spatial processes in a reactor
will lead to an optimization algorithm of intractable complexity, thus requiring computers
of enormous power. Asymptotic solutions of optimization problems, on the other hand, can
be obtained ignoring the detailed spatial picture.

The simplest and most flexible fuel burnup model under steady-state refuelling (SSR) is
provided by the so-called model of the fuel energy potential, which is useful and efficient
for generating asymptotic solutions of IFC planning problems. The fuel energy potential
(FEP) is defined as the energy that can be generated by burning and given guel in a reactor
of actual dimensions and power output but assuming hypothetical fuel charging mode: this
hypothetical mode ensures uniform burning of all the fuel moving through the reactor, by
stipulating continuous refuelling with infinitesimal fuel charges while maintaining full
power output and infinitely fast mixing of the fuel in the reactor core.* A quantitative
measure of the FEP is provided by the fuel lifetime in a reactor with such a (reference) fuel
cycle, i.e., the time that the fuel stays in the reactor under nominal power output condi-
tions,

$$\tau_\mathrm{T}(\mathbf{x}) = W\rho_\mathrm{T}(\mathbf{x}). \tag{1}$$

Here W, days $(kg/ton)^{-1}$, is the operating time of the reactor under normal power output
needed to produce 1 kg of slag for each ton of fuel; x is a vector whose components are fuel
enrichment, fuel density, reactor power, and all other parameters which determine fuel re-
activity; ρ_T, kg/ton, is the maximum attainable slag concentration in the fuel consistent
with reactor criticality (assuming uniform fuel irradiation during the entire operating
time): it is given by the equation [3]

$$\frac{1}{\rho_\mathrm{T}} \int_0^{\rho_\mathrm{T}} k_\infty(\rho, \mathbf{x}) \, d\rho = k_\mathrm{d}(\mathbf{x}), \tag{2}$$

where k_∞ is the multiplication factor of the actual subscripts fuel lattice, whose depend-
ence on ρ may be represented in the zero-dimensional approximation; k_d is the volume-average
multiplication factor required for the realization of the designed operating conditions.

If the FEP is known, we can use the fuel burnup loss factor compared with the reference
burnup mode in order to determine that part of the FEP which is realized under discrete
charging conditions. If the loss factor is K(n) for a strategy which calls for n refuelling
during the lifetime of each fuel portion in the reactor (equal to 1/n of the total reactor
charge), then buildup of poison in the unloaded fuel under these conditions is given by

$$\rho_\mathrm{f}(n, \mathbf{x}) = \frac{\rho_\mathrm{T}(\mathbf{x})}{K(n)}; \tag{3}$$

the fuel lifetime is

$$\tau_\mathrm{f}(n, \mathbf{x}) = \frac{\tau_\mathrm{T}(\mathbf{x})}{K(n)}, \tag{4}$$

and the reactor lifetime between two consecutive refuellings (in the linear approximation)
is

$$\tau(n, \mathbf{x}) = \frac{\tau_\mathrm{T}(\mathbf{x})}{nK(n)}. \tag{5}$$

Formulas for the loss factor of a number of fuel charging modes are given in [3]. Thus,
for a reactor in which radial mixing of the fuel is performed with the same periodicity as
fuel charging, we have

---

*This fuel burning mode was first introduced by Feinberg [3].

790

$$K(n) = \frac{1}{n} + \Theta_r \left(1 - \frac{1}{n}\right),$$ (6)

and without mixing

$$K(n) = \Theta \left(1 + \frac{1}{n}\right),$$ (7)

where Θ and Θ_r are integral characteristics of spatial and radial energy distribution in the reactor, respectively (see [3]).

Relationships (1)-(7) constitute a fuel burnup model under steady-state refuelling which is known as the FEP model.

STATEMENT OF THE PROBLEM

The search for an optimal IFC strategy always involves minimizing some objective function of several constrained variables. Depending on the specific conditions for which the objective function, the constraints, and the sought parameters (the controls) are chosen, different solution methods have to be used for the problem. We will only consider asymptotice estimates of the optimal number of refuellings during a given fuel lifetime.*

We thus assume that the effect of the period preceding the attainment of SSR has a negligible effect on the choise of the refuelling strategy. We also assume that the changes in the initial reactor charge associated with SSR variation make only a small contribution to the optimization criterion and may also be ignored. Then, if z is the objective function of the problem, we seek to find n_0 such that

$$z(n_0, \mathbf{x}, \mathbf{q}) = \min z(n, \mathbf{x}, \mathbf{q})$$ (8)

subject to the constraints

$$\mathbf{x} = \text{const}, \quad \mathbf{q} = \text{const}.$$ (9)

This n_0 is the asymptotic estimate of the optimal number of refuelling under SSR, where z stands for discounted specific costs or the sum of discounted and closing costs for a generating unit with a vector which has reached the SSR mode and is fuelled by fuel with the properties x; the components of q are τ_{rf}, the length of one reactor refuelling; φ the unit load ratio (the ratio of the average power output between scheduled shutdowns to the rated power output); η, the net unit efficiency; Q, the rated reactor power; τ_a, the average scheduled maintenance time of a shutdown unit per days of operation with load ratio φ; Θ and Θ_r; p, the cost discounting factor; capital investment and operating outlays; the cost of fuel and closing energy.

OBJECTIVE FUNCTIONS

In order to solve problem (8)-(9), we have to express z as an explicit function of n, x and q . This can be done in the following way. We divide the discounted specific costs into two components,

$$3 = 3_1 + 3_2,$$

where 3_1 is the part of the discounted specific costs associated with the flow of payments for fuel charges, and 3_2 is the part attributable to all other expenditures.

In the classical framework, assuming continuous fuel charging and constant power output of the generating unit, for given fuel charges, fixed capital outlays (including the initial charge cost), and fixed operating costs (depreciation charges, maintenance costs, wages, etc.), 3_1 depends only on the efficiency of fuel utilization and 3_2 only on the rated output utilization factor of the generating unit, K_u:

$$3_1 \sim K(n);$$
$$3_2 \sim [K_u(n)]^{-1}.$$

The appropriate criterion for the second case may be written in the form

$$3 = 3_g + 3_c$$

_____
*The proposed approach may be applied to other similar problems.

791

where $3_g = 3K_w \frac{Q\eta}{p}$ are the discounted power generating costs of the unit;

$$3_c = 3_c (\varphi - K_u) \frac{Q\eta}{p}$$

are the closing power costs; 3_c is the price of closing power. We assume that the efficiency is independent of φ.

Now consider a generating unit with a reactor which is equally capable of operating of the reference mode and in the discrete mode; the reactor operating costs are assumed to be independent of n and the initial charge cost is given. The generating unit equipment is such that the unit may operate under the load $\varphi\eta Q$ for $(365 - \tau_m)$ days each year. On average, τ_m consecutive days each year are spent on scheduled equipment maintenance, so that

$$\tau_a = \frac{\tau_m}{365 - \tau_m}, \quad K_u^r = \varphi \left(1 - \frac{\tau_m}{365} \right).$$

If in the reference mode with fuel enrichment x, the DSC are

$$3^r (x) = 3_1^r (x) + 3_2^r,$$

then in the discrete mode with the same fuel and n refuellings during the fuel lifetime, assuming that τ_a and φ remain unchanged, the cost will increase to

$$3 (n, x) = 3_1^r (x) K (n) + 3_2^r \frac{K_u^r}{K_u}, \tag{10}$$

where

$$K_u = \frac{m (n, x) \tau (n, x)}{365}; \quad m (n, x) = \frac{365 + \tau_{rf}}{\frac{1}{K_u^r} \tau(n, x) + \tau_{rf}}$$

is the annual number of reactor refuellings, when one of the refuellings coincides with scheduled maintenance $(\tau_{rf} \leqslant \tau_m)$.

Substituting K(n) and τ(n, x) from (6) or (7) and (5), respectively, in expression (10), we obtain the objective function of the DSC minimization problem in explicit form.

The second objective function is written, using (10), in the form

$$3 (n, x) = \frac{Q\eta}{p} [3_1^r (x) K (n) K_u + 3_2^r K_u^r + 3_3 (\varphi - K_u)], \tag{11}$$

and the same substitutions as before reduce it to an explicit form.

OPTIMAL NUMBER OF REFUELLINGS

The condition for minimum of the functions (10) and (11) equates to zero their derivatives with respect to n. In the first case, for DSC minimization, the solution of the problem (8)-(9) has the form

$$n_0 = \sqrt{\frac{A}{\varphi\tau_{rf}} \frac{365 + \tau_{rf}}{365 - \tau_m} 3_{1,2}^r (x) \tau_r (x)}, \tag{12}$$

and in the second case

$$n_0 = \frac{A}{B(x)} \left(1 + \sqrt{1 + B (x) \left(\frac{365}{365 - \tau_m} \frac{\tau_r(x)}{AC\tau_{rf}} + 1 \right)} \right), \tag{13}$$

where $3_{1,2}^r (x) = \frac{3_1^r (x)}{3_2^r (x)}$; $B (x) = \frac{3_c}{C3_1^r (x)} - 1$; without fuel mixing, A = 1, C = Θ; with radial mixing during each refuelling, $A = \frac{2\Theta}{\Theta_r} - 1$; $C = \Theta_r$.

We often have to consider an additional constraint on fuel burnup: $\rho_f(n, x) \leqslant \hat{\rho}_f$. It determines the admissible fuel lifetime $\tau_f(n, x) \leqslant \tau_f$, the minimum attainable loss factor

792
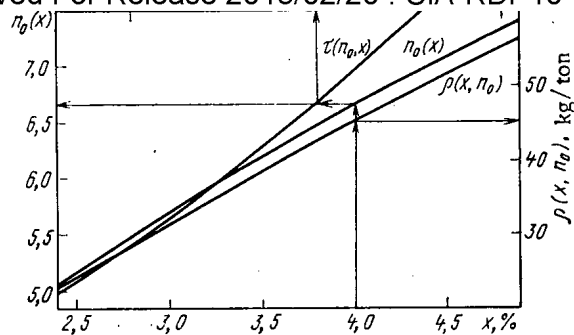
Fig. 1. Number of refuellings, reactor lifetime, and build-up of poison in the unloaded fuel vs fuel enrichment, corresponding to minimum DSC.
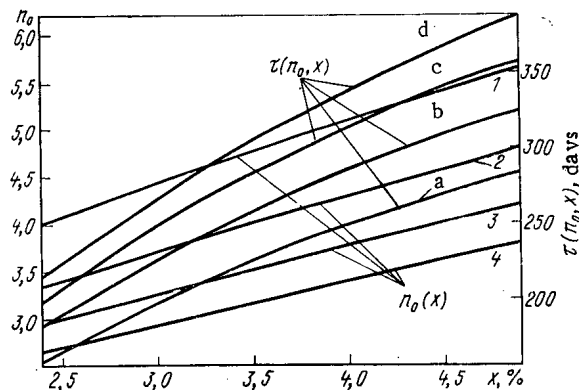
Fig. 2. Optimal number of refuellings and reactor lifetime as a function of enrichment for various closing power prices (1, 2, 3, 4 — $n_0 \cdot$ (x); a, b, c, d — $\tau(x, n_0)$ for 3_3 = 1.5, 2.0, 2.5, 3.0 kopecks/(kW-h), respectively).

$$K(\hat{\tau}_f) = \frac{\tau_r(x)}{\hat{\tau}_f},$$

and the number of refuellings corresponding to the limiting burnup,

$$\hat{n} = \hat{\tau}_f \frac{AC}{\tau_r(x) - C\hat{\tau}_f}.$$

The optimal number of refuellings during the fuel lifetime is then given by

$$n_0(\hat{\tau}_f) = \min\{n_0; \hat{n}\}.$$

NUMERICAL ESTIMATES

Let us consider some estimates for the optimal periodic charging of the VVÉR-440 reactor in SSR mode with radial fuel mixing for various fuel enrichment levels and various closing power prices.

The costs $3_{1,2}^r(x)$ and $3_1^r(x)$, entering the formulas (12) and (13) were determined from the following considerations. If a given reactor using fuel elements with enrichment x_m and subjected to n_m refuellings operates in the SSR mode for one year between refuellings

$\left[\frac{1}{\varphi}\tau(n_m, x_m) + \tau_m = 365\right]$ and both components of the DSC are known, i.e.,

$$3(n_m, x_m) = 3_1(n_m, x_m) + 3_2(x_m, n_m),$$

then under our previous assumptions we have

$$3_1(x) = \frac{\varepsilon_1(n_m, x_m)}{K(n_m)} \cdot \frac{s(x) \tau_r(x_m)}{s(x_m) \tau_r(x)};$$

$$3_{1,2}(x) = \frac{3_1^r(x)}{a_2(n_m, x_m)},$$

where $s(x)$ is the cost of fuel of enrichment x.

Following the data of [4-7], we may take $\tau_{rf} = 15$ days, $\tau_m = 35$ days, $\varphi = 0.9$, $\theta = 1.3$, $\theta_r = 1.15$; then, for $x = 3.3\%$ and $n = 3$, the DSC is 1.1 kopecks/(kW-h), and the fuel cost component is 0.3 kopecks/(kW-h).

In order to solve the equation (2), we used the numerical function $k_\infty(\rho, x)$, computed by the program UNIRASOS [6]. The fuel cost ratio $s(x)/s(x_m)$ was obtained using the classical formula for the price of enriched fuel (see, e.g., [8]), assuming 0.25% enrichment of the reprocessed fuel and taking the cost of fuel elements with 3.3% enrichment to be allocated to fabrication, acquisition of nautral uranium, and enrichment in proportions of 15%, 50%, and 35%, respectively [9].

Figure 1 can be used to determine, for a given x, the value of n_0 minimizing the DSC, the corresponding reactor lifetime $\tau(n_0, x)$, and the slag accumulation in the discharged fuel $\rho_f(x, n_0)$. For example, if $x = 3.3\%$, then $n_0 = 6$ and $\tau = 175$ days. With this refuelling strategy, after operating for 195 days with $\varphi = 0.9$ the reactor will be alternately shut down for 15 and 42 days in order to replace 1/6 of the fuel charge. The average multiyear rated power utilization factor will be 0.792, and the DSC and the specific fuel consumption will be respectively 2% and 15% less than for $n = 3$.

Calculations show that in terms of DSC, in the given range of enrichment values, it is better to perform more frequent refuellings and correspondingly to maintain shorter lifetimes than in the current practice. A lifetime of 300 days and longer is advisable for a reactor with long idle periods or with low load factors. For instance, if $x = 3.3\%$ and $\varphi = 0.9\%$, $n_0 \leqslant 3$ when $\tau_{rf} \approx \tau_m \geqslant 80$ days, i.e., $K_u \leqslant 0.7$.

Figure 2 shows how growth of 3_3 reduces n_0, making longer lifetimes more beneficial. However, for the usual VVÉR-440 fuel ($x = 2.4-3.6\%$), $\sim$300 day lifetime is advisable only if the closing costs per unit of power are quite high. Thus, if $x = 3.3\%$, then $\tau \geqslant 300$ days is economically justified only for $3_3 > 3$ kopecks/(kW-h).

CONCLUSION

The simple formula, derived for estimating the optimal number of reactor refuellings during the fuel lifetime may prove to be very useful for IFC planning. They can be used to easily estimate the effect of various factors on the refuelling strategy, such as the load factor of the generating unit, fuel costs, or shutdown time during refuelling, testing, and maintenance of equipment. The FEP model allows solving a number of other similar problems.

The conclusions based on the quantitative estimates should not be interpreted as general unambiguous recommendations. This would be contrary to the established conception of individual approach to IFC planning for each reactor.

LITERATURE CITED

1. A. G. Zakharin, V. P. Brailov, and V. I. Denisov, Methods of Economic Comparison of Alternatives in Power Engineering by the Principle of Minimum Discounted Costs [in Russian], Nauka, Moscow (1971).
2. S. L. Pruzner, A. N. Zlatopol'skii, and A. M. Nekrasov, The Economics of Power Supply in the USSR [in Russian], Vysshaya Shkola, Moscow (1978).
3. S. M. Feinberg et al., in: Proc. Second Int. Conf. on Peaceful Uses of Atomic Energy, Geneva, 1958. Papers of Soviet Scientists [in Russian], Vol. 2, Atomizdat, Moscow (19 (1959), pp. 411-533.
4. L. M. Voronin, Specific Features of Operation and Maintenance of Nuclear Power Stations [in Russian], Énergoizdat, Moscow (1981).
5. V. A. Sidorenko, Safety Issues of Water-Water Power Reactors [in Russian], Atomizdat, Moscow (1977).

6. F. Ya. Ovchinnikov et al., Operating Conditions of Water—Water Power Reactors [in Russian], Atomizdat, Moscow (1977).
7. A. A. Matveev, E. I. Ignatenko, A. P. Volkov, and B. A. Trofimov, "Organization of fuel utilization at the Kola Nuclear Power Station," At. Énerg. 51, No. 2, 87-91 (1981).
8. N. M. Sinev and B. B. Baturov, Nuclear Power Economics. Fundamentals of the Technology and Economics of Nuclear Fuel [in Russian], Atomizdat, Moscow (1980).
9. N. P. Dergachev, A. K. Kruglov, and V. M. Sedov, "Economic aspects of the development of nuclear power technology and thermal cycle installations in the USSR," At. Énerg., 43, No. 5, 365-369 (1977).

UNIFIED DRIVE MEANS OF THE CONTROLLING AND SHIELDING SYSTEM

OF RESEARCH REACTORS

I. Ya. Emel'yanov, A. N. Bakushin,   UDC 621.039.56
N. I. Galyshev. A. N. Zinkin,
and A. F. Lineva

Research reactors of various designs are employed [1, 2]: swimming pool (IRT and IVV) reactors, reactors with pressurized water (SM-2 reactors), and heavy—water (TVR) reactors These reactors are characterized by a relatively small core ($\sim$0.5-1 m), a small lattice spacing of the fuel elements, and small mass and small movement of the regulating elements; experimental channels for experiments in neutron physics, metallurgy, and other fields; frequent starts and stops because samples must be loaded or unloaded; and considerable distortions of the neutron flux distribution in the core region when the reactor is in the loaded state. Such reactors therefore require a flexible controlling and shielding system with universal means for regulating the output in automatic regulation and reactivity compensation in some combination for levelling the neutron flux and for providing the required neutron density in the test area. Since the reactor is often stopped and restarted, the reactor must satisfy increased requirements in regard to the steering of the controlling means and to radiation safety, i.e., the drive means of the controlling and shielding system must be comprehensive, must work in the automatic regulation mode, must compensate for the reactivity, and must provide emergency shielding (the drive of the controlling and shielding system must provide these functions individually and in various combinations); and fast response and precision in the movement of the regulating elements in the core must be guaranteed for performing precise experiments in neutron physics. The drive of the controlling and shielding system must be arranged on the reactor so that experimental work is not interfered with, i.e., access to the experimental channels must not be shut off.

Universal system and drive means of controlling and shielding systems could be built becasue discrete control systems with linear stepper motors were developed [3, 4]. Discrete control systems satisfy to the fullest extent the specific conditions of reactor regulation (synchronization of the operation of the regulating elements or their groups in various combinations and regulating conditions, emergency shielding of the reactor), and drive means of a controlling and shielding system with linear stepper motors meet the requirements in regard to high precision and fast response of the movement of a regulating element.

All the scientific-research work and the test designs [3] have shown that the main problem in the development of drive means with linear stepper motors is associated with the improvement of the static and dynamic quality of linear stepper motors within certain given dimensions (outer diameter of 60 mm), and $K_s = P_{max}/Q$ and $K_d = P_{max}/m$, where P_{max} denotes the greatest static force, Q denotes the mass of the motor, and m denotes the mass of the armature. The higher these coefficients, the better the design of the drive means. The design of the motor is based on the principle of longitudinal displacement of the magnetic flux along the armature with multiple armature modulation in the operational gap region. In this way excellent static characteristics of linear stepper motors can be obtained.
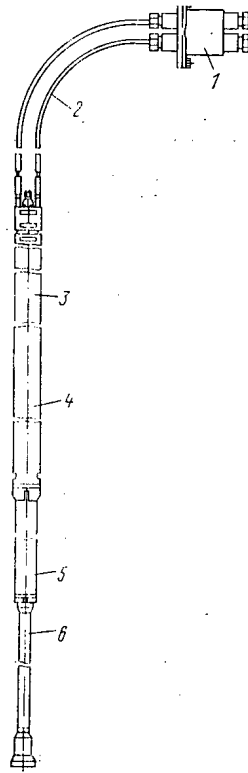
Fig. 1. Design of the drive means.
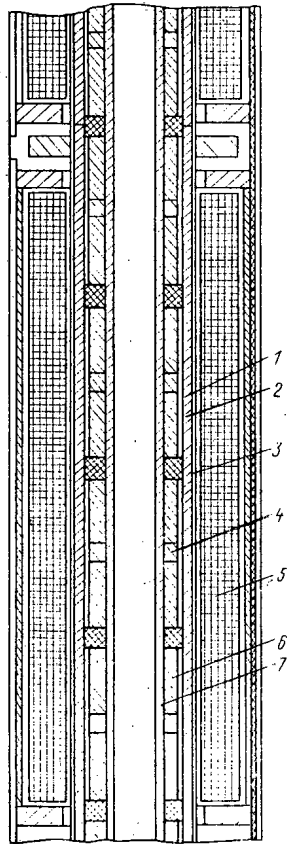
Fig. 2
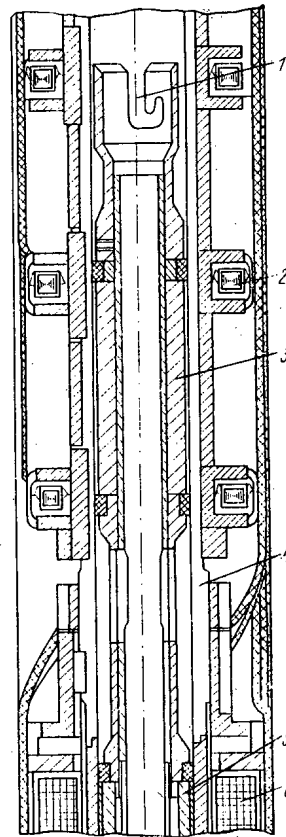
Fig. 3

Fig. 2. Design of the linear stepper motor.

Fig. 3. Linear position sensor of a regulating element.

796
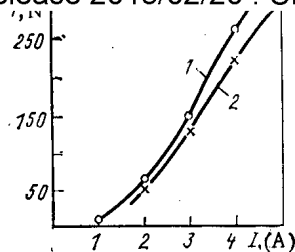
Fig. 4. Dependence of the static force P upon the current I: 1) two phases switched on; 2) one phase switched on.
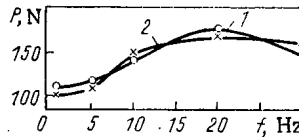
Fig. 5. Critical response of the linear stepper motor: 1) before and 2) after safe life testing.

In the case under consideration the static force is given by the formula $P_s = \Theta$ $(F_{mf}^2$, dG/dx, n), where F_{mf} denotes the magnetomotive force in the gap region; G, conductivity of the gap region of one tooth division; x, displacement of the armature; and n, number of inter-sections of the magnetic field by the operating gap.

This scheme makes it possible to use cylindrical control coils and to make better use of the stator volume. Multiple modulation of the magnetic flux requires a corresponding increase in the magnetomotive force in the gap. This can be achieved by increasing the axial length of the control coil while the outer diameter is preserved.

The step length of the movement of a regulating element and, hence, the dimensions of the tooth area are selected on the basis of the greatest admissible reactivity induced by the displacement of the element by one step [5].

When drive means with linear stepper motors are employed, conditions favorable for experiments in neutron physics are created because the induced reactivity can be determined with greater precision while the step movement of the regulating element is conserved; the use of computer technology is facilitated because in the discrete displacement of elements, the required information can be directly outputted in binary code.

The drive means (Fig. 1) comprise a linear stepper motor 4, a linear position sensor 3, regulating elements (not shown), clamping means 6, a damper 5, and flexible current leads 2 with plug-type connectors 1.

The linear stepper motor (Fig. 2) comprises housing 3 with control coils 5 of the four phases of the linear stepper motor mounted on the outer surface of the housing. Each phase of the linear stepper motor includes one control winding which is formed by one or several cylindrical coils. The pole pieces of the stator with the tooth region are inside the housing; the tooth region consists of alternating sleeves 1 and 2 of ferromagnetic and nonmagnetic steel. The tooth division of the stator is defined as $\tau = a + c$, where a and c denote the width of the sleeves of ferromagnetic and nonmagnetic material, respectively. The teeth of the stator of each of the phases of the linear stepper motor are offset relative to each other by $n\tau \pm \tau/4$, where n denotes a positive integer. Armature 7 of the linear stepper motor with the tooth region formed by a set of alternating sleeves 4 and 6 of ferromagnetic and nonmagnetic steel in analogy to sleeves 1 and 2 of the stator is mounted inside the stator. Armature 7 is flexible to compensate for possible twisting of the stator and the armature, which could influence the performance of the linear stepper motor.

A permanent magnet 3 of the linear position sensor of the regulating element is mounted on the upper end of armature 5 (Fig. 3); a cut 1 under a bayonette joint is provided for removing armature 5 from stator 6. Inductive coils 2 of the sensor are mounted on hous-ing 4 of the linear stepper motor; a signal indicating the position of the regulating ele-

797
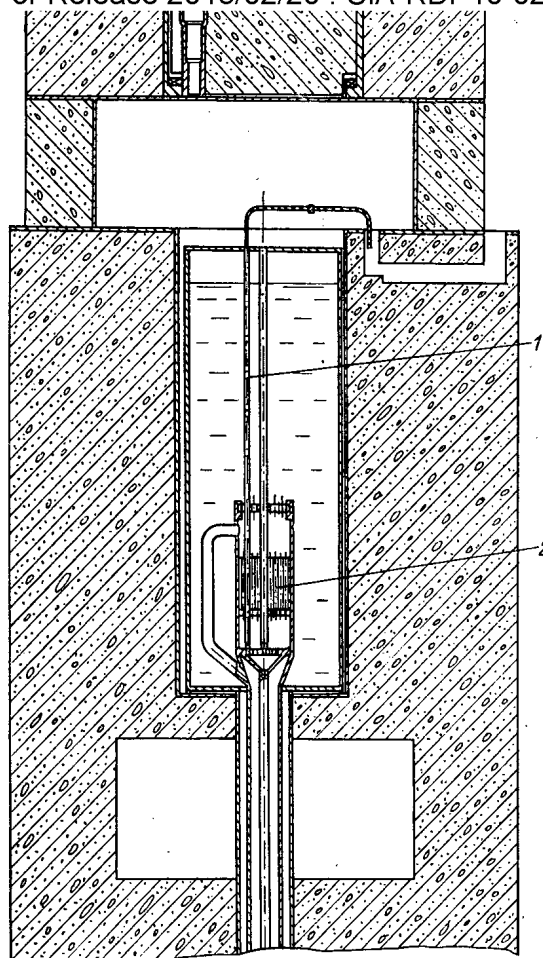
Fig. 6. Arrangement of the drive means of the controll-
ing and shielding system on the VVR-Ts research reactor:
1) drive means; 2) core.

ment is formed in those coils inside the field of permanent magnet 3. In addition, an indi-
cation of the movement of the regulating element in each step within the limits of the dis-
tance between neighboring induction coils 2 has been provided.

A collet clamp is attached to the lower end of the armature for engaging and disengag-
ing the regulating element with the armature.

A damper is provided for absorbing the kinetic energy of the moving components of the
drive means and of the regulating element.

SPECIFICATION DATA OF THE DRIVE MEANS

Step length (mm) of the armature per control pulse	2.5
Velocity (mm/sec) of the movement of the regulating element	$\leqslant 30$
Time (sec) of introducing the regulating element into the core by an emergency-shielding signal	$\leqslant 1$
Operational path length (mm) of the regulating element	600
Traction force (N)	100
Maximum diameter (mm) of the drive means	60
Length (mm) of the fixed parts of the drive means	2265
Total length (mm) of the drive means	3500
Medium for the operation of the drive means	water
Water temperature (°K)	up to 333
Water pressure (MPa)	0.098
Supply voltage (V) of the drive means:	
in braking operation	24
in shifting operation	60
Duration (msec) of a controlling pulse in shifting operation	60

798

A test version of the drive means was subjected to comprehensive tests (work-out of the individual components, investigation of the static and dynamic characteristics, thermal conditions, and safe life tests); for the test sample a controlling circuit of the linear stepper motor and other means was selected (Figs. 4 and 5). The tests have shown that the drive means are operative and that its performance corresponds to the particular requirements.

The design and the dimensions of the drive means make it possible to mount the drive on the reactor without covering the channels (Fig. 6); the flexible current leads can easily be put aside and the area above the core can be made free so that experimental work and reloading operations are not interferred with.

When some modifications are made without changing the basic design of the drive means, the drive can be used in research reactors with pressurized water.

An important advantage of the drive with the linear stepper motor results from the possibility of mounting the drive under the core. In this case the space above the core becomes fully free and experimental work and reloading operations are considerably simplified.

The scientific research work and the design tests resulted in the construction of a test sample of the drive for the controlling and shielding system. An analysis of test results of this drive shows that the new design is promising for research reactors. The investigations have helped to establish the main guidelines for a unified design of drive means with linear stepper motors. The most important points relate to the analysis of the available designs of the drive means of controlling and shielding systems built with elements of the same type; to the selection of the parameters of each type; to the construction of a system of automatic designing a unified series of drive means for controlling and shielding systems in research reactors; to the manufacture of the drive means; to testing and checking under operational conditions; and to equipping research reactors with these drive means.

LITERATURE CITED

1. G. A. Bat', A. S. Kochenov, and L. P. Kabanov, Nuclear Research Reactors [in Russian], Atomizdat, Moscow (1972).
2. S. M. Feinberg, N. A. Dollezhal', I. Ya. Emel'yanov, et al., Physical and Operational Characteristics of the SM-2 Reactor [in Russian], in: Proc. of 3rd Int. Conf. on Peaceful Uses of Atomic Energy, Geneva, 31 Aug.-9 Sept. 1964, Vol. 7, New York, pp. 384-397.
3. I. Ya. Emel'yanov, V. V. Voskoboinikov, and B. A. Maslenok, Principles of Designing Control Mechanisms of Nuclear Reactors [in Russian], Atomizdat, Moscow (1978).
4. I. Ya. Emel'yanov, V. V. Voskoboinikov, and V. P. Perfil'ev, The Automation of Nuclear Power Installations and Discrete Drive Means, At. Énerg., 33, No. 3, 735 (1972).
5. I. Ya. Emel'yanov, A. I. Efanov, and L. V. Konstantinov, Scientific-Technological Principles of the Control of Nuclear Reactors [in Russian], Énergoizdat, Moscow (1981).

INFLUENCE OF BURNING-OUT GRAPHITE IMPURITIES UPON THE PARAMETERS

OF THE RBMK-1000 REACTOR

N. V. Isaev, I. F. Moiseev,
E. M. Saprykin, V. E. Druzhinin,
and Yu. V. Shmonin

UDC 621.039.532

A correct calculation of the technicoeconomic parameters of a reactor requires knowledge of the true values of such parameters as the densities of the fuel, the coolant, and the graphite; the mass of the steel in each channel for applications; the thickness of the fuel-element casing, etc. Changes in the nuclear-physics properties of the graphite must be taken into account during the operation of the RBMK-1000 reactor. The influence of deviations of various specification parameters upon the technicoeconmic parameters of the RBMK-1000 reactor have been studied in detail in [1]. We evaluate in the present work how a change in the nuclear-physics properties of reactor graphite due to burnout of graphite impurities affects the characteristics of the RBMK-1000 reactor.

Impurities cannot be fully removed from reactor graphite during its production [2]. The impurities comprise absorbers which burnout and other absorbers which do not burnout. The ash content of reactor graphite usually amounts to a few thousandths of a percent. The typical composition of reactor-graphite impurities (B, Ca, Fe, H_2, Mn, Ti, V, and rare-earth elements) has been listed in [2]. Nitrogen which fills the pores in graphie is also a noxious admixture. The impurity composition in reactor graphite is monitored by the manufacturing plant. The total microscopic absorption cross section of reactor graphite is 4.2 mb (1 b = 10^{-28} m²). It is usually assumed in calculations of neutron physics that the microscopic absorption cross section of graphite is constant during the entire operational period of the reactor.

Figure 1 illustrates on a log scale the contribution of the various ash impurities to the effective absorption cross section of graphite when the impurities burn out during the operation of the RBMK reactor. The calculated curve (dashed line) was obtained for an average density of $8 \cdot 10^{13}$ cm⁻² · sec of thermal neutrons in graphite. The curve illustrates the dependence of the total effective microscopic absorption cross section of graphite impurities upon the time t of reactor operation:

$$\sigma_{\mathrm{C}}^{\mathrm{imp}}(t) = \sum_i \sigma_{\mathrm{C}}^{(i)} \rho_i\,(t)/\rho_{\mathrm{C}}, \tag{1}$$

where $\sigma_{\mathrm{C}}^{(i)}$ denotes the absorption cross section of the impurities contained in reactor graphite; $\rho_i(t)$, change in the nuclear density of the impurities in the course of time; and ρ_{C}, nuclear density of graphite.

The total effective microscopic absorption cross section of reactor graphite changes as follows (see Fig. 2):

$$\sigma_{\mathrm{C}}^{\mathrm{eff}}(t) = \sigma_{\mathrm{C}}^{(\mathrm{C})} + \sigma_{\mathrm{C}}^{\mathrm{imp}}(t), \tag{2}$$

where $\sigma_{\mathrm{C}}^{(\mathrm{C})}$ = 3.2 mb denotes the absorption cross section of carbon. Calculations show that after about 360 effective days of reactor operation, the $\sigma_{\mathrm{C}}^{\mathrm{eff}}(t)$ value changed from 4.2 to 3.24 mb, i.e., a radiation-induced purification of the reactor graphite from burning-out impurities is taking place. Calculations of the neutron-physical characteristics of a cell of the RBMK-1000 reactor were made with the VRM program for three types of reactor graphite; the absorption cross sections corresponding to curves 1, 2, and 3 of Fig. 2 were used.

Calculations have shown that the macroscopic cross section of a reactor cell coincides with the corresponding values of pure reactor graphite with σ_{C} = 3.24 mb for a thermal group Σ_a^2 of neutrons, once the degree of fuel burn-out E > 12.0 MW·days/kg uranium has been reached (macroscopic cross section calculated for $\sigma_{\mathrm{C}}^{\mathrm{eff}}(t)$ Fig. 3). The maximum difference of Σ_a^2 amounts to 1.2% for graphite with σ_{C} = 4.2 mb and $\sigma_{\mathrm{C}}^{\mathrm{eff}}(t)$.
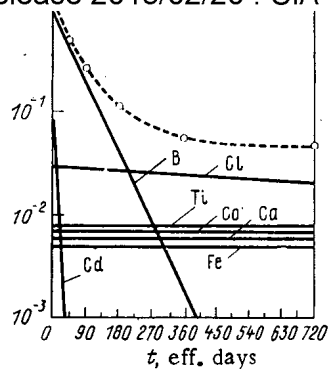
Fig. 1. Effective microscopic absorption cross section of graphite impurities as a function of the time of reactor operation and the contribution of the individual impurities; ---) sum of the contributions of the impurities.
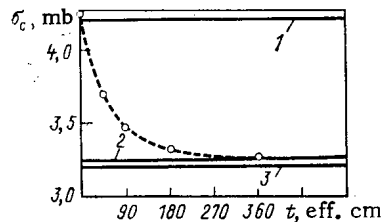
Fig. 2. Calculated dependence $\sigma_C(t)$ of reactor graphite upon t: curves 1, 2, and 3) σ_C^C = 4.2, 3.24 ("pure graphite"), and 3.2 (carbon) mb, respectively; ---) σ_C^{eff}.

The multiplication coefficient k_∞ of the neutrons in the reactor cell practically fully coincides with the values obtained for σ_C = 3.24 mb (Fig. 4) when $\sigma_C^{eff}(t)$ is used for E > 7 MW·days/kg.

In order to evaluate the influence of a change in the absorption cross section of reactor graphite upon the technicoeconomic parameters of the RBMK reactor, the REF-W program of [3] was used in the transition period of fuel loading work. A standard initial load comprising 1384 fuel elements, 234 additional absorbers, and 43 unloaded channels with a water column were assumed in the calculations. During reactor operation in the transition period, reloading of channels was considered by replacing additional absorbers (or the water column) by a fresh fuel element up to full unloading of the additional absorbers; after that, the burnt-out fuel elements were exchanged against new ones.

Calculations of the change of the average degree $E^{unl}(t)$ of the burnout of the fuel unloaded from the reactor in a transition have shown that when the burnout of impurities is taken into account in $\sigma_C^{eff}(t)$ (Fig. 5), the calculated $E^{unl}(t)$ values are greater than those obtained in the version with a constant σ_C = 4.2 mb. In the time period with t < 1600 eff. days, these $E^{unl}(t)$ values differ only slightly until the fuel elements of the initial lot are unloaded. In stationary operation of the reactor, the burnout of the graphite impurities increases the degree of burnout of unloaded fuel by about 4.7% in comparison with the calculated value which was obtained without considering the burnout of impurities.

The reloading intervals R(t) of the reactor depend upon the time of its operation (Fig. 6). The burnout of the impurities reduces R(t) in stationary operation by about 4.4% in comparison with the calculated values which were obtained with the burnout being disregarded. The shift of the curves in Fig. 6 results from changes in the time at which the unloading of additional absorbers from the reactor was terminated.

A detailed consideration of the burnout of impurities in reactor graphite has shown that the burnout reduces the calculated consumption of fuel elements in reactor recharging in the transitional mode of operation and in the stationary mode of operation. The results of calculations of the decrease in the number of fuel elements per annual reactor recharging and of the increase in the degree of burnout of the removed fuel are listed in Table 1. Calculations show that when the absorption corss section $\sigma_C^{eff}(t)$ of graphite changes relative to

801
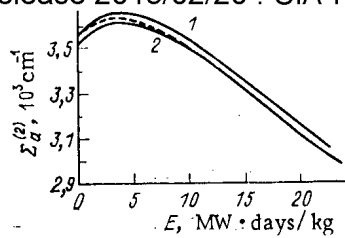
Fig. 3. Dependence of the macroscopic cross section Σ_a^2 for an RBMK-1000 reactor cell upon the fuel burnout: curves 1 and 2) σ_C = 4.2 and 3.24 mb, respectively; ---) $\sigma_C^{eff}(t)$.
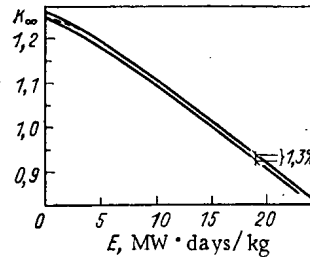
Fig. 4. Function k_∞ for an RBMK-1000 reactor cell: curves 1 and 2 refer to σ_C = 4.2 and 3.24 mb, respectively; ---) $\sigma_C^{eff}(t)$.
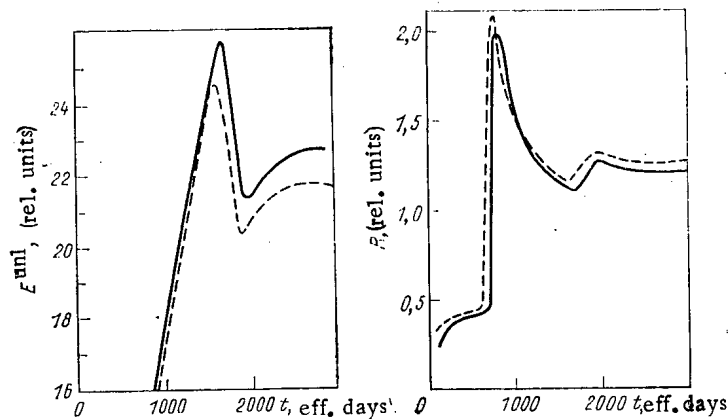
Fig. 5   Fig. 6

Fig. 5. Change in the degree of burnout of un-loaded fuel for various σ_C values: ---) σ_C = 4.2 mb and ——) $\sigma_C^{eff}(t)$.

Fig. 6. Time dependence of the recharging periods of the reactor for various σ_C values: ---) σ_C = 4.2 mb and ——) $\sigma_C^{eff}(t)$. .

σ_C = 4.2 mb, the fuel consumption in reactor make-up is reduced by 16 fresh fuel elements per year and the dgree of burnout of the unloaded fuel is increased by 0.95 MW·days/kg.

    Taking into account the change in $\sigma_C^{eff}(t)$ implies a correction of the effective coefficient k_{eff} of neutron multiplication in the reactor. The practice of calculating real critical reactor states involved the BOKR-BIS program [4] and has shown that in the initial period, after the start-up of the reactor, the k_{eff}^{calc} value is close to 1 and thereafter, the difference increases sharply and reaches (0.5-1.0%). We may assume that one of the systematic errors of the computational model originates from disregarding the burn-out of absorbers in graphite. When the real burnout of impurities in reactor graphite is taken into account, an increased k_{eff}^{calc} value is obtained with the BOKR-BIS program. The difference between the calculated k_{eff} value and the critical value in the transition period is reduced to ±(0.1-0.4)%. For example, a calculation made with the BOKR-BIS program for the critical state of the reactor of the first block of the Smolensk Atomic Power Station on December 12, 1984,

802

TABLE 1. Change in the Reactor Parameters

Parameter	Time (years) from the start of reactor operation									
	1	2	3	4	5	6	7	8	9	10
Decrease in the number of fuel elements	1	2	56	7	5	12	25	12	13	16
Increase in E^{unl} (MW·days/kg uranium)	–	–	0,39	0,16	0,20	0,73	1,58	0,36	0,80	0,95

renders the following values: k_{eff} = 0.99243 (when the burnout of the impurities is disregarded) and k_{eff} = 1.00327 (when the burnout of the impurities is taken into account).

It was known earlier that the calculations of the RBMK-1000 reactor are not free of systematic errors. The authors of [5] have corrected the energy output E_j of the fuel in their attempts to reduce the difference between the channel outputs obtained by calculations with the BOKR-BIS program and the channel outputs determined with the central monitoring system "Skala;" the authors of [5] tried to reduce the difference by correcting the energy E_j released from the fuel. It was shown that coinciding output values of the channels make it necessary to correct within 5% limits the E_j value calculated in the central monitoring system; this involves mianly on increase in E_j. But the authors of [5] have not given a proper explanation of the reasons for the discrepancies resulting from the calculations of the output and the energy liberation. Calculations of $E^{unl}(t)$ show (see Fig. 5) that the $\sigma_c^{eff}(t)$ values are corrected when changes in the absorption of graphite are brought into account. The corrections of the E_j values are within the regulation range indicated in [5], can be clearly explained in terms of physics, and help to increase the accuracy of neutron-physical calculations.

Owing to the high nuclear density of graphite and the large capture cross section of the burning-out absorbing impurities, the thousandths-of-a-percent components importantly influence the precision of neutron-physical calculations and the parameters of the RBMK-1000 reactor. A change in the composition of impurities in the reactor graphite by burnout implies a change in the macroscopic absorption cross section for thermal neutrons by about 1.2% in an RBMK-1000 cell. This change is the reason for the systematic error in the earlier calculations in which the burnout of impurities was disregarded. By taking into account the burnout which occurs during the operation of the RBMK-1000, the performance parameters of the RBMK-1000 reactor is actually higher by 4.7%, the recharging periods are reduced by 4.4%, and the fuel consumption is smaller by 4.4% in comparison with the previously accepted calculated values.

LITERATURE CITED

1. N. A. Dollezhal' and I. Ya. Emel'yanov, Channel-Type Nuclear Power Reactors [in Russian], Atomizdat, Moscow (1980), p. 36.
2. V. V. Goncharov, N. S. Burdakov, Yu. S. Virgil'ev, et al., The Effect of Irradiation upon the Graphite of Nuclear Reactors [in Russian], Atomizdat, Moscow (1978), pp. 23-27.
3. V. S. Romanenko and A. V. Krayushkin, "Computational Investigations of the Physical Properties of the RBMK Reactor in the Transition Period," At. Énerg., 53, No. 6, 367 (1982).
4. A. A. Shkurpelov, V. P. Borshchev, V. P. Veselov, et al., "The BOKR-BIS Program for the Two-Dimensional Calculation of the RBMK on an ES Series Computer," At. Énerg., 50, No. 5, 352 (1981).
5. A. A. Shkurpelov, N. V. Isaev, and A. S. Nerimov, "Correction of the Macroscopic Cross Sections by Increasing the Precision of the Parameters of the RBMK Charge," At. Énerg., 50, No. 1, 6 (1981).

803

LOCAL DISTRIBUTION OF THE COOLANT FLOW RATE IN FUEL
ASSEMBLIES WITH A BLOCKED FLOW-THROUGH SECTION

L. Sabotinov, I. Iordanov,
N. Antonov, K. Popesku,
and A. Buzhor

UDC 621.039.5

One of the basic methods of thermohydraulic analysis of fuel assemblies in nuclear reactors is the method of lumped parameters. In this method the total throughput cross section is divided into subchannels, for which the average values of the thermohydraulic parameters of the coolant are calculated. The equations of conservation of momentum in the axial and transverse directions are written down separately, which simplifies the equation of conservation of momentum in the transverse direction. The RAPREF program for fast analysis of the thermohydraulic processes in arrays of fuel elements was developed based on this method [1, 2].

TRANSPORT PROCESSES BETWEEN SUBCHANNELS

The geometrical structure of the fuel assembly and the parameters of the process determine the nonuniform distribution of the coolant flow rate in the subchannels. The change in the circular velocity around the fuel cell, the unequal pressure losses, and the change in the throughput cross section owing to the spiral winding determine the transport processes occurring between subchannels. These processes depend on the structure of the fuel-element array and on the flow conditions [3].

The model on which the RAPREF program is based took into account the following transport processes [4]: turbulent transport, transverse heat conduction, and forced mixing.

Turbulent transport is the resultant force of turbulent diffusion between neighboring subchannels and does not cause redistribution of the coolant flow rate. The transverse flow rate of the coolant accompanying turbulent transport is determined by the formula

$$M_{ij,\,T} = m_{lj,\,T}\,\Delta z = c_T\,\frac{m_{z,i}+m_{z,j}}{A_{z,i}+A_{z,j}}\,S\Delta z, \tag{1}$$

where c_T is the coefficient of mixing; $m_{ij,\,T}$, transverse turbulent flow rate of the coolant per unit lenght; m_c, axial flow rate of the coolant; A_c, axial throughput cross section; S, width of the throughput cross section at the boundary between subchannels; and Δz, axial distance over which the interaction of the diffusion processes is evaluated. The coefficient of mixing is determined by the following dependences:

$$c_T = \text{const}; \tag{2}$$

$$c_T = \text{const } \text{Re}^{\text{const-1}}; \tag{3}$$

$$c_T = \text{const } \text{Re}^{\text{const-1}}\,D_E/S; \tag{4}$$

$$c_T = \text{const } \text{Re}^{\text{const-1}}D_E/z_{IJ}, \tag{5}$$

where Re is Reynolds number; D_E is the average hydraulic diameter of the interacting subchannels i and j; z_{IJ} is the distance between the centers of the subchannels. For sodium-cooled fuel assemblies const = 0.002-0.005 and const-1 = 0.2.

Transverse Heat Conduction between Subchannels Determined by the Thermal Conductivity of Sodium. The heat flux owing to the conduction between two neighboring subchannels is determined by the relation

$$\Delta q_{ij,c} = F_s \hat{K}\,(T_i - T_j), \tag{6}$$
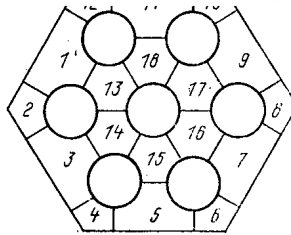
Fig. 1. Fuel assembly with seven rods and 18 sub-channels: 1, 3, 5, 7, 9, 11) lateral subchannel; 2, 4, 6, 8, 10, 12) corner subchannels; 13, 14, 15-18) central subchannels.

where F_s is the shape factor; $\hat{K}$, average thermal conductivity in subchannels i and j; and T_i and T_j, temperatures in the two subchannels.

The following expressions can be used for the shape factor:

$$F_s = 1.38 \, (S/D_F)^{0.674}; \tag{7}$$

$$F_s = S k_g/z_{IJ}, \tag{8}$$

where D_F is the outer diameter of the fuel element; K_g is a geometric factor whose values are determined by the type of interacting subchannels (central—central, central—lateral, lateral—corner). The average value recommended for the interaction of two central subchannels is 1.5.

Forced mixing is brought about by the peculiarities of the spiral winding, which are responsible for the predominant flow of liquid in a definite direction. The spiral winding substantially changes the velocity field and produces the following effects:

— increases the level of turbulence and turbulent transport, which is described by Eq. (1), in which c_T is given in the input data, depending on the type of interacting subchannel; and

— orients the motion of the coolant between neighboring subchannels, in a direction determined by the direction of the spiral winding and its pitch:

$$M_{ij, \, D} = m_{ij, \, D} \Delta z = \frac{1}{2} K_D S \, (\rho_i + \rho_j) \, \Delta z w_{ij}. \tag{9}$$

Here K_D is a coefficient with different values depending on the type of interacting subchannels, having the same distribution as c_T; ρ is the density of the coolant; and, w_{ij} is the velocity of the directed overflow.

The value of w_{ij} depends on the average axial velocity and on the tangent angle Θ between the main orientation of the throughput section and the local direction of winding:

$$w_{ij} = TAB\pi \, \frac{D_F + D_w}{P_w} \, \pi, \tag{10}$$

where $TAB = w_{ij}/(\hat{U} \tan \Theta)$ and is inserted into the input data for axial and radial configurations and subchannels; and P_w, D_w are the pitch and diameter of the winding.

The axial motion of the spiral winding changes the throughput section and leads, in its turn, to important effects. The indicated transport processes are included in the conservation equations describing the thermohydraulic parameters of the sodium coolant at each point. To complete the description of the characteristics of the fuel assembly the conservation equations for the coolant are supplemented by an equation of heat conduction in the fuel, which describes the distribution of the temperature field in the fuel elements.

CONSERVATION EQUATIONS FOR THE COOLANT

In deriving the conservation equations, a rectangular control volume is studied. Here the change in the throughput section in the axial direction with a constant flow rate in the transverse direction is taken into account.

805
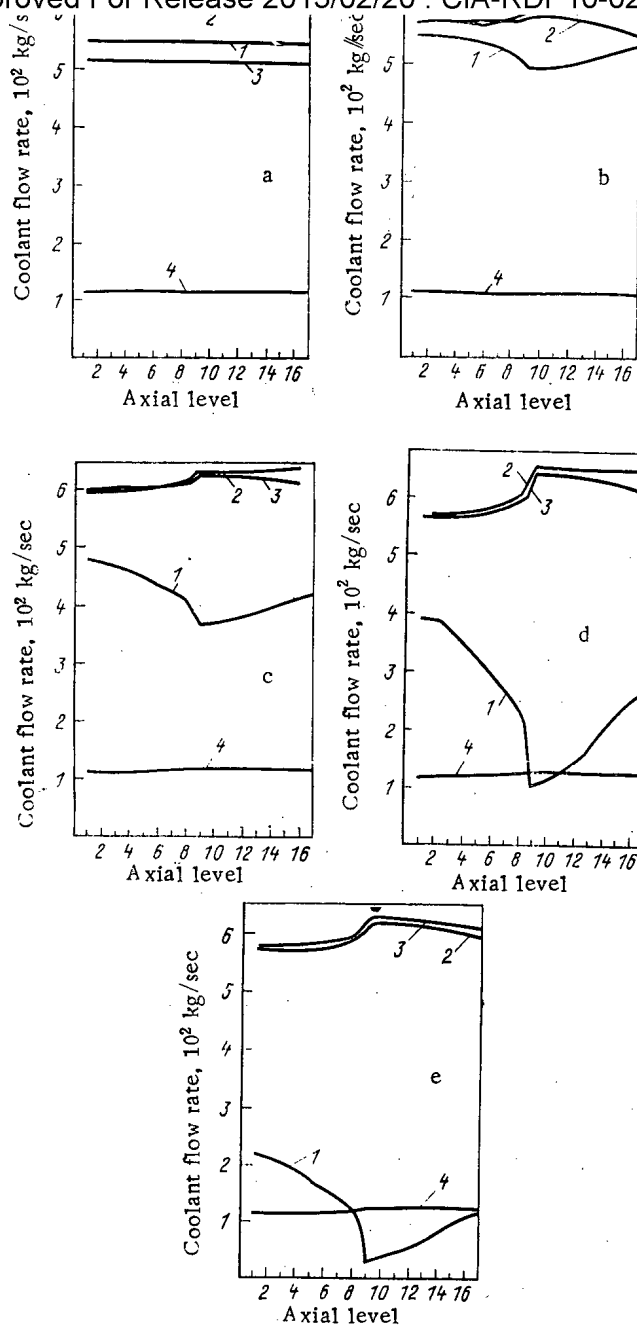
Fig. 2. Axial distribution of the coolant
flow rate with R_b = 0.9 (a), 0.7 (b), 0.5
(c), 0.3 (d), 0.2 (e): 1) subchannel 17; 2)
subchannel 16, 3) subchannel 18; 4) subchan-
nel 9.

Equation of Conservation of Mass

$$\frac{\partial m_z}{\partial z} = -\sum_{j=1}^{N} \overline{m}_{ij},$$ (11)

where $\overline{m}_{ij}$ is the transverse flow rate of the coolant per unit length in neighboring sub-
channels and z is the axial direction of the flow.

Relation (11) is used in the RAPREF program at each axial level L + 1 in the form

806
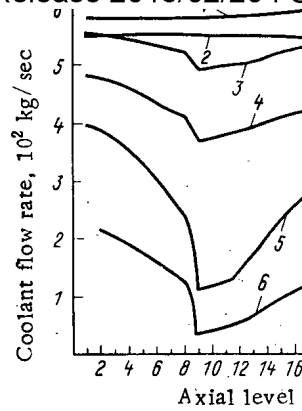
Fig. 3. Axial distribution of the coolant flow rate in the subchannel 17 with the blocking ratio $R_b = 1$ (1), 0.9 (2), 0.7 (3), 0.5 (4), 0.3 (5), 0.2 (6).

$$m_{zi}|_{L+1} = m_{zi}|_L - \sum_{j=1}^{N} (m_{ij,\,D} + m_{ij,\,P})\, \Delta z \tag{12}$$

($m_{ij,\,P}$ is the transverse flow rate of the coolant per unit length owing to the difference in the pressure between the subchannels).

Equation of Conservation of Energy

$$\frac{m_z}{A_z}\,\frac{\partial \bar{h}}{\partial z} = \frac{1}{A_z} \sum_{j=1}^{N} \left[\hat{K}\,\frac{S}{\Delta x_j}\,(\bar{T}_j - \bar{T}_i) + (\bar{m}_{ij} + m_{ij,\,T}C'_{ij})\,(\bar{h}_i - \bar{h}_j) \right] + q''' - \frac{g'_d}{A_d}, \tag{13}$$

where h is the enthalpy; q''', density of the power; q'_d, linear heat loss by the fuel assembly walls; A_d, area of the transverse cross section of the fuel assembly walls; x_k, direction transverse to the direction z, to which the values of the velocity and the area A_k correspond; and, C_{ij}, flow rate of the mixed turbulent flow. The coefficient C'_{ij} expresses the difference between the transverse turbulent transport of energy and momentum.

In the program the relation (13) is written in the following discrete form:

$$h_i|_{L+1} = h_i|_L + \left\{ \Delta z \sum_{j=1}^{N} \left[\hat{K}F_s\,(T_j - T_i) + \frac{1}{2} \times \right. \right.$$
$$\times (m_{ij} - |m_{ij}|)\,(h_i - h_j) + a_1 m_{ij,\,T}\,(h_i - h_j) \Big]_L +$$
$$\left. + \Delta z \overline{A}_{zi} \left(q''_i \Big|_{L+1/2} - \frac{1}{A_D}\,\delta_1 q'_d \Big|_L \right) \right\}/m_{zi}|_{L+1}, \tag{14}$$

where δ_1 is a parameter which assumes the value 1 for subchannels adjacent to the fuel assembly walls and the value 0 for other subchannels.

Since the values of $m_{ij,\,T}$ and c'_{ij} cannot be obtained with the help of measurements, their sum was replaced by the product $a_1 m_{ij,\,T}$, where the constant a_1 is close to 1.

Equation of Conservation of Momentum in the Axial Direction

$$\frac{\partial \bar{p} A_z}{\partial z} = \sum_{j=1}^{N} [\bar{m}_{ij} w^* - (\bar{m}_{ij} + m_{ij,\,T})\,(w_i - w_j)] - \bar{\rho} g - \left(\frac{m_z}{A_z}\right)^2 \left[\frac{f}{2D\rho} + \frac{K}{2\rho\Delta z} + \left(\frac{A_z}{A_z}\right)\frac{\partial}{\partial z}\left(\frac{1}{\rho}\right) - \frac{1}{\bar{\rho} A_z}\,\frac{\partial A_z}{\partial z} \right], \tag{15}$$

where p is the pressure of the liquid; w*, relative velocity, which can be defined as the velocity in the donor subchannel, the velocity in the acceptor subchannel, or as their combination; w, axial velocity; g, acceleration of gravity; f, friction coefficient; D, hydraulic equivalent diameter; and K, local pressure-drop factor.

807

TABLE 1. Radial Temperature Field at the Outlet from the Fuel Assembly for Different Values of R_b

R_b	Subchannels								
	1	2	3	4	5	6	7	8	9
0	351,10	369,41	339,72	367,72	345,73	368,00	338,00	367,00	345,27
0,1	351,13	368,99	339,73	367,61	345,72	367,99	338,24	367,02	345,28
0,3	351,06	368,61	339,52	366,75	345,53	366,75	338,29	365,92	345,67
0,5	351,19	367,59	339,56	366,34	345,85	366,32	338,32	366,14	346,92
0,7	351,22	367,69	339,67	366,52	345,81	366,42	338,70	367,46	350,16
0,8	351,26	367,70	339,68	366,53	345,86	366,44	339,09	368,40	353,27

R_b	Subchannels								
	10	11	12	13	14	15	16	17	18
0	350,41	342,95	352,26	402,16	402,11	399,18	380,81	399,61	392,13
0,1	350,29	342,97	351,37	401,58	402,55	399,22	380,63	400,03	391,96
0,3	350,47	343,05	352,24	401,96	400,97	399,64	382,28	405,97	393,82
0,5	350,34	343,12	351,21	402,32	401,77	400,62	383,75	420,77	395,32
0,7	351,59	343,44	351,27	403,12	402,52	401,11	389,27	453,22	400,34
0,8	352,61	343,79	351,32	404,04	402,63	402,04	394,61	479,25	405,57

Equation (15) is used in the program in each axial step in the form

$$p_i|_{L+1} = p_c|_L A_R + \sum_{j=1}^{N} \{[m_{ij}(1.5\,w_i - 0.5\,w_j) - m_{ij,\tau}(w_i - w_j)]\ A_R/A_{z,i}\}\Delta z - \Delta z g A_R \overline{A}_{zi}(\rho_i|_L +$$

$$+ \rho_i|_{L+1})/2A_{z,i}|_L - \frac{[(\rho_i w_i)_L + (\rho_i w_i)_{L+1}]^2}{2(\rho_{i,L} + \rho_{i,L+1})}\left[\frac{F_1}{2}\frac{\overline{A}_{zi}}{A_{zi}}A_R + \frac{\rho_{iL} - \rho_{i,L+1}}{\rho_{i,L+1}}A_R - A_R(1 - A_R)\right], \qquad (16)$$

where

$$F_1 = \frac{f}{D}\Delta z + K_{i,z};$$

$$A_R = A_{z,L+1}/A_{z,L}.$$

Equation of Conservation of Momentum in the Transverse Direction

To derive the equation of conservation of momentum in the transverse direction we shall study two neighboring subchannels. We write the equation in the general form

$$\frac{\partial \rho U_h^2 \Delta_k}{\partial x_h}\Delta x_h + \frac{\partial \rho U_h w A_z}{\partial z}\Delta z = -A_h\frac{\partial p}{\partial x_h} + F_{xh}, \qquad (17)$$

(F_{xk} is the surface force in the transverse direction).

Equating the values of the terms we obtain

$$A_k\frac{\partial p}{\partial x_k} = F_{xk}. \qquad (18)$$

The surface force in the transverse direction is related to the coefficient of resistance k in the transverse section by the relation

$$F_{xj} = -\frac{k|m_{ij}|m_{ij}}{2\rho S^2 \Delta x_j}V. \qquad (19)$$

The equation of conservation of the transverse momentum was used in the program in each axial segment Δz in the form

$$m_{ij}|m_{ij}| = \frac{2\rho_{i,L}(P_i - P_j)}{k}S^2\Delta z^2. \qquad (20)$$

808
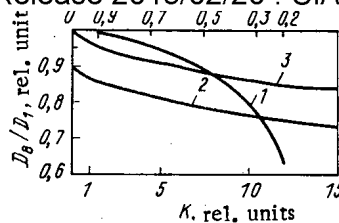
Fig. 4. Dependence of the blocking section on the local pressure drop factor: 1) $D_8/D_1 = f(R_b)$; 2) $D_8/D_1 = f(K) - R_b = 0.5$; 3) $D_8/D_1 = f(K) - R_b = 1$.

The pressure drop is the boundary condition used in the program. The values of the temperature, pressure, and input density of the coolant are assumed to be known for all subchannels.

To obtain the condition of uniform pressure at the outlet the velocities of the coolant at the inlet for all subchannels are determined by iteration. The parameters of the coolant in all subchannels are determined at the same time with the help of the equations describing the state of the coolant in successive axial sections, beginning at the inlet.

The velocities at the inlet are first assumed to be known and are then determined by the method of iteration. The transverse flow rates are calculated based on the properties of the coolant at the inlet to each axial segment. Knowing the transverse flow rates of the coolant in one segment and the heat flux it is possible to determine the enthalpy, the density, the pressure drop, and the velocity at the outlet from the segment. To take into account the effect of the local pressure loss on the properties of the coolant the method of iteration is applied to each axial segment.

EVALUATION OF THE EFFECTS ACCOMPANYING LOCAL BLOCKING

OF THE THROUGHPUT SECTION

During operation the structure of the rod bundle can deviate from the nominal structure because of local changes brough about by the block ing of the throughput cross section. For rod assemblies with a partially blocked throughput section the redistribution of the coolant flow between subchannels, which changes the temperature field, depends on a number of factors [3, 5]:

— the blocking ratio R_b, defined as the ratio of the cross section of the blocked zone to the nominal throughput section of the subchannel.

— change in the physical properties of sodium as a function of the temperature;

— the local pressure drop factor for the blocked zone [K in Eq. (15)]; and,

— the coefficient of resistance in the transverse throughput section [k in Eq. (19)].

The RAPREF program enables carrying out only an analysis of partial blocking of the throughput section of one subchannel up to a minimum value $R_b = 0.16-0.15$. To estimate the effects accompanying local blocking of the throughput section, a calculation was performed for an array consisting of seven fuel cells with the following characteristics:

Total axial length, mm	710
Outer diameter of the fuel cell, mm	6.8
Outer diameter of the fuel cell tablet, mm	6.0
Thermal resistance of the fuel jacket, $m^2 \cdot C/W$	$1.76 \cdot 10^{-4}$
Step between fuel elements, mm	8.3
Distance from the lateral fuel cells to the wall of the fuel assembly, mm	1.5
Local Pressure drop (at the inlet and outlet from the fuel assembly)	0
Total flow rate of the coolant in the fuel assembly, kg/sec	1.24

809

sure Loss Factor K in the Blocking Zones of
Subchannel 17 with R_b = 0.5

Charac-teristic	K				
	0	1	5	10	15
D_1, kg/sec	0,04385	0,03844	0,03075	0,02562	0,02322
T_e, °C	420,77	432,13	444,60	457,55	461,48
D_8/D_1	0,896	0,864	0,809	0,758	0,727

Note. T_e) temperature at the outlet from the
subchannel; D_8) axial flow rate of the coolant
in the blocking section; D_1) flow rate of the
coolant at the outlet in the subchannel.

The axial and radial distribution of the heat liberation is uniform.

Seventeen axial sections with the following markers (in mm) were used in the calculation: 0—76—152—216—267—318—368—406—419—432—444—470—508—559—610—660—710. The calculations were performed for zero and linear (200 W/cm) heat fluxes at a temperature of 300°C at the inlet. The calculation was also performed for fuel elements without spiral winding. Figure 1 shows a diagram consisting of 18 working subchannels. The parameters in subchannel 17 and in the axial section 8 (406 mm) were analzyed.

RESULTS

Change in the Blocking Ratio. In order to clarify the effects caused exclusively by a change in the value of the blocking ratio, in the analysis we ignored effects arising from turbulent tranposrt between subchannels (we correspondingly used the constants at the outlet) as well as effects arising from the temperature dependence of the properties of the materials (we assumed that the heat flux was equal to zero).

We assumed that the throughput cross section of subchannel 17 in axial section 8 was equal to 90, 70, 50, 30, and 20% of the nominal value; the value of the blocking ratio R_b was equal to 0.9, 0.7, 0.5, 0.3, and 0.2, respectively.

The coefficient of resistance in the transverse direction (0.5), the local pressure drop factors at the inlet and outlet from the fuel assembly (equal to zero), and the geometrical factor for the transverse conductivity remained constant in all cases. The local pressure loss factor in the blocking zone was assumed to be equal to zero.

The results obtained for the axial distribution of the coolant flow rate are presented in Figs. 2 and 3. In addition to the subchannel 17, the figures also show the subchannels with which they directly interact. The change in the blocking ratio leads to the following effects.

1. Change in the axial distribution of the coolant flow rate. For R_b = 1 the axial flow rate of the coolant remains practically constant in subchannel 17 as well in subchannels 9, 16, and 18. When the value of r_b is lowered, the coolant flow rate in subchannel 17 in the section before the blocking zone decreases slowly, and in the blocking zone itself it decreases substantially, after which it increases along the channel, approaching its starting value. The lower the value of R_b, the larger this effect is. Thus for R_b = 0.7 the coolant flow rate in the blocking zone decreases by 10% relative to the value at the inlet, reaching 84.5% for R_b = 0.2. The axial flow rate in neighboring subchannels 9, 16, and 18 increases slowly on the section up to the blocking zone as R_b decreases, it is maximum in the blocking zone, and then it decreases slowly up to the starting values.

2. Change in the distribution of the coolant flow rate at the inlet. As the value of R_b is lowered, the absolute value of the coolant flow rate in subchannel 17 decreases. When the blocking ratio changes from 1 to 0.2 the coolant flow rate at the inlet decreases from 0.0577 kg/sec to 0.0216 kg/sec, i.e., to 37.4% of the starting value. The combined action of these two effects lowers the axial flow rate of the coolant in the blocking zone by 94.2% when R_b is lowered from 10 to 0.2.

810

3. Pressure drop in the blocking zone, which substantially increases when R_b is lowered. The following values of Δp between the levels 7 and 9 in bar (1 bar = 10^5 Pa) were obtained for R_b = 1, 0.9, 0.7, 0.5, 0.3, and 0.2: 0.036; 0.042; 0.095; 0.252; 0.447, 0.476, respectively.

Change in the Heat Flux. The effect of a nonzero heat flux can be studied from two viewpoints:

a) its effect on the change in the axial distribution of the coolant flow rate at the inlet into a subchannel and the pressure drop in the blocking zone owing to a change in the properties of the liquid as a function of the temperature can be studied for the same value of the blocking ratio.

For the conditions of subchannel 9, with a coefficient of resistance in the transverse direction equal to 10^6 and R_b = 0.5, the results of the calculations show that or change in the heat flux from 0 to 200 W/cm, raising the temperature at the outlet in subchannel 17 from 300°C to 420.77°C, does not appreciably affect the axial distribution of the coolant flow rate as well as its flow rate at the inlet to the subchannel and the pressure drop in the blocking zone. The ratio of the coolant flow rate in section 8 to the coolant flow rate at the inlet to the subchannel changes by less than 1%. The local drop in the pressure Δp_7 changes approximately by 1%. The coolant flow rate at the inlet to the subchannel changes by less than 1%.

b) The change in the radial temperature field at the outlet from the fuel assembly can be studied. It follows from Table 1 that when R_b is lowered from 1 to 0.2, the temperature in subchannel 17 changes most (from 400°C to approximately 480°C).

Change in the Local Pressure Drop Factor in the Blocking Zone. The effect of the local pressure drop in the blocking zone, which affects the equation of conservation of momentum in the axial direction, was evaluated in the range 0-15 when the cross section decreased by 50%. An increase in the local pressure drop factor in the blocking zone produces the same qualitative effects in the axial distribution of the coolant flow rate and the distribution of the coolant flow rate at the inlet to the subchannel as does a change of the blocking ratio, but with a different "weight" (Table 2). Under conditions for which K = 0 and R_b = 0.9; 0.7; 0.5; 0.3; 0.2, the following values of D_8/D_1 where obtained: 0.9913; 0.9514; 0.8906; 0.7783; 0.6466, respectively.

It follows from Fig. 4 that the decrease in the cross section can be imitated exclusively by a change in the local pressure drop factor (a technique used in the COBRA programs) in the blocking zone.

Effect of the Coefficient of Resistance in the Transverse Direction. An increase in the coefficient of resistance in the transverse direction decreases the coolant flow rate at the inlet to the subchannel, the ratio of the coolant flow rate in the blocking zone to the coolant flow rate at the inlet, and the pressure drop. Thus increasing the coefficient of resistance in the transverse direction from 0.5 to 10^6 for R_b = 0.5 lowers the coolant flow rate at the inlet in subchannel 17 by 7.67% (0.0439/0.475) and lowers the ratio of the coolant flow rate in the blocking zone to the coolant flow rate at the inlet from 0.867 to 0.595, and the pressure drop decreases from 0.251 to 0.241 bar.

MAIN RESULTS

When the throughput section is blocked, the change in the blocking parameters gives rise to the following important effects.

A drop in the blocking ratio lowers the axial coolant flow rate in the block zone, lowers the coolant flow rate at the inlet into the zone, and increases the pressure drop in the zone.

A change in the intensity of the heat source does not affect the local coolant flow rate in the blocked zone or the flow rate at the inlet to the subchannel or the local pressure drop, but it substantially increases the temperature at the outlet from the blocked subchannel, proportionally to the decrease in the blocking ratio.

An increase in the local pressure drop factor in the blocked zone produces the same qualitative effects as a decrease in the blocking ratio, but only when R_b > 0.35-0.40.

811

1. R. Moeller, H. Tschoeke, and M. Kolodjiej, "Experimentelle Betimmung von Temperaturfur- feldern in natriumdurchstroemten Bundelm nit hexagonaler Stabanordung und gitterfoermin- gen Abstandhaltern," KFK 2356, January, 1977.
2. G. Straub, "Berechnung der Temperatur und Geschwindigkeitsfeler in parallel angestroem- ten Brennstabbuendeln Schneller natriumgekuehlter Brutreaktoren (ARTIS-Code)," Disserta- tion an der TU-Stuttgart (1976).
3. J. Creer, J. Bates, and A. Sutey, "Turbulent flow in a model nuclear fuel rod bundle con- taining partial flow blockages," Nucl. Eng. Design, 52, 15-33 (1979).
4. M. Kazimi, "Heat transfer correlation for analysis of CRBP assemblies," LRA-74-114 (1974).
5. F. Mantlic et al., "Obzor teplofiziceskih isledovanii sborkov tvelov s ceasticunoi blokirovoi prohodnih secenii," UJV 6057-T, ŘEŽ (1982).

USE OF SAMPLE RECOGNITION METHODS FOR DETECTING CURRENTS

IN STEAM GENERATORS

V. V. Golushko, V. S. Dunaev,   UDC 62-506:621.391.193
and A. B. Muralev

The operational detection of currents in steam generators working with sodium, the water of fast reactors, is an important problem. Acoustic detection is one of the promising and almost inertialess methods. When acoustic sensors are employed, the signals are usually nonstationary, random signals at the moment of flow initiation and are almost stationary sig- nals when the background is recorded. Investigations of these processes make it possible to develop an algorithm for the detection of flow signals (which below will be termed "the effect") on the background of acoustic noise generated by the steam generator in its opera- tion. The final goal of the investigations is to create a rather simple and reliable instru- ment, a flow detector. Therefore, when methods for the initial data evaluation are selected, the complexity of the actual technical embodiment is taken into consideration by the develop- ment of a decision rule.

The present work reports on an attempt of employing the techniques of the theory of sample recognition [1-3] in the analysis of signals obtained in an experiment in which cur- rents were simulated by argon in a working module of a steam generator; the signals were recorded on magnetic tape. Experiments were made in a 24 MW PG-2 steam generator which was mounted in a BOR-60 reactor and which is a model of the steam generator of a BN-600 unit. The experiment and its main results have been described in [4]. The experimental data, for which a processing algorithm is described in the present paper, were obtained from an acoustic waveguide-type sensor mounted in the upper part of the overheater. The distance from the sensor to the point of argon injection into sodium was 1.2 m; the argon consumption was 0.3 g/sec. The sensor was mounted so that the developing gas bubbles did not shield it.

The magnetic tape recordings of the signals obtained from the acoustic sensor were pro- cessed with a special unit [5, 6] which allows the operational calculation of energy spectra. Sixty samples were evaluated for the background and for the sum of effect + background with 20,000 values of the initial process in each of the samples. The samples formed an instruct- ing sequence. The spectra were analyzed in an 80 kHz frequency band. Further, the spectra were processed on a computer with especially developed programs.

REQUIREMENTS TO THE PROCESSING ALGORITHMS

The selection of the processing algorithms is associated with the requirements of flow detection. The main requirements are as follows:

— high stability against noise, i.e., a low probability of spurious response (spurious alarm);
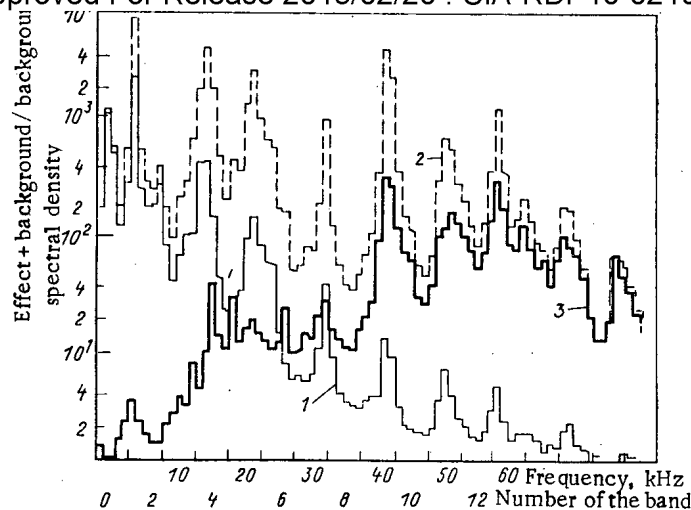
Fig. 1. Energy spectra and ratio effect + background to background: 1) background noise; 2) effect + background; 3) ratio of effect + background to background.

— technical simplicity and a sufficiently high probability of flow detection (low probability of missing a current); and

— the time of detecting a current of 0.3 g/sec must not exceed a few seconds.

We derived on the basis of these conditions the technical conditions under which the number of frequency bands to be analyzed in the instrument to be built was reduced to two; it was assumed that the width of the filter resonance curves is 5 kHz. The probability of a spurious alarm was preset as 10^{-6} and that of omitting a current as 10^{-3}. The possible spread of the resonance frequency of the sensors was ±5 kHz.

Algorithms for evaluating the data in the instrument must be as simple as possible for reducing the required memory space and for increasing the response rate. Therefore, one must study first of all the applicability of the algorithms of linear and piecewise linear classifiers. The problem therefore implies the recognition of objects of a given number of classes (background and sum of effect + background), i.e., separating lines must be drawn on the plane of the parameters selected (the two frequency bands providing most of the information).

The algorithms of recognition must provide, as far as possible, an objective classification. One must employ also that a priori information which is at the disposition of the researcher, namely the form of the frequency spectra of effect + background, information on the physical processes which are associated with the generation and development of a current, etc.

Figure 1 illustrates the form of the spectra of effect + background and of background noise (spectra resulting from averaging over 15 samples); Figure 1 also illustrates the ratio in dependence upon the frequency. Peaks which are typical for a resonance sensor appear in the spectra. One also observes a tendency to an increase in the ratio with increasing frequency. The background noise of the steam generator develops from the interaction of turbulent flow of liquid (sodium, water) and steam with the elements of the unit. This noise has a broad frequency spectrum with a maximum which is usually situated at a few kilohertz. In the simulation of the current, the outflow velocity of the gas stream is much greater (hundreds of m/sec) than the flow velocity of the liquid and the steam in the steam generator. Therefore, a relative increase in the spectral density must be observed at high frequencies in the spectrum of the background + effect signal.

When two frequency bands are selected, one must recall that owing to their shifting in the case of deviations of the resonance frequencies of the sensors (because the sensors are not identical or are unstable) and in changes in the signal spectra generated by the current, the positions of the classes will be shifted in parameter space. It is therefore necessary to study the influence of the shift upon the quality of the classification (recognition); the quality was in the present work assessed through the ratio of the minimum distance between the limits of the separating lines along the straight line connecting the centers of gravity

813
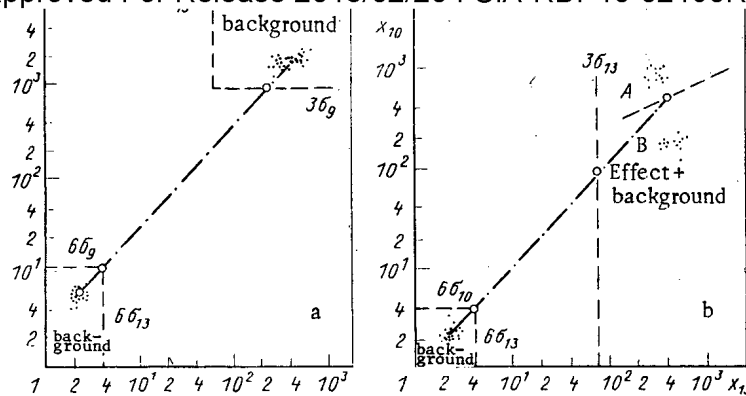
Fig. 2. Distribution of the objects (a) for a divison without shifting; b) for a division with shifiting; X_{13}) average energy in frequency band 13; X_9) average energy in frequency band 9; and X_{10}) average energy in frequency band 10.

of the classes to the standard deviation of the two-dimensional distributions for the objects of the background.

The form of the spectra and their ratio point to at least two strongly different states (classes) in the system. Frequency bands which provide information must be looked for in the high-frequency range.

ALGORITHMS OF THE INSTRUCTING MODE

Taking into account the given width of the frequency characteristics of the filters, the spectra were split into 16 neighboring bands of equal width (5 kHz); in each of these bands the data were integrated and averaged over the number of components summed. The second version of splitting served to verify the influence of the shift upon the quality of the classification. The splitting was performed with a 1-kHz shift to the right for part of the spectra of the effect + background signals. The data obtained were again centered and normalized in both cases. These procedures were performed for each frequency band on all available objects (60 spectra). Furthermore, the correlation matrix $||\rho\,(X_i, X_j)||$, was calculated where X_i and X_j denote the normalized and centered values of the i-th and j-th parameters. A submatrix with the numbers from 9 to 16 was separated from the matrix in accordance with *a priori* data on the effect + background/background ratio.

The method of correlation groups of [7] was employed to single out two groups of parameters which were divided by the smallest correlation coefficient. The following groups were obtained for the unshifted frequency separation (the half-dark figures represent the parameters numbers, i.e., the frequency bands):

14	16	15	13	12	11	first group;
9	10					second group.

For the Separation with Shifting of the Spectra:

12	16	15	11	9	14	first group;
10						second group.

The parameter groups determined can be treated further for calculations factors and for constructing classifiers in the newly obtained factor space [7]. But this approach would complicate the calculation procedure. Therefore, the correlation matrix was used to construct a simple criterion for the determination of a pair of bands with the greatest information content; after that, a piecewise-linear classification was made. The selection criteria for the parameter pair with the greatest information content was based upon the following concepts:

— the higher the (effect + background)/background ratio the greater the probability of obtaining a classification of good quality;

— the probability of a spurious alarm and of missing a current increases with increasing dispersion of the background, i.e., the quality of the classification becomes worse;

814

— the quality of the classification will increase with increasing ratio of the average value of the background; and

— the weaker the relation between the parameters (the smaller the correlation coefficient), the more objective properties of the system will be reflected.

Thus, the following criterion can be suggested:

$$K(X_i, X_j) = [1 - \rho(X_i, X_j)] \frac{S_i S_j (\overline{X}_{e.b_i})^2 (\overline{X}_{e.b_j})^2}{\sigma_{e.b_i} \sigma_{b_i} \sigma_{e.b_j} \sigma_{b_j}},$$

where

$$S_i = \overline{X}_{e.b_i}/\overline{X}_{b_i}; \quad S_j = \overline{X}_{e.b_j}/\overline{X}_{b_j}; \quad \overline{X}_{e.b_i} = \frac{1}{n} \sum_{k=1}^{n} X_{ik}$$

denotes the average value of the i-th parameter over n objects of the sum of effect and background; $\overline{X}_{b_i}$ denotes the average value of the i-th parameter for n objects of the background; and $\sigma_{e.b_i}$ and σ_{b_i} denotes the corresponding standard deviations of the i-th parameter. A similar notation was introduced for the j-th parameter. The maximum of the $K(X_i, X_j)$ value must correspond to the selection of the parameter pair (i, j) providing a maximum of information.

RESULTS OF THE CALCULATIONS

Calculations made with the criterion selected rendered the following results: in the case of an unshifted division according to frequency bands: i = 13 and j = 9; in the case of a shifted division: i = 13 and j = 10. The numbers i and j obtained for the parameters are in both cases in different groups which were determined by the method of correlation groups. This detail partly confirms that the parameter selection is correct.

Figure 2 illustrates the possible classification of objects for various forms of division. It follows from the figure that as a results of the shifting, the effect + background class is divided into two subclasses A and B and the quality index of the classification is reduced, mainly because of the sharp increase in the dispersion of the parameter X_{10}. At the same time, a change in the position of the objects of the effect + background class on the parameter plane can be caused by changes in the operational conditions of the steam generator, the characteristics of the current or the parameters of the instrument. Information on these changes can be used for improving the diagnostic capacity of the instrument. But it should be recalled that all this is associated with complications and an enhancement of the time analysis. The dashed line of Fig. 2 indicates the position of the dividing straight lines) the position was determined from the preset probabilities of a spurious alarm and of missing a current. Such lines can be easily produced on a display screen without significant time losses when simple programming is used.

The results of the processing of the recordings of the experiments have shown that a classification of objects in the form of effect + background and background is possible in accordance with the suggested criterion.

LITERATURE CITED

1. I. A. Birger, Technical Diagnostics [in Russian], Mashinostroenie, Moscow (1978).
2. A. L. Gorelik and V. A. Skripnik, Recognition Methods [in Russian], Vysshaya Shkola Moscow (1977).
3. V. N. Vapnik and A. Ya. Chervonenkis, The Theory of Sample Recognition [in Russian], Nauka, Moscow (1974).
4. V. M. Sokolov, Yu. P. Grebenkin, V. V. Golushko, and A. B. Muralev, Experimental Foundation of the Possible Detection of Currents in a Steam Generator through Acoustic Noise [in Russian], Preprint NIIAR-35 (550), Dimitrovgrad (1982).
5. V. V. Golushko and A. B. Muralev, A System for the Digital Processing of Random Processes. Principles of its Construction [in Russian], Preprint NIIAR, P-3 (337), Dimitrovgrad (1978).
6. A. N. Bulanov, V. V. Golushko, and A. B. Muralev, A System for the Digital Processing of Random Processes. Circuit Solutions [in Russian], Preprint NIIAR, P-8 (342), Dimitrovgrad (1978).

DYNAMICS OF HEAT-TRANSFER DEGRADATION IN CHANNELS WITH THE BOTTOM

INLET SEALED

B. F. Balunov, E. L. Smirnov,   UDC 621.039.536
and Yu. N. Ilyukhin

In different operational states of power-generating equipment it is possible that in
a vertical heat-liberating channel water can stop flowing into the bottom of the channel.
At the same time, the water level can be located above the top of the channel. After some
finite time interval, required for heating all water present in the channel up to the satura-
tion temperature, the channel can be regarded as a steam-generating channel with the bottom
inlet sealed off. In such channels heat transfer is degraded when the balance between the
flow rates of the countermoving flows (rising steam flow G_2 and descending water flow G_1) is
destroyed [1]. This breakdown of the equality $G_1 = G_2$ (toward increasing G_2 and decreasing
G_1) can be viewed as a particular case of the hydrodynamic critical state of countermoving
gas—liquid flows (known in the literature as the phenomenon of "flooding" [2, 3]), determining
the maximum possible flow rate G_1 for a fixed flow rate G_2.

The hydrodynamical critical state appears in the section with maximum steam flow velo-
city $w_2 = G_2/\rho_2 F_{ft}$, i.e., in the top section of the channel. When fluid enters the channel
from above ($G_1 > 0$) the sections with the hydrodynamic critical state and the state of de-
gradiation of heat transfer may not coincide and the time between these characteristic states
can be equal to tens of minutes.

We shall study a vertical cylindrical steam-generating channel with a constant flow-
through cross section (F_{ft}) and a sealed inlet at the bottom (Fig. 1). At the moment that
the hydrodynamic critical state appears ($\tau = 0$), a steam–water mixture is present in the
channel. The distribution of the true volume steam content over the height of the channel
is found from the well-known working dependences for bubbling:

$$\varphi_0 = f\,(p,\ w_2),\tag{1}$$

where

$$w_2 = \frac{1}{r\rho_2 F_{\text{ft}}} \int\limits_{L}^{z} \left(\frac{dN}{dz}\right) dz.\tag{2}$$

The maximum value of w_2 occurs in the heated section of the channel at the top ($z = 0$); it is
this section that must be regarded as being critical in the hydrodynamic sense.

For countermoving steam–water flows with steam–water flows with steam velocities ex-
ceeding the values corresponding to the condition of "free-fall" of water drops [4]

$$K_2 = \frac{w_2 \sqrt{\rho_2}}{\sqrt[4]{\sigma g\,(\rho_1 - \rho_2)}} = 0.7 - 1.4,$$

only an annular flow state (descending water films at the wall and ascending steam core) is
possible. Experiments have shown that the particular case of the hydrodynamic critical
state ($G_2 > G_1$) in the top section of the channel studied here is characterized by the values
$K_2 = 0.8-2.2$. Therefore, an annular flow state exists in this section. The film motion of
practically all water entering at the top along the channel walls also extends into the
lower part of the channel. At the same time the heat-liberating surface of the channel is
cooled in the normal manner by the evaporation of the descending film of fluid up to the
formation of stable discontinuities in it, whose appearance is characterized by a definite
trickling density:
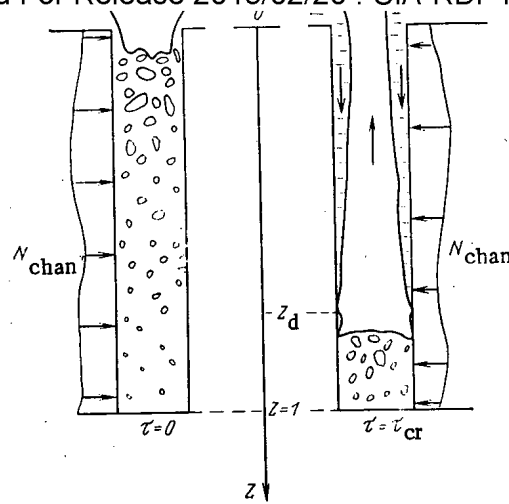
Fig. 1.   Diagram of a vertical steam-generating channel
with a sealed inlet at the bottom.

$$\Gamma = \frac{Gd}{\Pi} = \frac{Gd}{\pi d}.$$

The distance between the hydrodynamically critical section and the section with degraded heat transfer (z_d) can be found from the condition

$$G_1 = Gd + \frac{1}{r} \int_0^{z_d} \left(\frac{dN}{dz} \right) dz. \tag{3}$$

For a channel which is heated uniformly over its height (dN/dz) = N/L and the formula (3) assumes the form

$$G_1 = G_d + \frac{N}{r} \frac{z_d}{L} \tag{4}$$

(if $G_d \gg G_1$, then the degradation of heat transfer occurs in the heated section at the top of the channel). The mass of water between the sections z = 0 and z = z_d in the film of descending liquid

$$m_{film} = \Pi \rho_1 \int_0^{z_d} \delta_{film} dz = F_{ft} \rho_1 \int_0^{z_d} (1 - \varphi_{film}) \, dz$$

is much lower than the mass of water in the same section of the channel at the moment that the hydrodynamic critical state appears ($\tau = 0$):

$$m_0 = F_{ft} \rho_1 \int_0^{z_d} (1 - \varphi_0) \, dz.$$

Thus, under the conditions of unbalance between the flow rate of the generated steam and the water entering the channel at the top ($G_2 > G_1 > G_d$), a definite degradation time τ_{deg} is required for evaporation of the water located in the channel between the sections z = 0 and z = z_d outside the film on the wall:

$$\Delta m_w = F_{ft} \; \rho_1 \int_0^{z_d} [(1 - \varphi_0) - (1 - \varphi_{film})] \, dz = F_{ft} \; \rho_1 z_d [(1 - \bar{\varphi}_0) - (1 - \bar{\varphi}_{film})]. \tag{5}$$

The value of τ_{deg} can be determined from the equation of mass balance

$$\Delta m_w = (G_2 - G_1) \, \tau_{deg}. \tag{6}$$

In Eq. (6)

$$G_2 = N/r, \tag{7}$$

and G_d in Eqs. (3) and (4) is obtained from the recommendations of [5]. The results of the

817
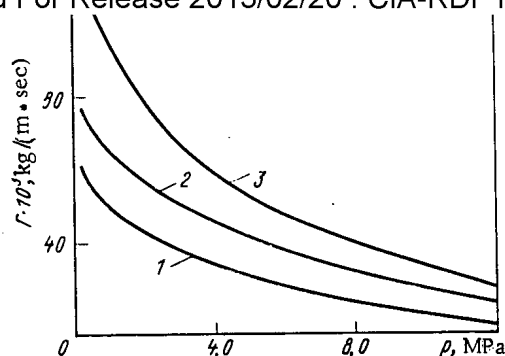
Fig. 2. Minimum (without breaks in the film) trickling density on the surface of a vertical channel for a descending film of water: 1) unheated surface; 2) heated surface, q = (12–180) kW/m²; 3) same, q = 250 kW/m².

calculations of $\Gamma = G_p/\pi d$, confirmed by experiments in the range p = 0.2–12 MPa, q = 12–250 kW/m², d = 30–53 mm, are presented in Fig. 2.

The value of G_1 is determined from the relation between the flow rate of the water and steam in the presence of "flooding" in vertical heated tubes in terms of the criteria of [6]:

$$\sqrt{K_2} + a\sqrt{K_1} = b \text{ th} \, (c \, \text{Bo}^{0,25}),$$

where

$$K_1 = \frac{G_1}{F_{ft} \sqrt[4]{\rho_1^2 \sigma g \, (\rho_1 - \rho_2)}}, \quad \text{Bo} = d\sqrt{\frac{g\,(\rho_1 - \rho_2)}{\sigma}}.$$

In the range of state parameters studied p = 0.2–6 MPa; d = (30–53) 10^{-3} m; q = 50–250 kW/m², this relation can be approximated by the dependence

$$\sqrt{K_2} + 0.94\sqrt{K_1} = 1.07 \, \text{Bo}^{0.125}. \tag{8}$$

It is recommended in [7] that the well-known formulas of Nusselt and Find be used to calculate the thickness of the liquid film in the presence of flooding. These formulas do not take into account the effect of the counterflowing gas (steam) flow and are therefore universal for the entire region $0 \leqslant z \leqslant z_d$. Based on the values of $G_1/\pi d$ obtained in the experiments, calculations using these formulas (with $d \geqslant 20$ mm) gave the values $1 - \varphi_{film} \leqslant 0.03$. Therefore the term $(1 - \varphi_{film})$ in Eq. (5) can be neglected compared with the term $(1 - \varphi_0)$, which is not less than 0.3.

Thus Eqs. (5) and (6) can be put into the form

$$\tau_{deg} = \frac{F_{ft}\,\rho_1 \int_0^{z \cdot d} (1 - \varphi_0)\,dz}{G_2 - G_1}. \tag{9}$$

To check the correctness of using in the proposed method the indicated dependences, we performed experiments in tubes with d = (30–53)·10^{-3} m, uniformly heated electrically over the entire length, with the bottom inlet sealed. A vessel with an inner diameter of 79·10^{-3} m, filled with boiling water, was placed above the working section. Its level was more than 3 m higher than the top face of the electrically heated tube. In order to record the degradation of heat transfer, 13 thermocouples, arranged uniformly along the height of the tube, were fastened to the outer surface of the tube. We carried out the experiments under pressures of 0.2–6.0 mPa with a virtually instantaneous ($\tau < 0.5$ sec) increase in the electrical power up to values corresponding to $G_2 > G_1$.*

Using the dependences presented above (1)–(9) as well as the experimental results, we compared the numerical values

---

*The power N > N_{cr}, where N_{cr} is defined according to the recommendations of [8], corresponds conditionally to this value.

818
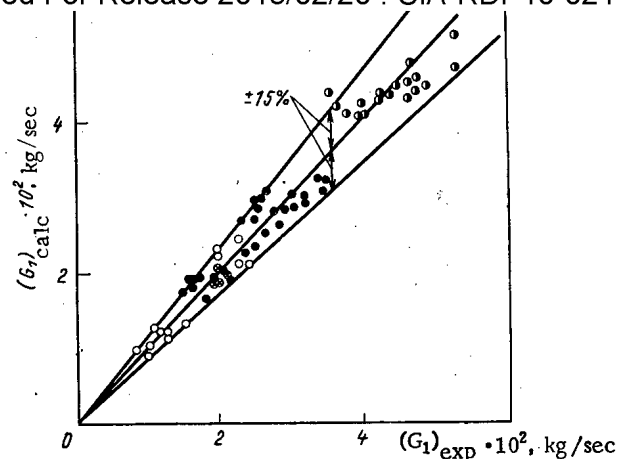
Fig. 3. Comparison of the experimental and computed values of G_1. Electrically heated tube with an inner diameter [mm] of $\bigcirc$ 30; $\otimes$ 40; $\bullet$ 47; $\copyright$ 53; G_{1calc} was obtained from Eq. (8).
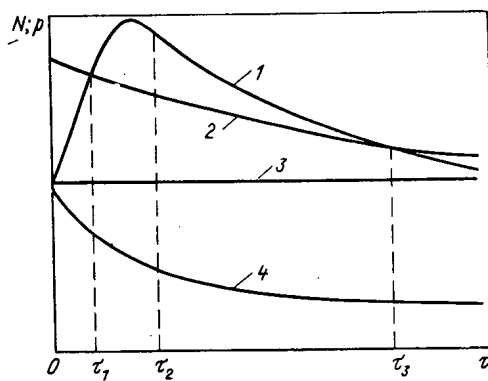
Fig. 4. Change in the parameters accompanying a drop in the pressure in the steam-generating channel: 1) effective power; 2) critical power; 3) capacity of the steam-generating channel; 4) pressure in the channel.

$$(G_1)_{exp} = G_2 - \frac{\rho_1 \; ft \int_0^{z_d} (1 - \varphi_0) \, dz}{(\tau_{deg})_{exp}}, \qquad (10)$$

calculated using the formulas (1) and (7) based on the quantities p, N, and τ_{deg} measured in the experiments and the values of G_1 determined from the dependence (8) for the same values of p and N. The results of this comparison are presented in Fig. 3.

In determining $(\tau_{deg})_{exp}$, the time required for heating the tube wall up to the temperature characteristic for heat outflow accompanying bubble boiling (τ_w) and for establishing a stationary distribution of the steam content over the height of the channel (τ_{φ_0}) was taken into account. In other words, the time required for steam bubbles forming at the bottom of the channel to flow to the top was taken into account:

$$\tau_{\varphi_0} = \frac{\int_0^L (1 - \varphi) \, dz}{\Delta w}.$$

The time $\tau_w + \tau_{\varphi_0}$ is required to achieve the conditions for the onset of the hydrodynamic critical state in the countermoving steam-water flows in the top section. The value of $\tau_w + \tau_{\varphi_0}$ did not exceed 2-3 sec in the experiments.

$(G_2 > G_1 > 0.5\ G_2)$, which gave a maximum error in $(G_1)_{exp}$ of $\pm 15\%$.

In this analysis the coordinates $(z_d)_{exp}$ and $(\tau_{yx})_{exp}$ could be data from any thermocouple recording the degradation of heat transfer. The results of the comparison (see Fig. 3) indicate the correctness of the calculations performed.

It is therefore recommended that Eq. (9) be used to determine the time interval from the moment the hydrodynamic critical state appears in the countermoving steam-water flows up to the onset of the growth of the temperature of the heat-liberating surface. In order to obtain the values of the quantities appearing in this formula, the expressions (1)-(3), (7), and (8) are required.

We recall that if in the calculation using Eqs. (4) and (9) $G_d > G_1$, then it is necessary to set $\tau_{yx} = 0$; this corresponds to the onset of the hydrodynamic critical state and degradation of heat transfer in the heated top section of the channel.

In the computational procedure described above, it was assumed that the pressure and power (of the thermal load) remained constant throughout the entire process. During real accidents, however, these parameters changes as a function of time, which complicates the solution of the problem. Thus a drop in the pressure in the channel with the boiling water causes additional generation of steam as a result of the heat (accumulated in the water) present in the channel and in the metal structures over which the water flows. The additional heat flux (N_{add}) forms when the pressure (saturation temperature) in the channel changes. In this case, Eq. (7) assumes the form

$$G_2 = (N_{chan} + N_{add})/r = N_{eff}/r. \tag{11}$$

In the case when the duration of the accident $\tau > 3$ sec, when the pressure in the channel drops, the process can be regarded as an equilibrium process and the expression for N_{add} can be written in the form

$$(N_{add})_\tau = \left(-m_1 \frac{di_1}{dp} \frac{dp}{d\tau} + Q_{met} \right)_\tau. \tag{12}$$

Here Q_{met} is the heat flux from the metal structure of the steam-generating channel; over which boiling water flows (it is determined from the formulas of nonstationary heat conduction); m_1 and i_1 are the mass and heat content of the boiling water in the channel, respectively.

We shall describe the procedure for calculating the time interval from the moment that the hydrodynamic critical state appears up to the moment that heat transfer is degraded under nonstationary conditions for the process whose parameters change in the manner shown in Fig. 4. At the time τ_1 a hydrodynamic critical state ($G_2 > G_1$, i.e., $N_{eff} > N_{cr}$) appears in the channel with the bottom inlet sealed. Further growth of N_{eff} and drop in pressure give rise to an increase in the steam content as a function of time in the channel (under the conditions of bubbling) and to continued ejection of the steam-water mixture from it (under the condition that the volume of the channel remains constant). The termination of this process is characterized by the time τ_2 corresponding to the maximum of the dependence

$$\overline{\varphi}L = \int_0^L \varphi\, dz = f(\tau),$$

where $\varphi(z)$ is determined from the formulas for bubbling (1) and (2).

In the interval $\tau_1 < \tau < \tau_2$ water does not flow into the channel at the top and a critical state can (but is unlikely to) appear in heat transfer accompanying the ascending motion of the steam-water mixture.

At the time τ_2 (with $K_2 < 3.2$) the water once again begins to enter the channel at the top, and in order to determine the time interval from τ_2 up to the moment of degradation of heat transfer the procedure used above must be used.

In this case, the system of equations (3) and (5) is written in the form

$$F_{ft}\left[\rho_1 \int_0^L (1-\varphi_0)\, dz \right]_{\tau_1} - \int_{\tau_2}^{\tau_{deg}} (G_2 - G_1)\, d\tau = F_{ft}\left[\rho_1 \int_{z_d}^L (1-\varphi_0)\, dz \right]_{\tau_{deg}}; \tag{13}$$

820

$$(G_1)_\tau = \left[G_d + \frac{1}{r} \int_0^{z_d} \left(\frac{dN}{dz} \right) dz \right]_\tau, \qquad (14)$$

where the values of the quantities entering into these equations are obtained from formulas (1)-(3), (8), (9), (11), and (12).

Terms of the form $F_{ft} \rho_1 \int_{z_i}^L (1 - \varphi) dz$ (with $z_i = 0$ and $z_i = z_d$) in the case of the assumptions made represent the mass of the water $(m_0)_\tau$ and $(m_{deg})_\tau$ present in the channel at the times τ_0 and τ_{deg}, and can be used to calculate N_{add} from Eq. (12).

The determination of the value of τ_{deg} is regarded as final when one of the following conditions is satisfied: the left side of Eq. (13) becomes less than the right side or the value of $(G_1)_\tau$ becomes less than that of $(G_p)_\tau$.

When $\tau > \tau_3$ the condition $G_2 > G_1$ is violated, and the mass of water in the channel begins to increase and the degradation of heat transfer being studied here becomes impossible.

The calculations based on the foregoing method were compared with the results of experiments performed with decreasing pressure ($dp/pd\tau < 1.2 \cdot 10^{-2}$ sec^{-1}) and N = const. The disagreement between the calculated and measured values of τ_{deg} (with $\tau_2 < 3$ sec) does not exceed ±20%, which, under the assumptions made, must be regarded as satisfactory.

LITERATURE CITED

1. B. F. Balunov and E. L. Smirnov, "Critical thermal flows in the absence of coolant flow in vertical steam-generating channels," At. Energ., 51, No. 4, 222-224 (1981).
2. G. Wallis, One-Dimensional Two-Phase Flow, McGraw-Hill (1969).
3. S. S. Kutateladze and Yu. L. Sorokin, "Hydrodynamic stability of some flow states of gas—liquid systems," in: Problems in the Heat Transfer and the Hydraulics of Two-Phase Systems [in Russian], Gosénergoizdat, Moscow (1961), pp. 315-324.
4. D. A. Frank-Kamenetskii, Diffusion and Heat Transfer in Chemical Kinetics, Plenum Press (1966).
5. N. Zuber and F. Staub, "Stability of dry patches forming in liquid film flowing over heated surfaces," Int. J. Heat Mass Transfer, 9, No. 9, 897-905 (1966).
6. K. Chung, C. Liu, and C. Tien, "Flooding in two-pase countercurrent flows. 2. Experimental Investigation," Phys. Chem. Hydrodynamics, 1, No. 2-3, 208-220 (1980).
7. H. Imura, H. Kusuda, and S. Funatsu, "Flooding velocity in a counter current two-phase flow," Chem. Eng. Sci., 32, 79-87 (1977).
8. Yu. N. Ilyukhin, E. L. Smirnov, and B. F. Balunov, Énergomashinostroenie, No. 1, 5-8 (1985).

DIMENSIONAL STABILITY OF STRUCTURAL MATERIALS UNDER LARGE NEUTRON

FLUENCES

N. K. Vasina, I. P. Kursevich,
O. A. Kozhevnikov, V. K. Shamardin,
and V. N. Golovanov   UDC 621.039.531

The dependence of swelling of the steels and alloys having fcc, bcc, and hcp crystal structures on the temperature and the dose plays an important role in the choice of materials for nuclear and thermonuclear reactors. As applied to the field of large neutron fluences, for a number of structural materials such data are obtained by carrying out simulation experiments using charged particle accelerators [1-3]. In view of the well-known shortcomings of such experiments and their uncoordinated nature, we carried out direct determination of the radiation-induced swelling of a number of austenitic, ferritic, refractory, and titanium-based materials in the 400-650°C range at a neutron fluence of $\sim 1 \cdot 10^{23}$ cm^{-2} (E > 0.1 MeV). A comparative study of the obtained data and the results of the simulation experiments conducted previously on these materials is expected to help in establishing a possible correlation between the values of swelling found in both modes of inducing radiational damages.

Table 1 shows the chemical composition and the regime of prior treatment of the experimental materials.

The test specimens were in the form of cylindrical rods (wires) measuring 3 mm in diameter and 27 mm in length with plane parallel polished end faces. The specimens were irradiated in the core of a BOR-60 reactor using a special assembly for material studies. The neutron fluence was maintained at $(7.4-11.7) \cdot 10^{22}$ cm^{-2} (E > 0.1 MeV) corresponding to 42-65 displacements per atom according to the TRN-standard. Along the height of the assembly, the temperature was varied from 400 up to 650°C by creating a predetermined gap between the external case and the internal ampul containing the specimen cassettes.
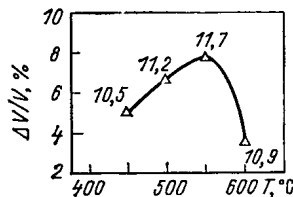
Fig. 1   Fig. 2

Fig. 1. Temperature dependence of swelling of Kh15N35M2 steel (in all the figures the numbers adjacent to the points indicate neutron fluence $\times 10^{22}$ cm^{-2}; E > 0.1 MeV).
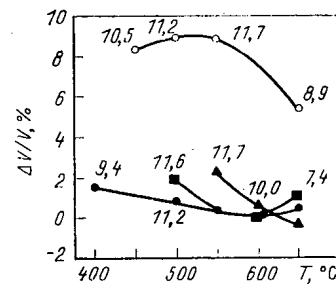
Fig. 2. Temperature dependence of swelling of the alloys of the base composition Fe-20% Cr-45 Ni and pure nickel: ○) nickel (99.99%); ●) Kh20N45M4BRTs (austenitizing at 1200°C, water quenching + austenitizing at 1050°C for a period of 1 h, water quenching), grain size number 3-4; ■) Kh20N45M4BRTs (austenitizing at 1050°C for a period of 1 h, water quenching), grain size number 6-8; ▲) Kh20N45B (austenitizing at 1050°C for 1 h, water quenching).

0038-531X/85/5904-0822$09.50

TABLE 1. Chemical Composition and the Regimes of Prior Treatment of the Experimental Materials

Material designation and condition	Weight content of elements, %												
	C	Si	Mn	Cr	Ni	Mo	Ti	Nb	Al	S	P	other elements	Fe
Kh16N11M3:													
austenitizing at 1050°C for 1 h, air cooling	0,06	0,58	1,3	16,25	10,71	2,28	0,1	—	—	0,015	0,015	—	remainder
austenitizing + 15% cold deformation	0,06	0,58	1,3	16,25	10,71	2,28	0,1	—	—	0,015	0,015	—	Same
austenitizing + 50% cold deformation	0,06	0,58	1,3	16,25	10,71	2,28	0,1	—	—	0,015	0,015	—	» »
Kh15N35M2:													
austenitizing at 1050°C for 1 h + air cooling	0,05	0,28	1,18	14,6	37,3	2,7	—	—	—	0,005	0,1	—	» »
Kh20N45B:													
austenitizing at 1050°C for 1 h + air cooling	0,03	0,23	0,36	18,89	44,55	—	0,01	1,25	0,12	0,009	0,006	—	—
Kh20N45M4BRTs:													
austenitizing at 1200°C for 5 h, water quenching + austenitizing at 1050°C for 1 h, water quenching (grain size numbers 3—4)	0,022	0,18	0,51	19,5	44,6	3,92	—	0,79	—	0,004	0,007	0,02 Zr	
Kh20N45M4BRTs:													
austenitizing at 1050°C for 1 h, water quenching (grain size number 6—8)	0,022	0,18	0,51	19,5	44,6	3,92	—	0,79	—	0,004	0,007	0,02 Zr	remainder
Nickel, annealing at 800°C for 1 h, air cooling	—	0,02	0,0002	0,006	99,9	0,001	0,01	—	—	—	—	—	0,02
01Kh13MCh, annealing at 800°C for 1 h, air cooling	0,035	0,45	0,53	14,53	0,05	1,08	—	—	0,04	0,01	0,01	0,005 Y	remainder
Molybdenum alloy, annealing at 1250°C for 1 h, air cooling	—	—	—	—	—	99,5	—	—	—	—	—	—	—
Niobium alloy, annealing at 1250°C for 1 h, air cooling	—	—	—	—	—	—	—	99,8	—	—	—	—	—
Titanium, annealing at 780°C for 1 h, air cooling	0,04	0,02	—	—	—	—	99,2	—	0,53	—	—	0,080 H_2 0,055 H_2 0,02 N_2	

TABLE 2. Swelling of the Steel Kh16N11M3 Under Different Structural Conditions

Condition	Irradiation parameters		Length change $\Delta l/l$, %	Volume change $\Delta V/V$, %
	neutron fluence $\times 10^{22}$ cm^{-2} (E > 0.1 MeV)	temp., °C		
Austenitizing	11,2	500	2,0	6,0
»	11,7	550	4,15	12,5
Austenitizing + 15% cold deformation	10,5	450	1,2	3,6
Same	11,7	550	3,0	9,0
» »	8,9	650	2,0	6,0
Austenitizing + 50% cold deformation	10,5	450	0,85	2,6
Same	11,7	550	2,4	7,2

823

Fig. 3. Temperature dependence of swelling of the bcc and hcp materials: ○) titanium (commercial purity); ●) 01Kh13MCh steel; ■) Mo alloy; ▲) Nb alloy.
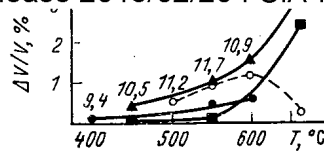
The magnitude of swelling was determined by precisely measuring the length of the specimens before and after irradiation within an error of ±0.01% using a special remote device designed incorporating an IZV-3 length measuring machine.

Table 2 gives the results of studies on the steel Kh16N11M3 under various structural conditions. The maximum swelling (~12.5%) was observed for the steel in the austenitized conditon at an irradiation temperature of 550°C. Cold working the steel by 15% and, in particular, by 50% effectively decreases swelling.

The temperature dependence of swelling of the Kh15N35M2 steel (Fig. 1) is characterized by a clearly defined maximum at 550°C amounting to 8% which is close to the swelling of the Kh16N11M3 steel in cold worked condition. Such a high swelling of the Kh15N35M2 steel does not agree with the conclusion of Johnson et al. [4] based on simulation experiments that the steels containing 35% Ni have a low swelling tendency.

Figure 2 shows the data on the swelling of pure nickel and the solid-solution strengh-ened high-nickel alloys Kh20N45B and Kh20N45M4BRTs in the austenitized condition; here, the alloy Kh20N45M4BRTs was austenitized at 1050 and 1200°C in order to obtain grain sizes corresponding to the numbers 6-8 and 3-4, respectively. The swelling curve of pure nickel has nonmonotonic nature and exhibits a maximum at 550°C. Taking the temperature shift into account, it agrees well with the previously published data [5] on the effect of ion bombardment.

Swelling of high-nickel alloys of the composition Fe—20 Cr—45 Ni does not exceed ~2% independent of alloying and the heat treatment regime. This agrees well with the data of the simulation experiments [1]. Furthermore, it is seen that the maximum resistance to swelling is exhibited by the alloy Kh20N45M4BRTs after austenitizing at 1200°C whereby the maximum amount of alloying elements is taken into the solid solution.

Based on an analysis of the obtained results, we can conclude that a satisfactory resistance to swelling of the solid-solution strengthened austenitic alloys can be achieved at a sufficiently high content of nickel (~45%) and the other alloying elements (Al, Ti, Nb, etc.) having a size incompatibility with the elements of the matrix.

The reduced radiation swelling of the Fe—Cr—Ni alloys at high nickel contents is attributed to short-range ordering of the solid solution [6]. The absence of a correlation between the swelling of the steels of the composition Fe—15 Cr—35 Ni under neutron and ion irradiation is apparently because of the difference in the duration of irradiation and in view of the fact that in both cases radiation-induced segregation of various elements (including nickel) occurs [7]. During prolonged neutron irradiation considerable depletion of nickel from the austenite matrix takes place because of its migration to sinks and, therefore, the nickel content in the solid solution becomes insufficient for reducing the magnitude of swelling, for example, by the mechanism of short-range ordering. During ion irradiation, where bombardment with charged particles lasts only for a few hours, the process of depletion of nickel from the solid solution does not occur to a significant extent.

The data on the swelling of the ferritic stainless steel 01Kh13MCh (Fig. 3) confirms the well-known high resistance of this class of steels to swelling. Similar results were obtained in the simulation experiments also [2].

Swelling of the molybdenum and niobium alloys (see Fig. 3) increases with increasing irradiation temperature, but does not exceed 3% at 650°C. These results as well as the data of Norris [8] show that the maximum swelling of the refractory metals having bcc lattice occurs in the region of higher temperatures than in the case of the fcc metals. A study of commercial purity titanium (hcp lattice) showed (see Fig. 3) that irradiation right up to a

824

hig...
eration range 500–650°C ($\Delta V/V \leq 1.2\%$). This agrees with the data of the simulation experiments [3].

LITERATURE CITED

1. V. F. Zelenskii et al., Vopr. At. Nauk. Tekh. Ser. Fiz. Rad. Povrezh. Rad. Materialoved., Issue 2 (13), 18-22 (1980).
2. A. M. Parshin et al., ibid., Issue 2 (13), 13-17 (1980).
3. V. F. Zelenskii et al., ibid., Issue 2 (16), 57-61 (1981).
4. W. Johnson et al., "An experimental survey of swelling in commercial Fe—Cr—Ni alloys bombarded with 5 MeV Ni-ions," J. Nucl. Mater., 54, No. 1, 24-40 (1974).
5. V. I. Bendikov et al., Vopr. At. Nauk. Tekh. Ser. Fiz. Rad. Povrezh. Rad. Materialoved., Issue 4 (23), 9-11 (1982).
6. I. P. Kursevich, V. A. Nikolaev, et al., ibid., Issue 4 (32), 57-64 (1984).
7. P. Okamoto, J. Nucl. Mater., 53, 336 (1974).
8. D. Norris, Rad. Effects, 15, 1 (1972).

EFFECT OF THERMOMECHANICAL TREATMENT ON THE SWELLING OF STEEL OKh16N15M3B

V. I. Shcherbak, V. N. Bykov,   UDC 621.039:553.3:669.15
and V. D. Dmitriev

Our earlier studies [1, 2] showed that thermomechanical treatment can significantly affect the mechanical properties and swelling of steels irradiated with fast neutrons. In view of this, it is interesting to carry out a more detailed study of the effect of such a treatment on the microstructure of the fuel element jackets of a BOR-60 reactor made from the austenitized steel OKh16N15M3B (holding at 1100°C for a period of 20 min) and the jackets made from the same steel, but subjected to thermomechanical treatment (15% cold deformation and annealing for 1 h at 800°C). For the present investigation we selected two centrally located adjacent fuel elements of a BN-6 experimental packet that was irradiated up to a neutron fluence of $6.6 \cdot 10^{22}$ cm^{-2} ($E_n > 0.1$ MeV) in the temperature range 340–640°C. Electron-microscopic studies were carried out on 12 different sections along the height of the jacket. The length of the fuel column in the fuel elements amounted to 500 mm.

The microstructure of the reference specimens showed that the austenitized steel OKh16N15M3B had a dislocation density of $5 \cdot 10^9$ cm^{-2}. The thermomechanical treatment of this steel led to the deposition of finely dispersed niobium carbonitride particles decorating the dislocations and the precipitates of the Laves phase; in this case, the dislocation density within the grains varied from $6 \cdot 10^{10}$ up to $2 \cdot 10^{11}$ cm^{-2}. An analysis of the electron micrographs of the steel showed that the precipitate particles deposit only on the edge dislocations or 'tripod' faults originating from the dissociation (splitting) of dislocation lines retained in the structure of the steel after cold working and annealing. The twin and grain boundaries were also decorated significantly with niobium carbide particles; here, the grain boundaries had precipitate-free zones measuring 700 Å in width.

When studying the specimens cut out from different sections of the fuel elements jackets made from the austenitic steel, we obtained the characteristic microstructure of the neutron irradiated OK16N15M3B steel (Fig. 1a, b, c). Dislocation loops and precipitate particles were observed in the lower sections. The size of the dislocation loops increases with increasing irradiation temperature. In this case, at the maximum fluence the dislocation density reached $7 \cdot 10^{10}$ cm^{-2}, and in the segments irradiated at 600°C, it was equal to 10^{10} cm^{-2}. Furthermore, Fig. 1 shows that the precipitate particles size increases with increasing irradiation temperature. Particularly intense growth of the precipitate particles of the other phases takes place at a temperature exceeding 550°C.

It was found that niobium carbonitride particles and the Laves phase are the main precipitates in the irradiated steel OKh16N15M3B. In the segments subjected to high tempera-
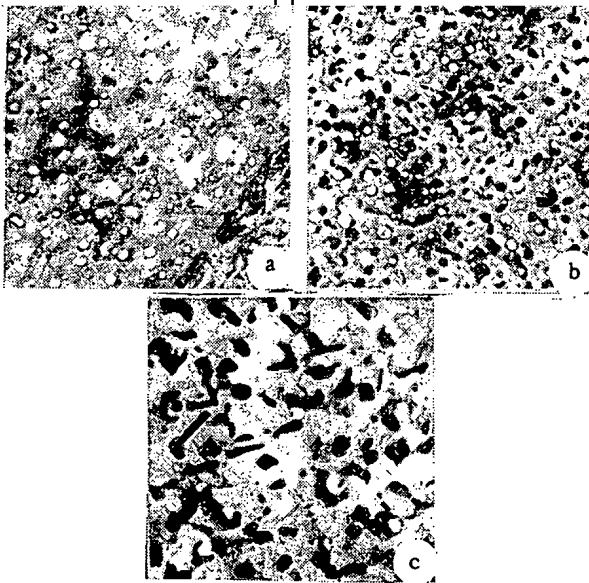
Fig. 1. Microstructure of the steel OKh16N15M3B after irradiating up to a neutron fluence (E_n > 0.1 MeV) of $5.0 \cdot 10^{22}$ cm^{-2} at 430°C (a), $6.3 \cdot 10^{22}$ cm^{-2}, 460°C (b), and $4.3 \cdot 10^{22}$ cm^{-2}, 610°C (c). Mag. × 50,000.
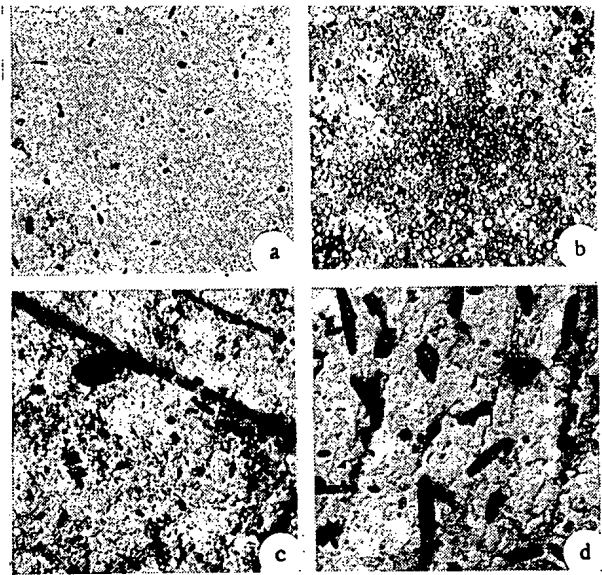
Fig. 2. Microstructure of the steel OKh16N15M3B after thermomechanical treatment and irradiation up to a neutron fluence of $0.5 \cdot 10^{22}$ cm^{-2} at 350°C (a), $5.8 \cdot 10^{22}$ cm^{-2}, 430°C (b), $6.3 \cdot 10^{22}$ cm^{-2}, 460°C (c), and $4.9 \cdot 10^{22}$ cm^{-2}, 610°C (d). Mag. × 50,000.

Fig. 3. Concentration N_v, average diameter <d_v>, and relative volume $\Delta V/V$ of pores in the steel OKh16N15M3B subjected to austenitizing (○) or thermomechanical treatment (●); the dashed line shows the fluence variation along the length of the fuel element.

826

ture, the $M_{23}C_6$ precipitate particles are observed on the grain boundaries as well as within the grains.

After thermomechanical treatment, the steel OKh16N15M3B shows a more nonuniform structure (Fig. 2a, b, c). Irradiation of this steel led to a decrease in the dislocation density up to 10^{11} cm^{-2} and up to $5 \cdot 10^{10}$ cm^{-2} (in the upper sections); in this case, the concentration of the precipitates decreased from $2 \cdot 10^{16}$ cm^{-3} up to 10^{16} cm^{-3}. The finely dispersed niobium carbide precipitates decorating the dislocations are mostly retained even at high irradiation temperatures. At a temperature exceeding 550°C, besides the finely dispersed precipitates, the microstructure of this steel shows coarser particles of other phases (Fig. 2d).

We note that the high dislocation density observed in the steel subjected to such a treatment restrains the coalescence process of the finely dispersed niobium carbonitride particles during irradiation up to a neutron fluence of $6.6 \cdot 10^{22}$ cm^{-2}.

Figure 3a shows the values of the average diameter and the concentration of pores along the height of the steel jacket under different structural conditions. A comparison of the results shows that after irradiating at a temperature below 500°C, the steel existing in the thermomechanically treated condition has higher concentration of pores of smaller size as compared to the austenitized steel. Figure 3b shows that when irradiated at a temperature below 460°C the relative pore volumes are close to each other, and their maximum values amount to 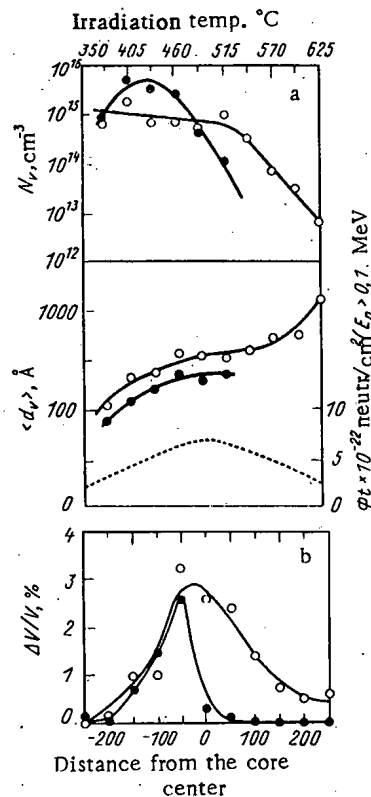3.2 and 2.6% for the steel subjected to austenitizing and to thermomechanical treatment, respectively. When irradiation is carried out at a temperature above 520°C, thermomechanical treatment completely suppresses the process of vacancy related porosity development at the given neutron fluence.

This type of porosity development in the fuel elements made from the steel existing in the thermomechanically treated condition may be explained in the following manner. During irradiation at a temperature below 460°C, blocking of the vast majority of edge dislocations by the depositing precipitate particles occurs. These particles hinder the process of dislocation climb and, thereby, sharply decrease the ability of dislocations to trap the point defects. Owing to this, the dislocation structure formed during such a treatment affects the supersaturation of the matrix with point defects to a considerably less extent. Therefore, in the temperature range under consideration, close values of swelling are observed after thermomechanical treatment and austenitizing. At a temperature above 460°C, where the density of niobium carbonitride precipitates formed during such a treatment begins to decrease, the dislocations can become free from the precipitates more easily, owing to which their effectiveness as sinks for point defects increases. In view of this, when irradiation is carried out at a high temperature up to a neutron fluence of $6.6 \cdot 10^{22}$ cm^{-2}, the effect of thermomechanical treatment is found to be similar to the effect of 10% cold deformation [3].

LITERATURE CITED

1. A. N. Vorobyev, V. N. Bykov, V. D. Dmitriev, and V. I. Shcherbak, "Radiation effects on the mechanical properties and microstructure of solution-treated and cold worked 1Kh18N10T and OKh16N15M3B stainless steels," J. Brit. Nucl. Energy Soc., 14, No. 2, 149-155 (1975).
2. V. N. Bykov, A. M. Dvoryashin, V. D. Dmitriev, and V. I. Shcherbak, "Stability of vacancy pores, dislocation structure, and precipitate particles during annealing of neutron irradiated OKh16N15M3B after austenitizing and thermomechanical treatment," Vopr. At. Nauk. Tekh., Ser. Fiz. Rad. Povrezhd. Rad. Materialoved., Issue 4 (27), 29-32 (1983).
3. N. P. Agapova, V. S. Ageev, M. I. Antipina, et al., "Structural study on the fuel-element jackets made from the steel OKh16N15M3B in cold worked (15%) condition and irradiated in a BOR-60 reactor up to 12.5% depletion," Vopr. At. Nauk. Tekh., Ser. At. Materialoved., Issue 4 (15), 19-26 (1982).

827

HYDROGEN PERMEABILITY IN Kh18N10T STAINLESS STEEL FROM PLASMA
GLOW-DISCHARGE

V. M. Sharapov, A. I. Kanaev,
and A. P. Zakharov   UDC 533.15

In recent years numerous studies have been made on the hydrogen permeability of stain-
less steels and on determining the parameters (constants) of the surface processes under ion
irradiation conditions [1-4]. Such studies are useful not only to understand the role of
different stages of the penetration (permeation) process, but also to predict the possibility
of using austenitic steels in thermonuclear installations. In this paper, we examine the
specific features of hydrogen penetration through the Kh18N10T stainless steel from a glow-
discharge plasma.

EXPERIMENTAL RESULTS

The experimental setup and the procedure for measuring the hydrogen permeability of the
metals in contact with a glow-discharge plasma were described elsewhere [5]. The ion flux
density from the plasma on the specimen amounted to $3 \cdot 10^{16}$ $cm^{-2} \cdot sec^{-1}$ at an ion energy ≤ 350
eV corresponding to the voltage applied across the specimen (cathode) and the anode, and the
temperature range was 520-1000°K.

Figure 1 shows the temperature dependence of hydrogen permeability in the case of two
Kh18N10T stainless steel specimens measuring 0.5 (1) and 1 mm (2) in thickness. In the en-
tire temperature range under study, hydrogen flux P is inversely proportional to the speci-
men thickness. In the high temperature region (670-1000°K) we observe an exponential depen-
dence of the flux on the reciprocal of temperature that is characterized by an activation
energy of 14.5 kcal/mole (60.3 kJ/mole); at lower temperatures (<670°K) this dependence be-
comes significantly weaker.

We conducted experiments in both these temperature regions (below and above 670°K) for
studying the effect of the voltage (potential difference) U between the specimen and the
anode, and the ion flux Q (discharge current j) on the penetrating hydrogen flux. It was
found that the voltage variation (Fig. 2) has no effect on the hydrogen permeability of the
specimen in the entire temperature range. In view of the fact that in these experiments
the voltage was varied (maintaining constant current density) by changing the pressure p by
almost 2 times, we can conclude that under these conditions hydrogen permeability is also
independent of the hydrogen pressure in the discharge gap. It is seen from Fig. 3 that at
all temperatures, the permeating hydrogen flux has a linear dependence on the impinging ion
flux right up to a value of $5 \cdot 10^{16}$ $cm^{-2} \cdot sec^{-1}$.

In these experiments, using the 'lag' (delay) method we measured the diffusion coeffi-
cients of hydrogen at 543 and 563°K in the glow-discharge plasma, and found them to be equal
to $3.5 \cdot 10^{-7}$ and $5.4 \cdot 10^{-7}$ cm^2/sec. These values are in reasonable agreement with the diffu-
sion coefficients measured under ordinary conditions during the interaction with molecular
hydrogen and described by the following equation [6] ($cm^2 \cdot sec$):

$$D = 0.12 \exp(-14100 \text{ cal}/RT).$$

DISCUSSION OF RESULTS

A similar temperature dependence of hydrogen permeability was previously found [7] in
the glow-discharge experiments conducted on nickel. It was assumed that the very weak temp-
erature dependence of hydrogen permeability in the lower temperature region is due to the
effect of the atomic component of plasma. However, in such a case, hydrogen permeability
would have been a function of the hydrogen pressure in the discharge gap; but this contracts
the obtained results (see Fig. 2) in view of the established similarity (agreement) of the
variation of atomic hydrogen content in the glow-discharge plasma with that of hydrogen
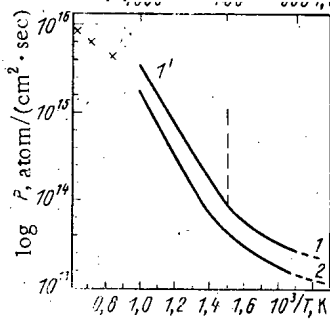
Fig. 1   Fig. 2

Fig. 1. Temperature dependence of hydrogen permeability in
the stainless steel Kh18N10T from plasma glow-discharge:
$P = (\alpha Q / S_1) (D/d)$; $S_t \ll S_p = S_1$; at $T < 700°K$, $S_1 = 18$ exp
$(-10,000 \text{ cal/RT})$; at $T > 700°K$, $S_1 = 7 \cdot 10^{-3}$; $\times$) calculated
values of P at $d = 0.5$ mm.
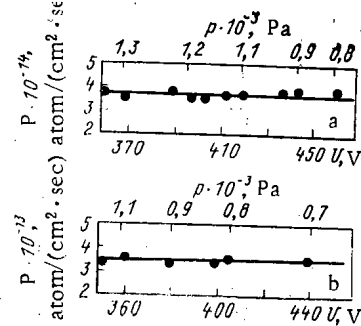
Fig. 2. Dependence of the penetrating hydrogen flux P on
the voltage across the electrodes U and on the hydrogen
pressure p in the discharge gap: a) $T = 790°K$; b) $T = 563°K$.
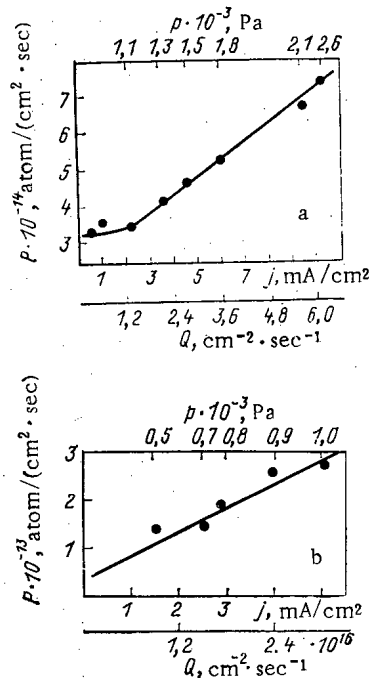
Fig. 3. Dependence of the permeating hydrogen flux P
on the current density of discharge j: a) $T = 800°K$;
b) $T = 563°K$.

pressure in the discharge gap [8]. Thus, under the aforementioned conditions, the hydrogen
permeability of the stainless steel is determined by the ionic component of the plasma.

The specific features of hydrogen permeation through molybdenum and nickel (at low
temperatures) under ion bombardment conditions, in particular, the discontinuities (salient
points) in the temperature dependence of hydrogen permeability, were attributed [7, 9] to
the effect of the 'intrinsic interstial atom' type mobile radiational defects. In this case,
dependence of hydrogen permeability on the voltage across the electrodes and an increase in
the diffusion coefficients of hydrogen were observed. The absence of such effects in the
stainless steel indicate that apparently, the mobile radiational defects do not have a sig-
nificant effect on the hydrogen permeability in this case. Consequently, the aforementioned
discontinuity is related to the effect of ion bombardment on the surface processes.

TABLE 1. Values of the Parameters Characterizing Hydrogen Permeability

T, K	S_1, cm/sec	$1/S_1$, sec/cm	S_t cm/sec	$1/S_t$, sec/cm	D, cm^2/sec	d/D, sec/cm	P, atom/cm$^2 \cdot$ sec)
300	$1 \cdot 10^{-6}$	10^6	$2 \cdot 10^{-7}$	$5 \cdot 10^6$	$5,6 \cdot 10^{-12}$	$9 \cdot 10^9$	—
400	$6,6 \cdot 10^{-5}$	$7,5 \cdot 10^3$	$7,6 \cdot 10^{-6}$	$1,3 \cdot 10^5$	$2 \cdot 10^{-9}$	$2,5 \cdot 10^7$	—
500	$8 \cdot 10^{-4}$	$1,2 \cdot 10^3$	$6,4 \cdot 10^{-5}$	$1,5 \cdot 10^4$	$7,7 \cdot 10^{-8}$	$6,4 \cdot 10^5$	—
600	$4,3 \cdot 10^{-3}$	$2,3 \cdot 10^2$	$2,8 \cdot 10^{-4}$	$3,5 \cdot 10^3$	$8,3 \cdot 10^{-7}$	$6 \cdot 10^4$	$4,8 \cdot 10^{13}$
800	$7 \cdot 10^{-3}$	140	$1,7 \cdot 10^{-3}$	$5,8 \cdot 10^2$	$1,5 \cdot 10^{-5}$	$3,3 \cdot 10^3$	$5,75 \cdot 10^{14}$
900	$7 \cdot 10^{-3}$	140	$3,2 \cdot 10^{-3}$	$3,1 \cdot 10^2$	$4,4 \cdot 10^{-5}$	$1,1 \cdot 10^3$	$1,5 \cdot 10^{15}$
1000	$7 \cdot 10^{-3}$	140	$4,8 \cdot 10^{-3}$	$2 \cdot 10^2$	10^{-4}	$5 \cdot 10^2$	$3,1 \cdot 10^{15}$
1200	—	—	$1 \cdot 10^{-2}$	10^2	$3 \cdot 10^{-4}$	$1,6 \cdot 10^2$	—
1500	—	—	$2,2 \cdot 10^{-2}$	45	10^{-3}	50	—

In this case, diffusional penetration of hydrogen can be described by Eq. (1) with the second-order boundary conditions (2) and (3), and the appropriate initial condition (4) characterizing the absence of hydrogen in the metal at the beginning of the experiment:

$$\frac{\partial C}{\partial t} = D \frac{\partial^2 C}{\partial x^2}; \tag{1}$$

$$-D \frac{\partial C}{\partial x} = \alpha Q - S_1 C |_{x=0}; \tag{2}$$

$$-D \frac{\partial C}{\partial x} = S_2 C |_{x=d}; \tag{3}$$

$$C(x, 0) = 0. \tag{4}$$

The condition (2) reflects the fact that hydrogen introduced into the metal from the ion flux αQ (α is the coefficient of penetration) partially diffuses into the metal (the member $-D \frac{\partial C}{\partial x}$, where D is the diffusion coefficient) and partially liberated reversibly into the discharge chamber (the member $S_1 C$, where S_1 is the reemission rate constant). The liberation of the diffused gas on the reverse side of the membrane is characterized by the constant S_2.

Solving the system of equations (1)-(4) leads to the following expression for the hydrogen flux penetrating through the membrane in the stationary regime steady-state:

$$P = \frac{\alpha Q}{S_1} \frac{1}{1/S_1 + 1/S_2 + d/D}. \tag{5}$$

In the case where penetration is restricted (controlled) by diffusion (the rate of the surface processes is much higher than that of the diffusional discharge $1/S_1$, $1/S_2 \ll d/D$), Eq. (5) simplifies to

$$P = \frac{\alpha Q}{S_1} \frac{D}{d}. \tag{6}$$

Such a direct proportionality between the penetrating hydrogen flux and the incident ion flux (see Fig. 3), and the inverse proportionality with the specimen thickness (see Fig. 1) were observed in the entire temperature range (520–1000°K). Consequently, Eq. (6) can be used for evaluating the hydrogen reemission rate S_1 under ion bombardment conditions. For this purpose, α was taken as 0.4 at an ion energy of 350 eV [10]. Table 1 shows the values of S_1 computed in this manner.

It was established that $S_1 = 7 \cdot 10^{-3}$ cm/sec at T = 670–1000°K, and that it is virtually independent of temperature in this range; however, at T < 670°K, S_1 varies as a function of temperature in the following way (Fig. 4, curve 3) cm/sec:

$$S_1 = 18 \exp(-10000 \, \text{cal} /RT). \tag{7}$$

For calculating S_1 we used the diffusion coefficients D obtained from Eq. (6). The values of D and d/D (for d = 0.5 mm) are given in Table 1. Besides this, the published values [11] of thermal desorption rate S_t (cm/sec) are also shown in Table 1 and Fig. 4 (line 1) which follow:

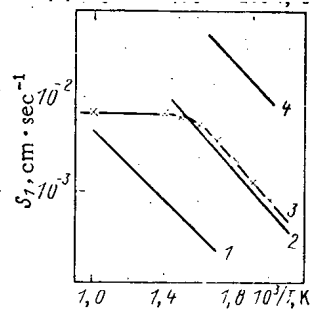$$S_t = 0.4 \exp(-8700 \, \text{cal} /RT). \tag{8}$$

830
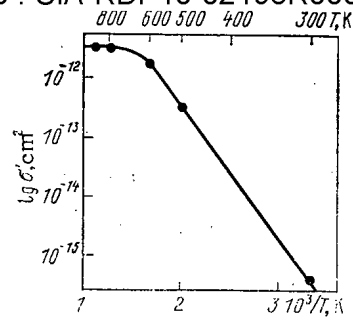
Fig. 4

Fig. 5

Fig. 4. Temperature dependence [11] of the thermal desorption rate (1) and the radiation-induced desorption rate: 2) published data [1]; 3) experiment; 4) published data [11].

Fig. 5. Temperature dependence of the transverse section of radiation-induced reemission: ●) calculated values.

In the general case,

$$S_1 = S_p + S_t, \tag{9}$$

where S_p is the radiation-induced desorption rate. Table 1 shows that the relationship $S_p \gg S_t$ is valid up to 1000°K and that the reemission rate constant of hydrogen on the irradiated side S_1 is determined only by the radiation-induced desorption, i.e., $S_1 = S_p$.

The rate of hydrogen reemission from the stainless steel within the pulse duration in the TM-4 discharge chamber measured [11] at 300 and 600°K was found to be equal to $3 \cdot 10^{-3}$ and $4 \cdot 10^{-2}$ cm/sec, and the variation, may be described by the following equation (cm/sec) (Fig. 4, line 4):

$$S_1 = 60 \exp(-8700 \,\mathrm{cal}\,/RT). \tag{10}$$

Waelbroeck et al. [1] also measured the reemission rate at 300-700°K in the experiments based on the so-called 'Langmuir effect' where the change of hydrogen pressure in the stainless steel chamber was recorded during the glow-discharge period. In order to explain the results of these experiments, the authors [1] used a diffusion equation with the boundary conditions showing quadratic dependence (square-law variation) on the concentration C. The reemission rate constant k_r, $\mathrm{cm}^4 \cdot \mathrm{sec}^{-1}$, and the ratio of the actual surface area to the geometric area σ were found out according to this.

In order to obtain the relationship between S_1 and σk_r, let us compare the equations

$$-D\,\frac{C_1 - C_2}{d} = \alpha Q - S_1 C_1 \tag{11}$$

and

$$-D\,\frac{C_1}{d} = \alpha Q - 2\sigma k_r C_1^2 \tag{12}$$

assuming that the penetration is restricted (controlled) by diffusion, i.e., $S_1 \gg D/d$ and $2/k_r \gg D^2/4d^2Q$. Equating the values of C_1 obtained for Eqs. (11) and (12) (under the condition that $C_1 \gg C_2$) we obtain the following relationship

$$S_1^2 = 2\delta k_r Q, \tag{13}$$

which is used for comparing the published data with the results of the present work. Recalculation of the published data [1] gives the following expression for S_1 (Fig. 4, line 2)

$$S_1 = 16 \exp(-1000 \,\mathrm{cal}\,/RT), \tag{14}$$

which coincides with that obtained in this work.

Apparently, Eqs. (7) and (14) may be considered to be more accurate than Eq. (10) that was obtained from the experiments conducted on such a complex apparatus as TM-4. Evidently, it may be confidently stated that under ion irradiation conditions at relatively low temper-

831

atures $\leqslant 700°K$) the reemission rate of hydrogen from the stainless steel has an exponential dependence on temperature in that the activation energy amounts to ~ 10 kcal/mole (41.9 kJ/mole), whereas, at T > 700°K this rate does not depend on temperature.

We can propose two possible explanations for this phenomenon.

1. The temperature dependence of S_1 indicates the activated nature of the process with an activation energy close to that of thermal desorption (8700 cal/mole or 36.45 kJ/mole), whereas, the radiation-induced desorption rate is clearly independent of temperature [15]. It is possible that accelerated thermal desorption occurs in this case as a result of ion bombardment. From Fig. 4 it follows that such an accelerated thermal desorption is as if it were equivalent to a temperature increase in the surface layer by 300°K.

2. The constant S_1 characterizes the radiation-induced desorption rate and, may be expressed [11] in the following form:

$$S_1 = S_p = \sigma' R_p (\alpha Q),\qquad(15)$$

where R_p is the jump depth of the ions of a given energy in the metal, cm (at an ion energy of 350 eV, $R_p \approx 20-30$ Å); and σ' is the transverse section of radiation-induced desorption, cm^2. In this case, we may assume that σ' is a function of temperature (at T < 700°K). The values of σ' calculated according to Eq. (15) were found to be $4 \cdot 10^{-16}$, $3 \cdot 10^{-13}$, $2 \cdot 10^{-12}$, $3 \cdot 10^{-12}$, $3 \cdot 10^{-12}$ cm^2 at T = 300, 500, 600, 800, and 900°K, respectively (Fig. 5). The variation of σ' with temperature in the range below 700°K may be expressed in the following way:

$$\sigma' = 1.1 \cdot 10^{-8} \exp (-10400 \, cal /RT).\qquad(16)$$

Nonavailability of data on the σ' measurements at temperatures above the room temperature did not make it possible to compare the obtained results. The experimentally determined [12, 13] σ' value for the stainless steel at 300°K using 350 eV bombarding ions was equal to $(2-3) \cdot 10^{-16}$ cm^2; on the other hand, according to the data of McCracken [14], in the case of unannealed stainless steels $\sigma' > 10^{-16}$ cm^2. The derived values are very close to the value calculated from Eq. (16): at 300°K, $\sigma' = 4 \cdot 10^{-16}$ cm^2. This apparently indicates the operation of the radiation-induced desorption process. However, in this case, it is difficult to explain the increase in σ' with increasing temperature: up to as high value as $3 \cdot 10^{-12}$ cm^2 at 700°K. The aforementioned effect may be related to the capture of hydrogem atoms by the defects created at the moment of irradiation whose probability of liberation from these defects increases with increasing temperature. However, additional experiments are required for verifying this hypothesis. In any case, the value $S_1 = 7 \cdot 10^{-3}$ cm/sec, that is obtained at T $\geq$ 700°K and is independent of temperature, forms the ultimate (limiting) value of the hydrogen reemission rate at the bombarding hydrogen ion fluxes amounting to $3 \cdot 10^{16}$ $cm^{-2} \cdot sec^{-1}$.

Table 1 shows that right up to low temperatures, hydrogen penetration through the stainless steel is diffusion controlled ($d/D \gg 1/S_1$, $1/S_t$) in contrast to, for example, molybdenum [15] in which at low temperatures, the penetration is governed by the surface processes. The rate of the surfaces processes (S_1, S_t) becomes comparable to the diffusional discharge rate (D/d) only at T > 1000°K. Using Eq. (5) and the S_1, S_t, and D values given in Table 1, we can evaluate P at high temperatures (see Fig. 1, cross symbols). The observed bend point in the temperature dependence of hydrogen permeability in the high temperature region indicates that in this case, the superficial (surface) stage of penetration begins to play a decisive role. From Eq. (5) it follows that the maximum obtainable permability $P_{max} = \alpha Q$ provided that $1/S_1 \gg 1/S_t$, d/D. However, in the case of the stainless steel, the values of $1/S_1$, $1/S_t$, and d/D are fairly close to each other in the entire range up to T_{melt} and, therefore, P_{max} always remains less than αQ. Thus, at T = 1600°K, the flux $P \approx 3 \cdot 10^{15}$ $cm^{-2} \cdot sec^{-1}$ which is approximately 4 times less than $\alpha Q = 1.2 \cdot 10^{16}$ $cm^{-2} \cdot sec^{-1}$.

CONCLUSIONS

In the entire temperature range under consideration (520-1000°K), the radiation-induced desorption rate is higher than the thermal desorption rate.

In the temperature range below 700°K, the magnitude of hydrogen permeability is determined by the radiation-induced desorption rate that depends on temperature according to the equation

$$S_1 = 18 \exp (-10000 \, cal /RT).$$

$7 \cdot 10^{-3}$ cm/sec.

Above 1000°K, the rates of the radiation-induced desorption, thermal desorption, and diffusional discharge are comparable, and the exponential temperature dependence of flux would be disrupted.

LITERATURE CITED

1. F. Waelbroeck, J. Winter, and P. Weinhold, J. Nucl. Mater., 103-104, 471-475 (1981).
2. M. Brown, B. Emmoth, F. Waelbroeck, and P. Weinhold, J. Nucl. Mater., 93-94, 861-865 (1980).
3. V. M. Sharapov, A. I. Pavlov, and A. P. Zakharov, "Hydrogen permeability of some structural materials under the conditions of low-energy ion bombardment," Zh. Fiz. Khim., 56, No. 5, 1202-1206 (1982).
4. M. Baskes, J. Nucl. Mater., 92, 318 (1980).
5. V. M. Sharapov, A. P. Zahkarov, and V. V. Matveev, "Effect of the glow-discharge parameters on the hydrogen permeability in molybdenum," Zh. Tekh. Fiz., 45, 2002-2004 (1975).
6. K. Wilson and M. Baskes, J. Nucl. Mater., 76-77, 291-297 (1978).
7. V. M. Sharapov, A. I. Pavlov, and A. P. Zakharov, "Hydrogen permeability in nickel from plasma glow-discharge," Zh. Fiz. Khim., 54, No. 11, 2887-2890 (1980).
8. D. I. Slovetskii and R. D. Todesaite, "A study of the mechanism of disintegration of nitrogen molecules in glow-discharge," Khim. Vys. Énerg., 7, No. 4, 291-296 (1973).
9. V. M. Sharapov and A. P. Zakharov, "Peculiarities of hydrogen permeation in molybdenum under glow-discharge conditions," Zh. Tekh. Fiz., 46, 611-614 (1976).
10. K. Wilson, J. Nucl. Mater., 103-104, 453-463 (1981).
11. S. A. Grashin, Yu. A. Sokolov, A. E. Gorodetskii, et al., Interaction of Hydrogen with the Material of the TM-4 Discharge Chamber [in Russian], Preprint IAÉ-3622/7, Moscow (1982).
12. G. Farrell and S. Donnelly, J. Nucl. Mater., 76-77, 322-327 (1978).
13. E. Thomas, J. Appl. Phys., 51 (2), 1176-1183 (1980).
14. G. McCracken, Vacuum, 24, No. 10, 463-467 (1974).
15. A. P. Zakharov and V. M. Sharapov, "Effect of surface processes on the hydrogen permeability of molybdenum," Fiz. Khim. Mekh. Mater., No. 6, 54-58 (1971).

VARIATION OF THE DISLOCATION DENSITY UNDER THE CONDITIONS OF RADIATION-INDUCED SWELLING OF STRONGLY DEFORMED CRYSTALS

Z. K. Saralidze   UDC 539.2/3:648:621.039

The dislocation structure of crystals undergoes considerable changes under irradiation and the dislocation density can either increase or decrease, depending on its initial value. An interesting feature of the evolution of the dislocation structure during irradiation is a tendency toward the attainment of a certain steady-state dislocation density. It is known, e.g., that when annealed (initial dislocation density $\rho_0 < 10^9$ cm^{-2}) and cold-worked ($\rho_0 \approx 10^{12}$ cm^{-2}) austenitic stainless steels are bombarded with fast neutrons, the dislocation density attains the same constant value $\rho_S = 6 \cdot 10^{10}$ cm^{-2} at a neutron fluence $\sim 10^{22}$ cm^{-2} [1].

Since the stresses necessary for dislocation glide do not arise in the crystals during irradiation, it must be assumed that the rearrangement of the dislocation structure of the crystal is caused solely by the climbing of the dislocations, by the annihilation of the dislocations during collision, and the formation of new dislocation loops from the solid solution that is supersaturated with point defects. It is thus of interest not only to elucidate the mechanism responsible for the tendency toward a constant dislocation density and to estimate the steady-state concentration ρ_S, but also to establish what, during the irradiation of the crystals in the free state, causes an uncompensated steady-state flow of

a particular type of point defects to the dislocations, which is necessary for steady-state climb by dislocations.

Edge dislocations have a capability for preferential absorption of interstitial atoms [2-4]. However, this is insufficient for the existence of a steady-state flow of uncompensated interstitials to such dislocations. Such flows can exist only if the crystal contains different sinks with an unlike tendency toward preferential absorption of point defects. It is usually assumed that besides dislocations the crystal contains vacancy pores, which most often are considered as neutral sinks without a tendency toward preferential absorption. In highly deformed crystals, however, pore formation is suppressed until sufficiently high fluences, which lead to a very substantial change in the dislocation density, are attained. Therefore, when explaining the comparatively rapid decrease in the dislocation desntiy in the case of crystals with a high initial density, Bondarenko and Konobeev [5] considered neutral sinks in the form of mixed helical dislocations introduced into the material during deformation. Since this assumption was not sufficiently substantiated, it was considered as a postulate [5].

It should be emphasized that in the case of steady-state spearation of flows of vacancies and interstitials to sinks of unlike types one of the sinks need not be considered to be neutral or capable of preferential absorption of vacancies. All of the sinks can have a tendency toward preferential absorption of any one type of point defect (e.g., interstitials). Nevertheless, if the different sinks have a different tendency toward such preferential absorption, then under steady-state conditions of irradiation one type of sink will absorb predominantly interstitials and the other type predominantly absorbs vacancies.

The stronger elastic interaction of edge dislocations with interstitial atoms than with vacancies is one of the principal causes of preferential absorption of interstitials by edge dislocations. The elastic field of an edge dislocation depends on the orientation of its Burgers vector relative to the crystallograhic axes. Therefore, dislocations with Burgers vectors of different orientation should interact in different ways with different point defects. Accordingly, they should also have different tendencies toward preferential absorption of interstitials. This, as mentioned above, is completely sufficient for the steady-state separation of flows of interstitials and vacancies to dislocations with Burgers vectors of different orientations and as a result conditions are created for steady-state climb of these dislocations during irradiation. The factor η_D of the tendency of dislocations toward preferential absorption of interstitials is usually assumed to be of the order of several per cent. In principle, however, its relative change can be calculated as a function of the orientation of the Burgers vector and the dislocation line and for qualitative analysis we can take $\Delta\eta \approx 10^{-2}$, assuming that this value is not grossly overestimated.

We also note that the presence of preferential sinks of only interstitial atoms produces an excess supersaturation of the crystal with vacancies and, consequently, should be conducive to the nucleation of vacancy pores but not of interstitial dislocation loops. The critical size of interstitial dislocation loops. The critical size of interstitial dislocation loops (if only the small loops do not have an anomalously strong tendency toward preferential absorption of interstitial atoms) under such conditions should be too large and, therefore, the observed loops should have a subcritical size and cannot make any significant contribution to the formation or evolution of the dislocation structure of the crystal. It should be added here that the conditions for the nucleation of interstitial loops do not improve appreciably even when neutral sinks or sinks with a small tendency toward preferential absorption of vacancies are present in the crystal. We shall henceforth assume that the evolution of the dislocation structure of the crystal during irradiation occurs mainly as a result of the climbing of the edge segments of the dislocation network that exists in the crystal and the climbing of helical dislocations that can form from screw segments of dislocations of the probability of this process is sufficiently large.

Two parallel processes can occur during the climb of dislocations: multiplication of dislocations through the formation of new dislocation loops by the Bardeen—Herring mechanism from climbing edge segments [6] and the annihilation of dislocations of opposite sign when they enter into the region of "spontaneous mutual recombination," i.e., when they approach to a distance at which the force of the mutual attraction becomes equal to the force that starts the slip of dislocations. Naturally, when the initial dislocation density is low, the multiplication process will predominate and the dislocation network will become denser under irradiation. Conversely, when the initial density is high, the process of dislocation

834

annihilation will predominate and the dislocation density will increase, a steady-state dislocation density should be established when the rates of the two processes are equal. An exact mathematical description of the process of change in the dislocation structure is extremely complicated. The phenomenological equations presented in [5] for the description of the behavior of the dislocation density contain indeterminate parameters and the applicability of these equations is limited. It is thus desirable to attempt a qualitative description of the time dependence (fluence dependence) of the dislocation density on the basis of fairly simple but physically substantiated assumptions.

Suppose that $\rho(t)$ is the dislocation density and $l \approx \rho^{-1/2}$ is the average length of the segments in the dislocation network. Then the bulk density of dislocation segments $n = (\rho/l) = \rho^{3/2}$. A segment, as a source, can generate a dislocation loop whose radius is commensurate with its length. If v is the velocity of climbing by dislocations, then $\tau_1 \simeq l/v$ is the creation time and $\nu_1 \simeq v/l$ is the rate of creation of loops of size l per unit time by one segment-source. In this case the rate of increase of the dislocation density because of all such sources is (apart from a factor of severalfold) equal to

$$(d\rho/dt)_s \approx nl\nu_1 = \rho^{3/2}v.$$

If z is the number of different possible orientations of the Burgers vector in the crystal, then with an isotropic distribution for the orientation of the dislocations the bulk density of dislocation segments that climb in parallel planes is $n_1 = n/z = \rho^{3/2}/z$. By σ_0 we denote the starting stress for dislocation slip. Then the distance h at which climbing dislocation segments can annihilate is found from the formula $h = b(G/\sigma_0)$, where G is the shear modulus of the crystal. The average distance between segments that climb in parallel planes and are separated by a distance $\leq h$ can be expressed as:

$$\lambda = (n_1 h)^{-1/2} = (\rho^{3/2}h/z)^{-1/2}.$$

The lifetime τ_2 of a climbing dislocation to annihilation will be determined from the condition $\lambda = v\tau_2$. In this case the rate of change of the dislocation density as a consequency of annihilation (to within a numerical factor) is

$$(d\rho/dt)_{an} \simeq (\rho/\tau_2) = (\rho v/\lambda) = \rho^{7/4}(h/z)^{1/2}.$$

Thus, for the rate of change of dislocation density we get the equation

$$(d\rho/dt) = \rho^{3/2}v - \rho^{7/4}v\,(h/z)^{1/2}. \tag{1}$$

The climbing velocity v in the general case can depend on the dislocation density.

The stationary solution of Eq. (1) ($d\rho/dt = 0$), which corresponds to a long irradiation time (large fluence), has the form

$$\rho_s = (z\sigma_0/bG)^2 \tag{2}$$

and does not depend on either the initial plane of the dislocations or their climbing velocity since it is determined only by the structure of the crystal (z) and its mechanical characteristics (σ_0, G). If for a rough estimate we use the values $b = 3\cdot10^{-8}$ cm and $\sigma_0/G = 8\cdot10^{-4}$, then for cubic crystals ($z = 9$, three <100> orientations and six <110> orientations) we get $\rho_s = 5.7\cdot10^{10}$ cm^{-2}, which is close to the value established during the irradiation of stainless steels.

The climbing velocity of an edge dislocation can be written as

$$v = \frac{2\pi}{b\ln(l/r_0)}\,D^{(-)}c^{(-)}\Delta\eta, \tag{3}$$

where b is the Burgers vector, r_0 is the radius of the dislocation core, $D^{(-)}$ is the vacancy diffusion coefficient, $c^{(-)}$ is the steady-state vacancy concentration during irradiation, and $\Delta\eta$ is the orientational difference of the factors of the tendency toward absorption of interstitials by dislocations.

The quasi-steady-state vacancy concentration $c^{(-)}$ can be determined from the condition for the balance of point defects

$$c^{(-)} = \frac{\omega\rho}{4r_c\ln(l/r_0)}\left\{\left[1 + \frac{4r_cQ\ln^2(l/r_0)}{\pi\rho^2 D^{(-)}}\right]^{1/2} - 1\right\}, \tag{4}$$

where r is the radius of spontaneous recombination of point defects and Q is the number of separated Frenkel pairs that form in a unit volume of the crystal per unit time ($K = \omega Q$ is the rate of formation of displacements). For simplicity, Eq. (4) does not make allowance

835

fo_ ...the possible processes of point in the crystal, that is contact in their total diameter
in a unit volume is smaller than the dislocation density.

Substitution Eq. (4) into formula (3) and then into Eq. (1), we get the following
equation for the time dependence of the dislocation density during irradiation:

$$\frac{d\rho}{dt} = \frac{\pi\Delta\eta\omega}{2br_c\ln^2(l/r_0)}\left\{\left[1 + \frac{4r_cK\ln^2(l/r_0)}{\pi\omega\rho^2D^{(-)}}\right]^{1/2} - 1\right\}\left[1 - \left(\frac{bG}{z\sigma_0}\right)^{1/2}\rho^{1/4}\right]\rho^{5/2}. \tag{5}$$

The solution of Eq. (5) in the general form reduces to integration of a fiarly compli-
cated function and, therefore, we shall confine ourselves to consideration of the limiting
cases when Eq. (5) assumes a form that is more accessible to integration.

The expression

$$\xi = (4r_cK\ln^2(l/r_0)/\pi\omega\rho^2D^{(-)}), \tag{6}$$

which appears in formulas (4) and (5), depends on the rate of formation of displacements,
the dislocation density, and temperature. If from the condition $\xi = 1$ we determine the
critical values of these parameters $[T_c(\rho, K), \rho_c(T, K),$ and $K_c(T,\rho)]$, which, naturally,
will depend on the true values of the other two parameters, then clearly when one of the
conditions $T_{irr} \gg T_c(\rho, K)$, $\rho \gg \rho_c(T_{irr}, K)$, or $K \ll K_c(T_{irr}, \rho)$ is satisfied, the para-
meter ξ will be much smaller than unity and Eq. (5) takes on the form

$$\frac{d\rho}{dt} = \frac{\Delta\eta K}{b}\rho^{1/2}[1 - (\rho/\rho_s)^{1/4}], \quad \xi \ll 1, \tag{7}$$

where ρ_s is described by formula (2). This limiting case corresponds to irradiation condi-
tions when the volume recombination can be neglected and the steady-state concentrations of
point defects are determined by the disappearance of the point defects in sinks (in disloca-
tions, in the given case). If one of the conditions $T_{irr} \ll T_c(\rho, K)$, $\rho \ll \rho_c(T_{irr}, K)$, or
$K \gg K_c(T_{irr}, \rho)$ is satisfied, then the main role in the kinetics of accumulation of point
defects will be played by their volume recombination, the parameter will be much greater than
unity, and Eq. (5) assumes the form

$$\frac{d\rho}{dt} = \frac{\Delta\eta K}{b}\gamma\rho^{3/2}[1 - (\rho/\rho_s)^{1/4}], \quad \xi \gg 1, \tag{8}$$

where

$$\gamma = [\pi D^{(-)}\omega/r_cK\ln^2(l/r_0)]^{1/2}. \tag{9}$$

It should be noted that for Eq. (8), unlike the case for Eq. (7), the irradiation temp-
erature is important and the dependence [found from the solution of Eq. (8)] of the disloca-
tion density on the fluence Φ, expressed as the number of displacements per atom ($\Phi = Kt$),
is affected by the rate of formation of displacements (the coefficient γ depends on K). It
should also be borne in mind that Eqs. (7) and (8) can be used to describe the changes $\rho(t)$
over the entire range of time (fluences) if during the irradiation the conditions for their
possible application because of a change in are not violated, i.e., $\rho(t)$ does not intersect
its critical value $\rho_c(T_{irr}, K)$, and the $K_c[\rho(t), T_{irr}]$ do not intersect the real values that
correspond to the conditions of the experiment.

The function $\rho(t)$ cannot be found in explicit form from the solutions of Eqs. (7) and
(8). The functional dependence of the fluence Φ on the dislocation density ρ can be deter-
mined fairly easily,

$$\Phi(\rho) = \frac{4b\rho_s^{1/2}}{\Delta\eta}\left(x_0^{1/4} - x^{1/4} + \ln\frac{x_0^{1/4}-1}{x^{1/4}-1}\right), \quad \xi \ll 1; \tag{10}$$

$$\Phi(\rho) = \frac{4b}{\Delta\eta\gamma\rho_s^{1/2}}\left[\ln\frac{(1-x^{1/4})x^{1/4}}{(1-x^{1/4})x_0^{1/4}} + \frac{3x^{1/2}-2x^{1/4}-1}{2x^{1/2}} - \frac{3x_0^{1/2}-2x_0^{1/4}-1}{2x_0^{1/2}}\right], \quad \xi \gg 1, \tag{11}$$

where

$$x = \rho(t)/\rho_s, \quad x_0 = \rho_0/\rho_s, \tag{12}$$

and ρ_0 is the initial dislocation density, which can be greater than or smaller than ρ_s.

Using formulas (10) and (11), we obtained the plot of the function $\rho(\Phi)$ which, natur-
ally, is affected by the specific values of the parameters that characterize the irradiation
conditions (T_{irr}, K) and the state of the crystal (ρ_0), as well as the constants of the crys-
tal itself. Analysis of Eq. (10), the condition for the applicability of which is easily

836

which is characterized by the initial value $x_0 = 20$, decreases by a factor of roughtly 10 at a fluence of 7 displacements per atom while at a fluence of 15 displacements per atom the values of $\rho(\Phi)$ and ρ_s differ by a mere 4%.

The irradiation of crystals is often accompanied by swelling due to the formation of vacancy pores. For intensive nucleation of pores it is necessary that the critical radius of diffusion development of a pore be fairly small, which is possible only for high steady-state supersaturations of point defects. The critical pore radius R_c can be found from the condition of a zero rate of diffusion change in the pore size,

$$R_c = \frac{2\xi\omega}{kT \ln[1 + \eta_D(c^{(-)}/c_0^{(-)})]} , \tag{13}$$

where ξ is the specific surface energy of the pore, η_D is the factor of the tendency of a dislocation toward preferential absorption of interstitial atoms, and $c^{(-)}$ and $c_0^{(-)}$ are the steady-state and equilibrium vacancy concentrations, respectively.

We assume that the initial dislocation density ρ_0 is sufficiently high. From estimates, $T_c < 800°K$ for $\rho_0 \geqslant 10^{11}$ cm^{-2} even when the rate of formation of displaced atoms is $K = 10^{-3}$ sec^{-1}. If the crystal is irradiated at $T_{irr} > T_c(\rho_0, °K)$, the steady-state vacancy concentration (4) has the form

$$c^{(-)} = \frac{\ln(l/r_0)}{2\pi} \frac{K}{\rho D^{(-)}} \tag{14}$$

and depends significantly on the dislocation density.

The exponential temperature dependence of the parameter $\eta_D c^{(-)}/c_0^{(-)}$ in formula (13) is responsible for the peculiar temperature dependence $R_c(T)$. If we introduce the temperature T*, which is determined from the condition

$$\eta_D c^{(-)}/c_0^{(-)} = 1, \tag{15}$$

then it is easily seen that for $T_{irr} > T*$ the function $R_c(T)$ begins to increase sharply with rising temperature and this should correspond to a rapid decrease in the rate of pore nucleation. This allows the temperature T* to be identified with the high-temperature limit of pore formation (swelling of crystals). Substituting formula (14) into Eq. (15), we get

$$T* = \frac{E_0 + E_m}{k \ln[2\pi\rho D_0^{(-)}/\eta_D K \ln(l/r_0)]} , \tag{16}$$

where E_0 and E_m are energies of vacancy formation and migration and $D_0^{(-)}$ is the preexponential factor of the diffusion coefficient. When $D_0^{(-)} = 10^{-1}$ cm^2/sec, $K = 10^3$ sec^{-1}, and $2\pi/\ln(l/r_0) \approx 1$ the dislocation density decreases from $\rho_0 = 10^{12}$ cm^{-2} to $\rho \simeq 10^{10}$ cm^{-2} can shift T* downward by more than 10%.

Thus, if the initial dislocation density in the crystal is too high ($\rho_0 \gg \rho_s$) and $T_{irr} > T*(\rho_0)$, then the crystal should not swell. However, if $T*(\rho)$ becomes smaller than T_{irr} as ρ decreases during irradiation, the crystal should begin to swell. The time necessary for the dislocation density to decrease to the value determined from the condition

$$T*[\rho(t)] = T_{irr} , \tag{17}$$

will be called the swelling delay time. This time can be determined directly from Eq. (10) if on the left-hand side of the equation ρ is replaced by the solution of (17) with formula (16). It should be pointed out that the value obtained for the delay time cannot be considered to be quantitatively accurate. For a more accurate quantitative description of the processes under consideration it is necessary to know the value of $\Delta\eta$ and the detailed mechanism of evolution of the dislocation structure; this permits an accurate description of the change in the dislocation density with time.

LITERATURE CITED

1. H. Brager et al., in: Proceedings of International Conference on Radiation Effects in Breeder Reactor Structural Materials, Scottsdale, June 19-23 (1977), p. 727.
2. F. Ham, J. Appl. Phys., 30, No. 6, 915 (1959).
3. I. G. Margvelashvili and Z. K. Saralidze, "Influence of the elastic field of a dislocation on the steady-state diffusion flows of point defects," Fiz. Tverd. Tela (Leningrad), 15, No. 9, 2665 (1973).
4. W. Wolfer and M. Ashkin, J. Appl. Phys., 47, No. 3, 791 (1976).

837

6. J. Bardeen and C. Herring, in: Imperfections in Nearly Perfect Crystals, Wiley, New York
   (1952), p. 261.

AUTOMATIC REMOTE MONITORING OF THE SEPARATION PROCESSES OF TRANSPLUTONIUM

ELEMENTS BY ION EXCHANGE

I. V. Tselishchev, N. S. Glushak,   UDC 546.799:66.012.1-52
A. A. Elesin, V. V. Krayukhina,
V. M. Nikolaev, V. V. Pevtsov,
N. I. Pushkarskii, and V. I. Shipilov

Ion-exchange processes are used to produce pure samples of transplutonium elements with a high atomic number from irradiated accumulative reactor targets. The behavior of the elements to be separated in a production line must be carefully monitored because the separation coefficient of these elements in such processes is low, the volumes of the solution with the valuable products are small, and the requirements with respect to purification and yield are high. The monitoring cannot be fully effected by laboratory analyses after taking samples because the analyses take a long time and are laborious and the relative losses of the valuable products are high. Laboratory analyses must be necessarily supplemented by a continuous remote monitoring on the producing line so that information on the development of the processes can be rapidly obtained, optimal fractionation of the products can be performed during the processes, and the number of laboratory analyses can be minimized.

In order to increase the amount of information on the behavior of the elements to be separated in a production line, one employs monitoring systems with a set of detectors corresponding to the specific conditions of the process. For example, the authors of [1] have described the use of BF_3, γ-Ge(Li), and NaI detectors for monitoring the separation of Cm, Am, Cf, and Eu by ion exchange processes. The detectors were mounted near a loop with output to a semiservicing station of the production line, and the information obtained from the detectors was processed in a computer.

The present work concerns an investigation of the possible use of immersed alpha, neutron, and γ-NaI detectors and of an information retrieving and processing system as described in [2] for monitoring ion exchange processes in the separation of ^{253}Es and ^{252}Cf. In the process to be monitored, first Es and thereafter Cf are washed out and the separation coefficient amounts to ~1.4. The required purification and yield of Es are attained by a three-step refining of the initial mixture. The remote monitoring system must reliably determine the limits of the Es fraction and the beginning of the Cf washing-out. When the Cf concentration is relatively high in the mixture to be separated, one employs in the first stages of the process immersed alpha and neutron detectors for the monitoring and immersed α- and γ-NaI detectors in the last stage. Certain characteristic features of the nuclides to be monitored are listed in Table 1 in terms of nuclear physics; the table includes the parameters of the detectors employed.

An immersed n-silicon surface-barrier detector is employed for measuring the ^{253}Es and ^{252}Cf concentrations from the α-activaty [3]. The α-spectrum obtained with the aid of such a detector from a mixture of those nuclides in a nitric acid solution is illustrated in Fig. 1. The specific overall α-bulk activity of the solution is determined with a formula of [4]:

$$\gamma = \eta N, \tag{1}$$

where γ denotes the specific α-bulk activity (Bq/ml); η denotes the detector calibration coefficient (Bq·sec/(ml·pulse)) determined in measurements of the α-activity of standard solutions) and N (pulses per sec) denotes the repetition frequency of the pulses on the 20% discrimination level. The relative concentration of the α-emitters is obtained with formulas of [5]:

meters

| Nuclide	Immersion detector for alpha particles, area 10 mm², resolution 1%					Gamma-NaI detector, 25 × 25 mm, resolution 8% (660 keV)		Neutron detector, area 25 mm²	
	Specific α-activity (Bq/μg)	α particle energy (keV)	Sensitivity threshold (μg/ml) for particles	Specific activity (Bq/μg) of spontaneous fission	Sensitivity threshold (μg/ml) for fission fragments	Energy (keV) of the main gamma lines and of the x-ray radiation	Sensitivity threshold (μg/ml) for gamma radiation	Specific activity (neutron/(sec · μg)) for neutrons	Sensitivity threshold (μg/ml) for neutrons
^{252}Cf	$1,9 \cdot 10^7$	6118	$0,5 \cdot 10^{-4}$	$6,2 \cdot 10^5$	$0,8 \cdot 10^{-3}$	41; 97	$1 \cdot 10^{-4}$	$2,3 \cdot 10^6$	$0,4 \cdot 10^{-1}$
^{253}Es	$9,3 \cdot 10^8$	6632	$0,1 \cdot 10^{-5}$	—	—	42; 77; 112	—	—	—
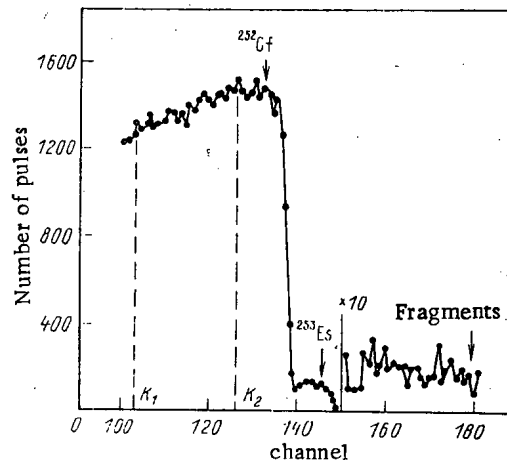
Fig. 1. α-Spectrum obtained for the ^{252}Cf and ^{253}Es mixture with an immersion detector.
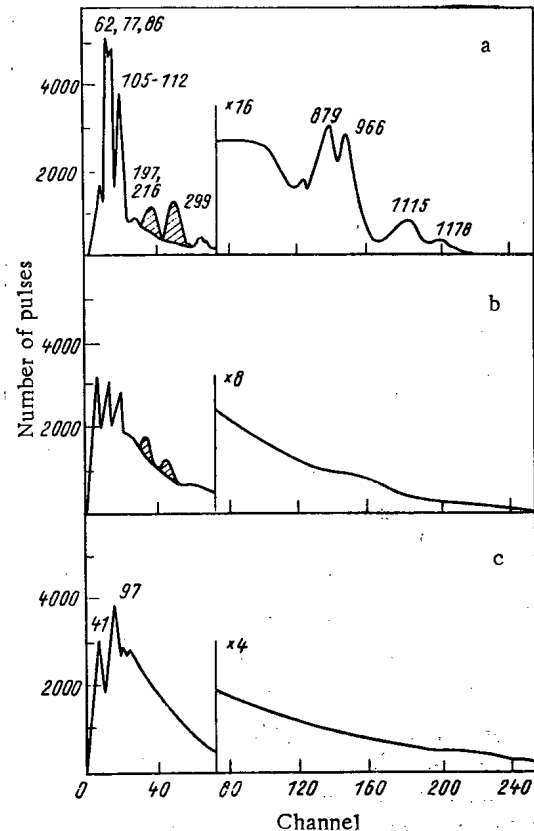
Fig. 2. γ-Spectra obtained with an NaI detector; a) ^{160}Tb and ^{253}Es; b) ^{160}Tb, ^{253}Es, and ^{252}Cf; c) ^{252}Cf; the numbers at the peaks denote the energy values (keV).

$$\varepsilon_l = h_l - h_{l+1}; \tag{2}$$

$$h_l = \sum_k n_k \, (C_0 + C_1 k)/\sum_k (C_0 + C_1 k)^2, \tag{3}$$

where h_l denotes the relative concentration of the l-th α-emitter; n_k, contents of the k-th channel of the α-spectrum; and C_0 and C_1, parameters of the linear dependence which describes the distribution function of the number of α-particle over the energy; this dependence is obtained with the least-square method for the spectral section from k_1 to k_2 (see Fig. 1). The concentration K_1 of the l-th α-emitter is (expressed in μg/ml)

$$K_l = \gamma \varepsilon_l / a, \tag{4}$$

where a denotes the specific α-activity (Bq/μg) of the nuclide; γ, total specific α-bulk activity (Bq/ml); and ε_l, relative concentration of the l-th alpha emitter in the solution. Es and Cf were separately determined through their α-activity in the interval $0.1 < \varepsilon_1 < 0.9$ when the results of the laboratory analysis coincided within the error limits.
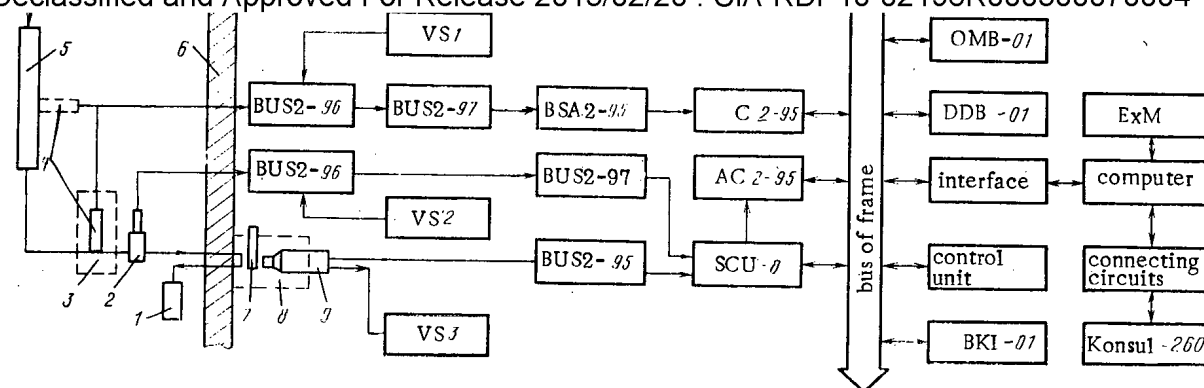
839

Fig. 3. Structure of the monitoring system: 1) receiving vessel; 2) flow cell with immersed alpha detector; 3) neutron shield made of polyethylene; 4) detector of fast neutrons; 5) column; 6) shield of the chamber or box; 7) box for gamma samples; 8) lead shield; 9) 6931-17 NaI detector; BUS2-96) preamplifiers; BUS2-95 and BUS2-97) amplifiers; VS1-VS3) voltage supplies; BSA2-95) discriminator; C2-95) counter; AC2-95) amplitude converter; SCU-8) switch control unit; OMB-01) operational memory block; DDB-01) data display block; BKI-01) timer; ExM) external memory of the 1530-17 type.

Additional information on the ^{252}Cf concentration in the solution is obtained by recording fragments of spontaneous fission with the aid of an immersed alpha detector. The amplitude of the pulses resulting from ^{252}Cf fission fragments substantially exceeds (by about one order of magnitude) the amplitude of the pulses generated by the α-particles; therefore, by recording the fission fragments, the Cf concentration can be precisely determined, and this is particularly important at high loads in the α-measuring channel (more than 10^4 pulses per sec) when the resolution of the α-spectra is significantly reduced.

A fast-neutron sensor is used to measure the neutron flux from the ^{252}Cf. The sensor is a silicon surface barrier detector with an area of 25 mm^2. A thin layer of a hydrogen-containing material (lucite) was applied to the sensitive surface of this detector. Though the sensitivity of such a detector is relatively low, one can obtain with this detector useful information on the ^{252}Cf concentration at various points of an ion-exchange unit.

A spectrometric 6931-17 NaI detector (25 × 25 mm) with a resolution of 8% for the 660-keV line is employed for recording the γ-radiation of the nuclides to be separated. The main contribution to the γ-radiation of the solutions to be monitored is provided by ^{160}Tb which is the chemical analog of Es and which is washed out together with the latter. This detail makes it possible to determine the relative ^{253}Es concentration of the solution from the area of the ^{160}Tb photopeaks at 200-300 keV (Fig. 2). The ^{252}Cf concentration is assessed from the repetition frequency of the pulses resulting from the remaining part of the spectrum and generated by the γ-radiation and from the neutron flux from ^{252}Cf; this part of the spectrum is determined by subtracting the contribution produced by ^{160}Tb and ^{253}Es from the total spectrum.

The structure of the monitoring system is systematically illustrated in Fig. 3. The immersed α-sensor is mounted in flow cell of the production line inside a hot chamber or hot box. The neutron sensor records the neutron flux at the output of the production line or at another point of the unit (the dashed lines indicate the position of the detector in the scanning of a column). The γ detector is mounted near a production line loop which was extended into the service area. The information supplied by the sensors is processed with an information-retrieving and processing system. The system under consideration is distinguished from the previously described system of [2] by equipment with channels for measuring the γ-radiation (6931-17 detector, supply block VN3, and BUS2-95 amplifier) and the neutron flux (neutron detector, BUS2-96 preamplifier, BUS2-97 amplifier, BSA2-95 discriminator, and supply block VS1).

The program for the operation of the monitoring system is designed for testing individual units, calibrating the measuring channels, periodic connection of the sensors during process monitoring, processing of the information arriving from the sensors, and outputing of the results of the measurements on a printer or the screen of the data display unit. The
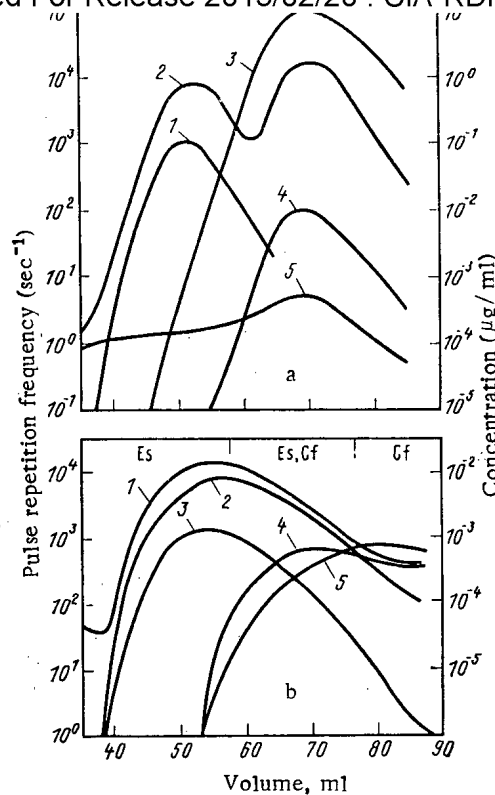
Fig. 4. Results of the monitoring of the separation of ^{253}Es from ^{252}Cf: a) with the aid of immersed α- and neutron detectors; b) with the aid of immersed α and γ detectors.

program and the initial data are inputted from magnetic tape or from the computer keyboard. The results of measurements made with the α-sensor are outputted as concentration of the nuclide (Bq/ml or μg/ml) on a printer, whereas the recordings of the fission fragments, of the neutron flux, and of the γ-radiation are outputted as pulse repetition frequency (pulses per sec), which corresponds to the relative concentration of the elements to be separated. The periodicity of the measurements depends upon the dynamics of the process and is 100-300 sec. Each measurement has its particular number and time which corresponds to the solution volume passed through. The results of the monitoring of the entire process are recorded in an external memory and can be displayed on a screen of the data display unit as curves of washing out; these results can be additionally processed (calculation of the purification, extraction).

Figure 4a illustrates an example of remote monitoring on a line for separating ^{253}Es and ^{252}Cf via the α activity, fission fragments, and the neutron flux. The α-monitoring (curve 2) facilitates the determination of the front edge, the position of the maximum, and the beginning of the drop of the curve of Es washing-out. The front edge of the Cf washing-out curve is determined mainly from fission fragments (curve 4) and the neutron flux (curve 5), because at a high load in the α-measuring channel, it is hard to separately determine ^{252}Cf on the ^{253}Es background. The gently sloping front edge of curve 5 of monitoring the ^{252}Cf concentration through neutrons can be explained by insufficient shielding from the spurious neutron flux and by the low sensitivity of the neutron detector. Curves 1 and 3 reflect the change of the ^{253}Es and ^{252}Cf concentrations according to the laboratory analysis data of individual samples. The results obtained with γ-monitoring are shown in Fig. 4b. In the particular case, the α-activity in the solution monitored results mainly from ^{253}Es (curve 2), and the total γ activity (curve 1) is composed of the activity of ^{160}Tb (curve 3) and the activity of ^{252}Cf (curve 4). Curve 5 indicates the change in the ^{252}Cf concentration according to laboratory measurements on individual samples in a neutron unit. It follows from the examples that the results of remote monitoring on a production line rather precisely describe the behavior of the elements to be separated and are close to the results of laboratory analyses in a wide variability range of the concentrations, as well as in cases of various Es and Cf ratios in the initial mixtures. α- and γ-monitoring are the basic monitor-

841

ing processes, whereas additional monitoring involves fission fragments and neutrons. The sensitivity of the neutron detector can be increased by increasing the sensitive surface area, and the background in the neutron channel can be reduced by employing appropriate neutron shields.

It was therefore shown in the example of the separation of ^{253}Es from ^{252}Cf that when immersed α-, neutron, and γ-NaI detectors and an information-retrieval- and processing system are used in the automatic remote monitoring of ion-exchange processes for the separation of transplutonium elements with high atomic numbers, the elements to be separated can be operationally observed in the production line during the process and an additional processing of the results of the monitoring after termination of the monitoring is possible. The information obtained is a necessary supplement to the analysis data of samples and helps to reach optimal fractionation of the products with a minimum number of laboratory analyses. When the set of detectors used becomes greater, the detector parameters are improved, and the information retrieving and processing system reaches a faster response, ion exchange, and extraction processes in the separation of transplutonium elements can be successfully monitored in the case of a complicated nuclide composition of the solution treated while requirements in regard to fast execution of the measurements and their accuracy are being met.

LITERATURE CITED

1. M. Wakat and S. Peterson, Nucl. Technol., 17, 49 (1973).
2. V. A. Bikineev, N. S. Glushak, and V. V. Pevtsov, "An automatic system for monitoring the production process of separating transplutonium elements," At. Énerg., 55, No. 3, 179 (1983).
3. V. V. Pevtsov, "An immersed alpha-spectrometry detector," Prob. Tekh. Eksp., 4, 78 (1976).
4. M. I. Krapivin, M. P. Malafeev, et al., "Immersed semiconductor detectors for the determination of the specific alpha-activity of solutions," in: Reports of the First Symposium of the SEV "Research in the Processing of Irradiated Fuel," Vol. 3, Atomic Energy Commission of Czechoslovakia, Prague (1977), pp. 188–201.
5. E. A. Vznuzdaev and V. I. Orlov, "An analysis of alpha spectra of transuranium radionuclides obtained from thick uniform sources," Prib. Tekh. Eksp., 1, 57 (1982).

DEPENDENCE OF THE MEAN VALUE AND FLUCTUATIONS OF THE ABSORBED ENERGY
ON THE SCINTILLATOR DIMENSIONS

F. M. Zav'yalkin and S. P. Osipov   UDC 539.16

In [1, 2], it was shown that the level of signal fluctuations at a detector output depends on the number of γ quanta and the spread of their absorbed energy; the dependence of the mean absorbed energy $\overline{E}_{ab}$ and accumulation coefficient of the fluctuations ξ on the radius of a cylindrical NaI(Tl) scintillator (thickness 7 cm) for 1.25-MeV γ quanta was described; and it was established that $\xi_{max} = 3-4$. In [3], the dependence of the amplitude-distribution coefficient $\eta = \sqrt{\xi}$ on the radius of the cylindrical scintillator was investigated for large values of the recording efficiency (0.5–0.9). A method of estimating the maximum value of η as a function of the energy spectrum of the radiation incident on the crystal was proposed, and analytical expressions were obtained. It was shown that η does not exceed 1.2–1.4 for scintillators of different materials and monoenergetic sources and for sources with a continuous spectrum cannot be larger than 1.5.

The presence of such contradictory and partial data and the need to know the dependence of the mean absorbed energy $\overline{E}_{ab}$ and accumulation coefficient of the fluctuations ξ on the scintillator dimensions for designing scintillator detectors of the ionizing radiation operating in the current-recording mode means that the above-noted dependences must be investigated. This problem takes on special importance in designing multichannel systems,
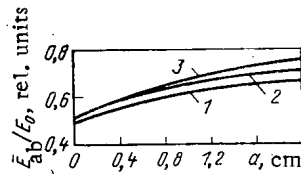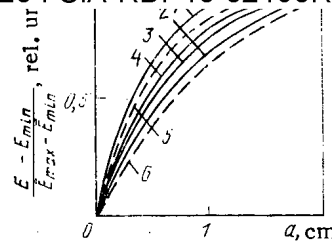
Fig. 1   Fig. 2

Fig. 1. Dependence of $\overline{E}_{ab}$ on the radius of the cylindrical CsI scintillator at an energy of 1000 keV; 1) l = 2.5 cm; 2) 5; 3) 10.

Fig. 2. Dependence of $\overline{E}_{ab}$ on the radius for various energies and crystal materials when l = 5 cm; 1) E_0 = 250 keV; 2) 1000; 3) 1750; 4) 2500; 5) 1000, $CdWO_4$; 6) E_0 = 1000 keV, plastic.

multilayer detectors [4] for tomographical apparatus, and spectrometers based on deriving the radiation spectrum [5] from the experimental absorbed-energy distribution.

In the present work, the mean absorbed energy and accumulation coefficient of fluctuations for cylindrical scintillators made from materials covering the density and atomic-number ranges employed ($CdWO_4$, CsI, plastics), of radius a and length l for a narrow photon beam of energy E_0 incident on the crystal along the cylinder axis is calculated. The accumulation coefficient of the fluctuations is determined by the mean square deviation δ_0 of the energy absorbed by the detector material $\xi = 1 + \delta_0^2$. Using the dispersion property of the random quantity $\sigma^2 x = \overline{x^2} - \overline{x}^2$, it was found that $\xi = \overline{E_{ab}^2}/\overline{E}_{ab}^2$. No account is taken of electron leakage in the calculations. The interaction coefficients of γ quanta with materials are taken from [6]. The Monte Carlo method is used in the calculations, taking account of the recommendations made in the present work.

Typical curves of $\overline{E}_{ab}$ as a function of the radius a of the cylindrical CsI scintillator for various crystal lengths and E_0 = 1000 keV. As is evident, with increase in scintillator radius, the function $\overline{E}_{ab}$ increases with increase in saturation from minimal $\overline{E}_{min}$ (the approximation of a needle-shaped scintillator, $a \approx 0$) to maximal $\overline{E}_{max}$ value of the absorbed energy ($a = \infty$). This is explained in that, beginning at some radius, γ-quantum lekage through the front and rear surfaces of the scintillator will predominate over leakage through the side surface; this effect is increased as the photons leaving through the side surface lose a larger proportion of their energy in the crystal than those leaving through the rear surface.

It follows from Fig. 1 that, when l = 2.5 cm, saturation sets in more rapidly than when l = 5 cm and l = 10 cm. Thus, the rate of absorbed-energy accumulation decreases with increase in crystal length. This is explained by increase in the proportion of energy leakage through the side surface.

The dependence of the mean absorbed energy on the radius is also determined by E_0 and the scintillator material (Fig. 2). Comparison of curves 1-4 shows that the rate of accumulation of $\overline{E}_{ab}$ with increase in E_0 at first decreases since there is a sharp decrease in the proportion of the photoeffect, and then increases because forward-scattered photons predominate in the quantum leakage. In analyzing curves 2, 5, 6, increase in density of the scintillator material with increase in rate of accumulation of $\overline{E}_{ab}$ is established; this is associated with increase in the influence of the photoeffect.

On the basis of analysis of the results obtained, it is possible to describe the dependence of the mean energy absorbed in a crystal of radius a

$$\overline{E}_{ab} = \overline{E}_{min} + (\overline{E}_{max} - \overline{E}_{min})(1 - e^{-ga}), \tag{1}$$

where g is a coefficient depending on E_0, l, and the crystal material; E_{max}, E_{min} are expressed in terms of E_0. The error with which Eq. (1) approximates the theoretical data is no more than 1%.

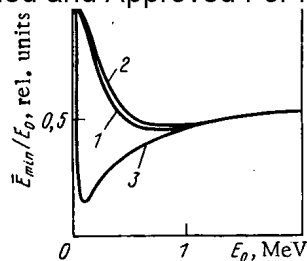The value of $\overline{E}_{min}$ is found [3] using the Klein–Nishina–Tamm formula

843

Fig. 3. Dependence of $\overline{E}_{min}$ on E_0;
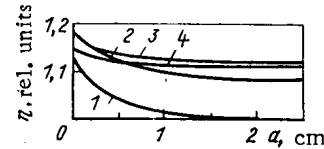1) CsI; 2) CdWO$_4$; 3) plastic.

Fig. 4. Dependence of η on a for
the CsI crystal: 1) $E_0 = 250$ keV;
$l = 2.5$ cm; 2) 1000, 2.5; 3) 1000,
10; 4) 1750, 2.5.

TABLE 1. Coefficients t, b_1, b_2 for Various Scintillator Materials

Coefficient	Plastic	CsI	CdWO$_4$
t	0,51	0,85	0,75
b_1	1,51	2,01	2,33
b_2	0,25	0,61	0,73

$$\overline{E}_{min} = \frac{\mu_{ph}}{\mu} + \frac{E_0 - 1{,}02}{E_0} \frac{\mu_b}{\mu} \frac{C}{2\mu} \left[\frac{-20\alpha^4 + 102\alpha^3 + 186\alpha^2 + 102\alpha + 18}{3\alpha(1 + 2\alpha)^3} - \frac{2\alpha + 3 - \alpha^2}{\alpha^2} \ln(1 + 2\alpha) \right], \qquad (2)$$

where E_0 is the energy, MeV; μ, linear attenuation coefficient of γ radiation of energy E_0 by the scintillator material μ_{ph}, attenuation coefficient of the radiation as a result of the photoeffect; μ_b, attenuation coefficient of the radiation due to pair creation; $\alpha = E_0/511$; C, a coefficient proportional to the number of electrons per cm^3 of the scintillator material.

The dependence of $\overline{E}_{min}$ on E_0 calculated from Eq. (2) for various crystal materials is shown in Fig. 3. The minimal energy at first falls sharply with increase in E_0. This is because of the sharp decrease in influence of the photoeffect in the range $E_0 = 0-5$ MeV. Then $\overline{E}_{min}$ increases slowly, since the proportion of energy lost in the crystal from the recorded quantum increases. For CdWO$_4$, $\overline{E}_{min}$ is larger when $E_0 < 1$ MeV than for CsI, on account of the large contribution of the photoeffect to the total linear attenuation coefficient of the radiation. Beginning at $E_0 = 1$ MeV, $\overline{E}_{min}$ is practically the same for CsI and CdWO$_4$ (0.5-1%). For plastic, $\overline{E}_{min}$ is less than for CsI and CdWO$_4$, and the minimum is reached earlier, which is explained by the absence of a photoeffect for $E_0 \geqslant 0.2$ MeV.

The function $\overline{E}_{max}$ depends on E_0 as well as the length and the material of the scintillator. With increase in l from 0 to infinity, $\overline{E}_{max}$ increases monotonically from $\overline{E}_{min}$ to 1. With increase in E_0, the behavior of $\overline{E}_{max}$ is the same as that of $\overline{E}_{min}$.

The dependence of $\overline{E}_{max}$ on the crystal length may be approximated with an error of 1.5-3% by the expression

$$\overline{E}_{max} = \overline{E}_{min} + (1 - \overline{E}_{min})(1 - e^{-fl}). \qquad (3)$$

Here f is a coefficient depending on E_0; $f = t\mu(E_0)$, where t depends on the scintillator material (Table 1).

The coefficient $g(E_0, L)$ determines the rate of increase in $\overline{E}_{ab}$, its dependence on E_0 is qualitatively described above. For $l = 0$, the function $g = \infty$; when l tends to infinity g tends to a constant value. The function $g(E_0, l)$ may be described by the formula

$$g(E_0, l) = b_1\mu + \frac{b_2}{\mu l}. \qquad (4)$$

The values of the coefficients b_1, b_2 for various types of crystals are given in Table 1. The minimum values of E_{ab} calculated by the Monte Carlo method and from Eq. (2) are in good agreement; the deviation is no more than 0.7-1%.

844

To find the mean accumulation coefficient of the fluctuations of absorbed energy, $\overline{E}^2_{ab}$ is calculated. The dependence of $\overline{E}^2_{ab}$ on a, l, E_0, and the type of crystal is completely analogous to the dependence of $\overline{E}_{ab}$ on a, l, E_0, and the type of crystal. The dependence of the accumulation rate of $\overline{E}_{ab}$ and $\overline{E}^2_{ab}$ on a is the same for each set of l, E_0, i.e., the dependence of $\overline{E}^2_{ab}$ on a may be described by the formula

$$\overline{F}^2_{ab} = \overline{E}^2_{min} + (\overline{E}^2_{max} - \overline{E}^2_{min})(1 - e^{-ga}), \tag{5}$$

where $\overline{E}^2_{min}$, $\overline{E}^2_{max}$ are expressed in units of E_0^2. The limiting minimal value of the mean square absorbed energy is [3]

$$\overline{E}^2_{min} = \frac{\mu_{ph}}{\mu} + \frac{(E_0 - 1.02)^2 \mu_{ab}}{E_0^2 \mu} + \frac{C}{\alpha^2}\left[\frac{-68\alpha^5 + 184\alpha^4 + 566\alpha^3 + 494\alpha^2 + 180\alpha + 24}{3(1+2\alpha)^4} - \frac{2\alpha + 4 - \alpha^2}{\alpha}\ln(1+2\alpha)\right]. \tag{6}$$

The dependence of $\overline{E}^2_{max}$ on E_0 and l is written analogously to Eq. (3)

$$\overline{E}^2_{max} = \overline{E}^2_{min} + (1 - \overline{E}^2_{min})(1 - e^{-l\mu(E_0)l}).$$

The values of $\overline{E}^2_{min}$ calculated by the Monte Carlo method and from Eq. (5) coincide with an error of 0.7–1%.

The accumulation coefficient of the fluctuations may be determined from Eqs. (1) and (5)

$$\xi = \frac{\overline{E}^2_{min} - (\overline{E}^2_{max} - \overline{E}^2_{min})(1 - e^{-ga})}{[\overline{E}_{min} + (\overline{E}_{max} - \overline{E}_{min})(1 - e^{-ga})]^2}. \tag{7}$$

It was noted in [3] that the dependence $\eta = \sqrt{\xi}$ is approximated by a linear function if the scintillator the thickness is sufficiently large. As shown by the results of machine calculations, this is not true for small thickness. Theoretical curves of η as a function of the radius a of a cylindrical scintillator for different l and different values of the energy are shown in Fig. 4. At small crystal thickness, η does not depend on the radius; when $\mu h = 0.2-2$, this dependence is significant on both the thickness and the crystal diameter. At large scintillator thickness, η is approximately the same. Since η decreases to some value with increase in diameter, it is possible to approximate the dependence of η on a by a formula analogous to Eqs. (1) and (5); the rate of decrease of η is analogous to the rate of accumulation of $\overline{E}_{ab}$ and $\overline{E}^2_{ab}$, that is

$$\eta = \eta_{max} + (\eta_0 - \eta_{max})e^{-ga}, \tag{8}$$

where the coefficients g, η_{max} depend on l, E_0, and the type of scintillator; η_0 depends on E_0 and the type of scintillator. Equation (8) is more convenient than Eq. (7). The value of η_0 is determined from $\overline{E}_{min}$ and $\overline{E}^2_{min}$. The dependence of η_{max} on l may be obtained from the dependences $\overline{E}^2_{max}(l)$ and $\overline{E}_{max}(l)$.

The results obtained are only valid for monoenergetic sources. The specific feature of the use of a nonmonoenergetic source for radiometric measurements in the mean-current recording mode is that $\eta \neq 1$ for a total-absorption crystal. The values of $\overline{E}_{ab}$ and $\overline{E}^2_{ab}$ may be found from the formulas from [3] and from Eqs. (1)-(6).

The value of η may be calculated for total-absorption crystals and sources with a discrete spectrum. It is found that η is no greater than 1.07 (^{88}Ra). It is not difficult to estimate η for total-absorption crystals and x-ray sources. The Kramers energy spectrum [7], disregarding the high-energy component, is

$$f(E) = \frac{2(E_0 - \overline{E})}{E^2},$$

where E_0 is the maximum energy in the spectrum and

$$\overline{E} = \int_0^{E_0} Ef(E)\,dE, \quad \overline{E}^2 = \int_0^{E_0} E^2 f(E)\,dE.$$

Then $\eta = 1.5$. If the high-energy component is taken into account, then

$$\eta = \sqrt{\frac{1.5(E_0 + 4B)(E_0 + 2B)}{(E_0 + 3B)^2}}, \tag{9}$$

845

where b is the coefficient of the high-energy component [7]. It follows from Eq. (9) that $\eta < 1.5$. The theoretical values of the limiting η for Shiff bremsstrahlung spectra with maximum energy $E_0 = 10\text{-}15$ MeV according to the experimental data of [8] are in good agreement (discrepancy no more than 3%) with the values obtained from Eq. (9). This is because the physical nature of the bremsstrahlung radiation does not depend on E_0, i.e., the Shiff and Kramers spectra are adequate from a physical viewpoint.

Any barrier between the bremsstrahlung source and the detector hardens the spectrum and hence decreases the accumulation coefficient of the fluctuations. In this case $\overline{E_{ab}}$ and $\overline{E_{ab}^2}$ are determined from the formulas of [3] and from Eqs. (1)-(5).

Theoretical investigations and Monte Carlo calculations allow the dependence of the absorbed energy and the accumulation coefficient of the fluctuations on the dimensions, type of crystal, and radiation spectrum incident on the crystal to be estimated. The results obtained may be used to estimate the expected signal and signal/noise deviations or to select the minimal dimensions of the cylindrical scintillator on the basis of the required signal/noise ratio. The results may also be used to establish the radiation spectrum from a known absorbed-energy distribution over the radius or length of the cylindrical scintillator.

<div align="center">LITERATURE CITED</div>

1. A. A. Maiorov, S. V. Mamikonyan, L. I. Kosarev, and V. T. Firstov, Radioisotopic Defectoscopy (Methods and Apparatus) [in Russian], Atomizdat, Moscow (1976).
2. V. I. Gorbunov et al., Radiometric Radiation-Monitoring Systems [in Russian], Atomizdat, Moscow (1976).
3. F. M. Zav'yalkin, Yu. G. Zubkov, and S. P. Osipov, "Dependence of the signal/noise deviation on the radius of a cylindrical scintillator," Defektoskopiya, No. 11, 56-59 (1984).
4. R. Alvarez and A. Macovski, "Energy-selective reconstructions in x-ray computerized tomography," Phys. Med. Biol., 21, 733-744 (1976).
5. A. S. Kék, "Machine tomography using x-rays, radioactive isotopes, and ultrasound," Tr. Inst. Inzh. Électrotekh. Radioélektron., 67, No. 9, 79-110 (1979).
6. Handbook on Radiational Protection for Engineers [in Russian], Vol. 1, Atomizdat, Moscow (1972).
7. X-Ray Engineering [in Russian], Vol. 1, Mashinostroenie, Moscow (1980).
8. V. A. Vorob'ev, V. I. Gorbunov, et al., Betatrons in Defectoscopy [in Russian], Atomizdat, Moscow (1973).

MEASUREMENT OF THE RATIO OF THE ^{236}U AND ^{235}U FISSION CROSS SECTIONS
IN THE NEUTRON-ENERGY RANGE 0.34-7.4 MeV

B. I. Fursov, M. P. Klemyshev,
B. F. Samylin, G. N. Smirenkin,
and Yu. M. Turchin

UDC 539.173.84

The present work continues a cycle of measurements of the fission cross sections of nuclides [1, 2] in the neutron-energy range that is most important for fast-reactor calculations by the method described in [1]. Neutrons were generated in T(p, n) and D(d, n) reactions in solid targets from titanium hydride on copper substrates ($E_n < 1$ MeV) or scandium hydride on molybdenum substrates while tritons and deuterons were accelerated in the electrostatic accelerators of the Physics and Power Engineering Institute, Obninsk. The energy resolution, which depends on the target thickness and the solid angle in which the fissionable layer was located, was $\Delta E_n = \pm 30\text{-}40$ keV in the region of the ^{236}U fission threshold and increased to $\pm 100\text{-}200$ keV for $E_n \leqslant 3.8$ MeV. A fissionable triuranium octaoxide (U_3O_8) layer of diameter 10-15 mm and thickness 0.3-0.5 mg/cm² was deposited onto thin ($\leqslant 0.1$ mm) substrates of polished aluminum (Table 1). The fission fragments were detected by a double ionization chamber. The efficiency of fission chambers for ^{235}U and ^{236}U was 98.3 and 98.8%, respectively. We used B/A layers for measurements of the energy dependence of the ^{236}U/^{235}U

TABLE 1. Isotopic Composition of Fissionable Nuclei, at. %

Laver	Principal isotope	^{234}U	^{235}U	^{236}U	^{238}U
A	^{235}U	0,0010	99,9955$\pm$0,0010	0,0035	0,0005
B	^{236}U	<0,001	0,047$\pm$0,002	99,845$\pm$0,005	0,107$\pm$0,002
C	^{236}U	<0,001	3,002$\pm$0,009	96,87$\pm$0,10	0,13$\pm$0,02
D	^{236}U	<0,001	4,973$\pm$0,015	94,90$\pm$0,09	0,13$\pm$0,02

TABLE 2. Results of Calibration of $\sigma_f(^{236}U)/\sigma_f(^{235}U)$ with ^{238}U Layers of Different Isotopic Compositions

Calibra-tion	Layer	E_n, MeV			
		1,475	2	2,5	3
I	C/A	0,538$\pm$0,009	0,633$\pm$0,009	0,687$\pm$0,011 *	0,713$\pm$0,012
II	D/A	0,542$\pm$0,008	0,631$\pm$0,008	0,688$\pm$0,010	0,718$\pm$0,011
Average		0,540$\pm$0,006	0,632$\pm$0,006	0,688$\pm$0,007	0,716$\pm$0,008

*The structure of the errors of this measurement is given in Table 4.

ratio of fission cross sections and we used C/A and D/A layers for calibrations. Calibration was carried out to measure the ratio of fissionable ^{236}U and ^{235}U layers by a method that makes it possible to obtain highly accurate results in analogous measurements of fission cross sections of ^{238}U and ^{235}U [1]. In the ionization chamber ^{236}U layers (C and D), with a ^{235}U impurity that is well known from mass-spectroscopic measurements, was mounted in contact with ^{235}U layers (A). The ionization chamber was placed in a polyethylene-moderated neutron flux from an accelerator. Since ^{236}U does not possess subbarrier fissionability, the slow neutrons cause fission of only the ^{235}U nuclei in each layer. In the case of irradiation with slow neutrons the fissions that occurred when the detector was covered with a 0.5-mm layer of cadmium were subtracted from the number of fissions with the detector opened. The cadmium ratio for ^{235}U was about 20, the correction to the ratio of the number of fissions in the ^{236}U and ^{235}U layers did not exceed 0.3-0.5%, and the energy of the neutrons prior to moderation was 400 keV [the T(p, n) reaction was used]. To eliminate the blocking of one layer by another we irradiated them in turn from the front and back side of the detector and averaged the results.

After the slow-neutron measurements the moderator block was removed and a cycle of measurements of the ratio of the ^{236}U and ^{235}U fission cross sections was performed with the same layers for neutrons possessing energies of 1.475, 2, 2.5, and 3 MeV (Table 2). To measure the energy dependence of the ratio of the ^{236}U and ^{235}U fission cross sections over the entire range, including the subbarrier region, we used the B layer of ^{236}U, which contained no less than 0.05% ^{235}U. The energy dependence curve was normalized to values averaged over two calibrations for E = 1.475, 2, 2.5, and 3 MeV, which were measured with an average error of ~1.1%. Since the measurements were carried out in a continuous beam of accelerated particles, great attention was paid to the determination of the components of the neutron background. The influence of neutrons scattered by the walls of the experimental room was taken into account through the deviation from the ~R^{-2} law with the distance of the detector from the accelerator target. This component of the background did not exceed 0.4% for $E_n \leqslant 3.6$ MeV and 0.7% for E_n = 3.8-7.4 MeV.

It was important to make correct allowance for the background of neutrons scattered by the structure of the accelerator target. The correction for this component was found from measurements with an increased effective thickness of the material of the target structure by a factor of two and then three, followed by linear extrapolation of the results to zero thickness. The layer of water (0.25 mm) that cooled the target was simulated with polyethylene. The correction for the ratio of the fission cross sections of ^{236}U and ^{235}U was 1-2.2% over the range 1.475-3.6 MeV, increased to 5% for 0.338 MeV, and did not exceed 0.3-1.2% for the region $E_n \geqslant 3.8$ MeV.

847

Ratio of the ²³⁶U and ²³⁵U Fission Cross Sections ... urement of the Ratio of the ²³⁶U and ²³⁵U Fission Cross Sections for E_n = 2.5 MeV (calibration I)

E_n, MeV	ΔE_n, keV	σ^6/σ^5	Δ stat.	Δ tot.	E_n, MeV	ΔE_n, keV	σ^6/σ^5	Δ stat.	Δ tot.
0,338	40	0,00209	4,8	5,2	2,30	68	0,682	0,2	1,5
0,387	38	0,00274	4,6	5,0	2,40	68	0,691	0,3	1,5
0,436	36	0,00400	3,7	4,2	2,50	67	0,685	0,4	1,6
0,484	34	0,00574	2,9	3,5	2,60	66	0,685	0,3	1,6
0,535	33	0,00823	2,6	3,2	2,70	66	0,689	0,4	1,6
0,584	33	0,0112	2,5	3,1	2,80	65	0,695	0,3	1,5
0,633	32	0,0163	2,1	2,8	2,90	65	0,699	0,3	1,5
0,683	32	0,0274	2,0	2,7	3,00	65	0,712	0,2	1,6
0,732	32	0,539	1,8	2,5	3,10	65	0,719	0,2	1,6
0,782	31	0,0991	1,5	2,3	3,20	65	0,727	0,2	1,6
0,832	31	0,141	1,2	2,1	3,30	65	0,739	0,3	1,6
0,882	31	0,194	0,8	1,9	3,40	66	0,746	0,3	1,6
0,931	30	0,263	0,6	1,8	3,50	66	0,750	0,4	1,7
0,981	32	0,283	0,5	1,7	3,60	66	0,758	0,4	1,8
1,030	32	0,289	0,9	2,5	3,80	240	0,773	0,7	2,0
1,079	32	0,337	0,6	1,8	4,00	174	0,774	0,3	1,9
1,129	32	0,401	0,8	1,8	4,20	161	0,779	0,4	1,9
1,178	33	0,448	0,5	1,7	4,40	142	0,784	0,4	1,8
1,227	33	0,494	0,3	1,6	4,60	133	0,787	0,4	1,8
1,276	33	0,547	0,4	1,6	4,80	118	0,788	0,5	1,8
1,326	33	0,559	0,4	1,7	5,00	112	0,785	0,4	1,7
1,376	34	0,560	0,3	1,6	5,20	106	0,791	0,5	1,6
1,426	34	0,557	0,3	1,6	5,40	104	0,796	0,4	1,6
1,475	34	0,542	0,3	1,6	5,60	102	0,803	0,7	1,8
1,524	34	0,524	0,4	1,6	5,80	125	0,805	1,0	2,0
1,574	35	0,534	0,3	1,6	6,00	122	0,812	1,1	2,1
1,624	35	0,558	0,4	1,6	6,20	120	0,811	1,1	2,2
1,674	35	0,582	0,3	1,6	6,40	117	0,831	1,2	2,4
1,800	73	0,604	0,2	1,6	6,60	116	0,855	1,0	2,3
1,900	72	0,615	0,2	1,6	6,80	116	0,880	0,9	2,4
2,00	71	0,636	0,2	1,5	7,00	117	0,888	0,8	2,4
2,10	70	0,651	0,3	1,5	7,20	118	0,893	1,0	2,5
2,20	69	0,663	0,3	1,5	7,40	119	0,867	1,3	2,7

Source of corrections and errors	Correction, %	Error, %
Statistics of fast-neutron measurements		0,5
Fission of impurity isotopes (excluding ²³⁵U) by fast neutrons	<0,1	0,1
Energy dependence of the fission-fragment detection efficiency	0,7	0,3
Background of neutrons: scattered on the target structure	1,6	0,7
from concomitant (p, n) reactions	1,9	0,2
from the expt. room	0,4	0,3
Inelastic scattering of neutrons	—	0,5
Error of the energy dependence of the ratio of the ²³⁶U and ²³⁵U fission cross sections	—	1,1
Rel. content of ²³⁵U nuclei in the ²³⁶U layer (see Table I)		0,3
Error of slow-neutron measurements	—	1,0
Difference of the neutron fluxes in the ²³⁶U and ²³⁵U layers	1,1	0,5
Total error	—	1,6

The measurements performed indicated a considerable dependence of the results on the background of neutrons from concomitant (p, n) and (d, n) reactions in scandium and molybdenum, which are incorporated into the composition of the target and its substrate, as a consequence of an abrupt change in the ²³⁶U fission cross section in the region of the threshold and the comparatively low energy of the background neutrons. These components of the background were measured on models simulating the target (molybdenum with deposited scandium but without tritium or deuterium). The main and background measurements were made many times on a set of targets and models and the results were averaged. In the background measurements it was important to reproduce identical conditions for the targets and models owing to the dependence of the background (d, n) reactions not only on the integral of the current but also on the time, i.e., the "history" of the irradiation.

The number of fissions of ²³⁵U nuclei reached 9% for 3.6 MeV in the case of the (p, n) reaction. The correction to the ²³⁶U/²³⁵U fission cross-section ratio in this case was 5.5% and decreased to 0.1% for 1.475 MeV. In the case of the (d, n) reaction the total number of ²³⁵U fissions for 7.4 MeV reached 32% with a correction of 16.4% to the ²³⁶U/²³⁵U fission cross-section ratio and a decrease to 0.8-1.2% for 3.8-5.4 MeV. By means of calculations we introduced corrections to the results of the measurements. It was most important to make allowance for the fission of isotope impurities in measurements in the subthreshold region (E_n = 0.34-0.84 MeV) and calibration measurements. The influence of ²³⁴U and ²³⁸U is negligible.

The energy dependence of the efficiency of detection of fission fragments by ionization chambers made it possible to take into account the fraction of fission fragments that are completely absorbed by layers of finite thickness or that generate pulses with an amplitude below the discrimination threshold. The correction incorporates the motions of the fissionable nucleus in the laboratory coordinate system because of the momentum transferred by a neutron and also incorporates the angular distributions of the fission fragments. The values of the angular anisotropy of the fission were taken from [3] for ²³⁵U and from [4, 5] for
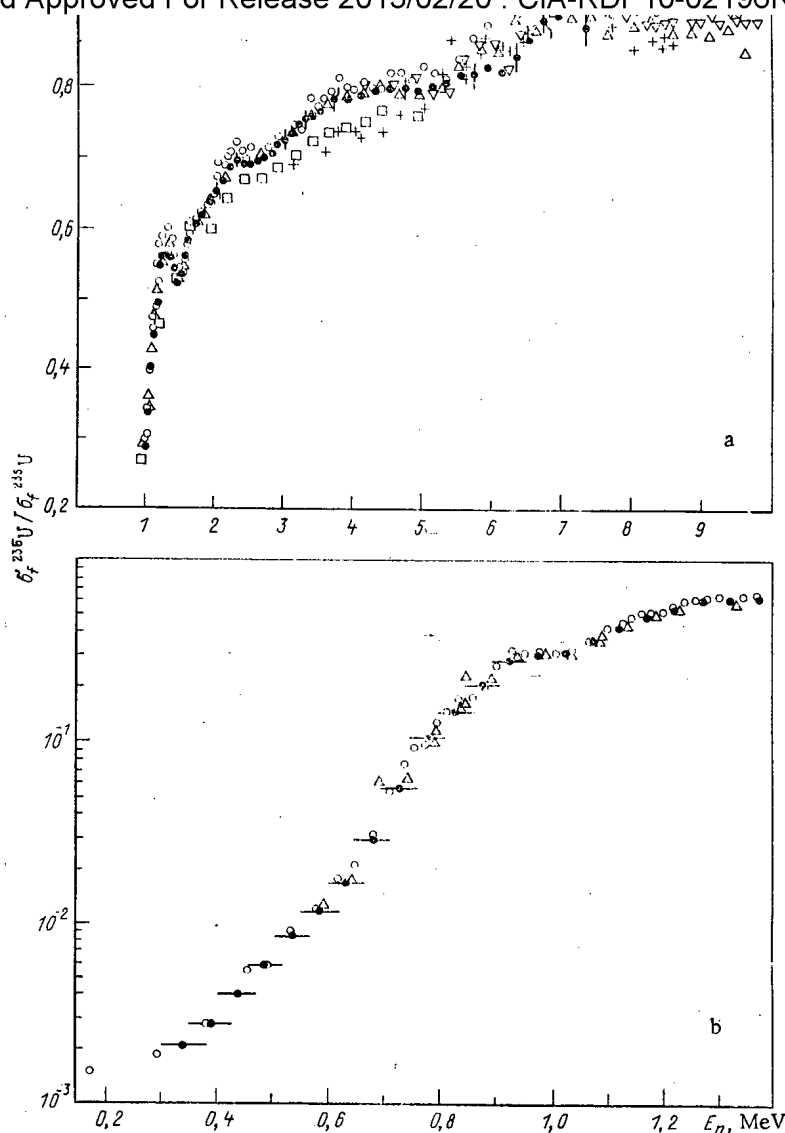
Fig. 1. Ratio of the ^{236}U and ^{235}U fission cross sections:
a) region of the "plateu"; b) subbarrier energy region; ●) re-
sults of this work; Δ) data from [6]; ○) data from [7]; ▽) data
from [8]; +) data from [9]; □) data from [10].

^{236}U. A small correction allowed for the difference in the neutron fluxes through the ^{236}U
and ^{235}U layers, separated by the electrode of the ionization chamber and the substrates of
the layers. According to estimates the inelastic scattering of neutrons on the material of
the detector, electrodes, and substrates of the layers is small. The upper estimate of this
effect (0.5%) was added to the resultant error. The results obtained in this work are pre-
sented in Table 3. It indicates the statistical error, which was determined from the scat-
ter of the results, and the total error, which is the root-mean-square sum of all the in-
determinacies found. Table 4 gives the structure of the characteristic errors and the errors
of one calibration measurement at 2.5 MeV. The part that determines the energy dependence
of the ^{236}U/^{235}U ratio of fission cross sections (1.1%) was separated from the total error.
The systematic part of the total error (1.2%) which was correlated over the entire energy
range studied consisted of the squares of the average accuracy of the calibration values
(1.1%, Table 2) and the error of the normalization of the energy dependence to reference
values (0.5%). Besides the statistical error, the errors due to the experimental measure-
ments and the computational corrections were incorporated into the error of the energy de-
pendence. The largest contribution came from the scattered-neutron background (1.2% for
0.338 MeV) and concomitant (d, n) reactions (1.8% for 7.4 MeV). The total error of measure-
ment of the ratio of ^{236}U and ^{235}U fission cross sections was 1.5-2% in the range 1-5.6 MeV

849

background, and increased to 5.2% for 0.338 MeV because of a deterioration of the statistical accuracy of the measurements of the subbarrier region of ^{236}U fission.

Figure 1 compares the results of this work with those of other authors. It should be pointed out that there is satisfactory agreement with the results of [6] except for individual values in the range 6-7 MeV. The data of [7] have higher values (by 2-4%) over the entire range studied while in the range $E_n > 5.5$ MeV this difference reaches 5-10%. The results of [8] are in agreement with the data of this paper over the combined energy range but are 3-5% higher for individual values of the energy for $E_n > 5.7$ MeV. The results of [9] in the range 3-5 MeV and the data of [10] in the range 2-5 MeV are systematically below the results of this work.

The authors express their thanks to E. Yu. Baranov for participation in the work.

LITERATURE CITED

1. B. I. Fursov et al., At. Énerg., 43, No. 3, 161 (1977).
2. B. I. Fursov et al., At. Énerg., 43, No. 4, 261 (1977); 44, No. 3, 236 (1978); 45, No. 6, 440 (1979); 46, No. 1, 35 (1979); 55, No. 1, 3 (1983).
3. J. Meadows and C. Budtz-Jorgensen, Rep. ANL-NDM-64 (1982).
4. R. Leachman and L. Blumberg, Phys. Rev., 137, No. 4B, 814 (1965).
5. Kh. D. Androsenko et al., Vorp. At. Nauki Tekh. Ser. Yad. Konstanty, No. 1 (40), 50 (1981).
6. J. Meadows, Nucl. Sci. Eng., 65, 171 (1978).
7. J. Behrens and G. Carlson, Nucl. Sci. Eng., 63, 250 (1977).
8. A. A. Goverdovskii et al., in: Neutron Physics [in Russian], Vol. 2, TsNIIAtominform (1984), p. 193.
9. C. Nordborg, and H. Conde, in: Proceedings of a Conference on Neutron Physics, Harwell (1978), p. 910.
10. W. Stein et al., in: Proceedings of a Conference on Neutron Cross Sections and Technology, Vol. 1, Washington, D.C. (1968), p. 627.

HIGH-TEMPERATURE STRENGTH OF THE 10Kh18N9 STEEL IN THE MEDIUM OF CARBON-
CONTAINING SODIUM AT 500°C

O. V. Starkov, I. P. Mukhin,   UDC 620.171.32
V. V. Chukanov, and V. D. Zhelnin

During the operation of fast neutron reactors with sodium coolant, the intermediate
heat exchanger of the second loop made from the 10Kh18N9 stainless steel is subjected to
static and dynamic loads. In the presence of a carbon source, the stainless steel 10Kh18N9
may undergo carburization leading to a change in its high-temperature strength and ductility
[1]. In view of this, it is necessary to study the effect of carbon-containing sodium on
the long-term strength, creep rate, and elongation of the 10Kh18N9 austenitic steel at 500°C.

The tests on the long-term strength and creep of the 10Kh18N9 steel in carbon-contain-
ing sodium and in pure sodium were carried out at 500°C on plain specimens measuring 4 mm
in width and 1 mm in thickness, and having a gauge length of 17.5 mm under a constant ten-
sile load in a specially designed leak-tight system. All the components of the system in-
cluding the specimen grips that are in contact with sodium were made from the steel
0Kh20N14S2. An insert (sleeve) made from the U10 carbon steel served as a carbon source.
The surface area of the insert in contact with sodium was 37.5 cm^2 and the surface area of
the components of the system and the specimen amounted to 350 cm^2.

Filling up the system with sodium (156 cm^3) and hermetic sealing were carried out in a
vacuum glove box using pure argon atmosphere. The control (reference) steel specimens were
also tested using such an arrangement in pure sodium. The plain specimens of steel were
heat treated in a regime of heating up to 1100°C, subsequent holding for a period of 10 min,
and air cooling.

The rate of carbon absorption by the chromium-nickel steels through sodium increases
with increasing temperature and increasing carbon-source area, and slows down with time
[2]. The established quantitative regularities [3, 4] of carburization of the austenitic
steels 10Kh18N10T and 10Kh16N15M3B from different carbon sources permit one to simulate the
carburization conditions of the heat exchanger tubes (metal-metal) of the second loop made
from the 10Kh18N9 steel from a low-alloy pearlitic steel 10Kh2M (structural material of the
steam generators) acting as a carbon source. In the general case, neglecting the stresses,
the amount of carbon absorbed by the steel is given by the equation $\Delta m \simeq P\tau^{0.5}$. Here, P is
the carburization parameter determining the carburization ability (carburizability) of the
system as a whole. For the second loop working with sodium at 500°C and at equal surface
areas of the source S_s and the carbon absorber S_a, $P \approx 1\cdot10^{-3}$ mg·cm^{-2}·h$^{-0.5}$. In the experi-
ments, we used a strong carbon source in the form of U10 steel which gives $P = 1\cdot10^{-2}$ mg·
cm^{-2}·h$^{-0.5}$ at $S_s/S_a \simeq 1{:}9.4 \simeq 0.1$ based on the published data [2, 4]. For an equal quantity
of carbon to be absorbed by the 10Kh18N9 steel from the sources comprising the steels U10
and 10Kh2M ($P_1\tau_1^{0.5} = P_2\tau_2^{0.5}$), it follows that when the 10Kh2M steel is used as a carbon
source, the experimental duration must be 100 times greater than that required when the U10
steel is used. Thus, the experiments for evaluating the high-temperature strength of the
10Kh18N9 steel were carried out under the conditions approximately simulating carburization
from the pearlitic steel over a period of 100,000 h. However, it must be noted that the
effect of these conditions on the mechanical properties is more pronounced than that under
the actual conditions because of the occurance of all-sided (multidirectional) carburiza-
tion; in the actual structures, we observe one-sided (unilateral) carburization.

The analytical dependences of time-to-fracture τ on the stress σ obtained using the
method of least-square [5, 6] have the following forms

$$\lg \sigma = -0.1830 \lg \tau + 1.7648 \tag{1}$$

when tested in pure sodium and
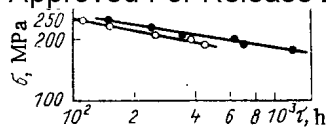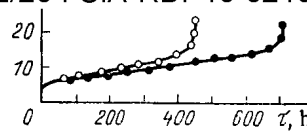
Fig. 1   Fig. 2

Fig. 1. Stress dependence of the time-to-fracture of the steel 10Kh18N9 in Na (○) and in Na + C (●) at 500°C.

Fig. 2. Creep curves of the steel 10Kh18N9 at 500°C in Na (○) and Na + C (●) at σ = 190 MPa.
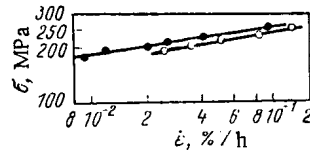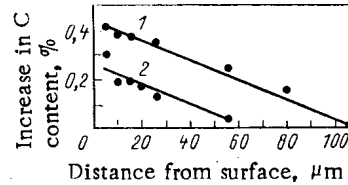

Fig. 3   Fig. 4

Fig. 3. Stress dependence of the steady-state creep rate of the steel 10Kh18N9 when testing in Na (●) and Na + C (○) at 500°C.

Fig. 4. Variation of carbon content across the thickness of a 10Kh18N9 steel specimen after testing in Na + C for a period of 1250 h (1) and 630 h (2) at 500°C.

$$\lg \sigma = -0.1544 \lg \tau + 1.7268 \tag{2}$$

when tested in carbon-containing sodium. The corresponding plots (Fig. 1) show that the presence of carbon in sodium increases the long-term strength of the steel and improves the creep resistance in that this effect is observed during the stage of steady-state creep (Fig. 2). Figure 3 shows that at 500°C, carbon-containing sodium leads to a decrease in the steady-state creep rate by approximately 50%. In this case, the difference between the corresponding creep rates increases with increasing test duration, i.e., with decreasing load.

The stress dependence of the steady-state creep is described by the following equations:

$$\lg \sigma = 0.1653 \lg \dot{\varepsilon} + 1.5411 \tag{3}$$

when tested in pure sodium and

$$\lg \sigma = 0.1414 \lg \dot{\varepsilon} + 1.5470 \tag{4}$$

when tested in carbon-containing sodium.

Metallographic analysis showed the formation of a frontal zone of increased etchability (measuring 12 μm in depth) on the surface of the 10Kh18N9 steel specimens subjected to creep tests in carbon-containing sodium for a period of 1250 h. The formation of microcracks was also observed on the specimen surface. We did not find variation in the microhardness across the cross section of the steel specimen (2.2×10^3 MPa). The fracture of steel occurs across the grains and along the grain boundaries. The specimens tested in carbon-free sodium did not show any corrosive damage. Microcracks were found on the surface of the fractured specimens also, but their number is significantly less than that observed during the tests in carbon-containing sodium. In this case also, the fracture of steel is both transgranular and intergranular.

The order to study the corroded zone and the changes in the carbon, chromium, and nickel contents in the 10Kh18N9 steel subjected to tensile tests for 630 and 1250 h in carbon-containing sodium, we studied the "oblique" sections of the specimens using an electron-probe microanalyzer "Camebax." An insignificant carburization of the surface layer was recorded (maximum by 0.4% of the initial carbon content). In this case, the carbon content and the

852

the steel (Fig. 4). No changes in the chromium and nickel contents were found across the cross section of the steel specimens. We evaluated the diffusion coefficient D of carbon in the unstabilized austenitic steel along the depth of carburization, and found it to be $D = (5-9) \cdot 10^{-12} \text{ cm}^2/\text{sec}$.

LITERATURE CITED

1. R. Snyder, K. Natesan, and T. Kassner, "Kinetics of the carburization–decarburization process of austenitic stainless steels in sodium," Trans. Am. Nucl. Soc., 16, 112–213 (1973).
2. B. A. Nevzorov, V. V. Zotov, V. A. Ivanov, and O. V. Starkov, Corrosion of Structural Materials in Liquid Alkali Metals [in Russian], Atomizdat (1977), pp. 140–206.
3. O. V. Starkov, B. A. Nevzorov, and I. N. Luk'yanova, "Aggressive action of carbonaceous impurities in liquid sodium on structural steels," Zashch. Met., 7, No. 6, 674–678 (1971).
4. O. V. Starkov and I. N. Luk'yanova, "Carburization of austenitic steels in sodium coolant," ibid., 10, No. 3, 255–260 (1974).
5. E. N. Pustyl'nik, Statistical Methods of Analysis and Observations [in Russian], Nauka, Moscow (1965), p. 288.
6. N. D. Sazonova, Testing Heat Resistant Materials for Creep and Long-Term Strength [in Russian], Mashinostroenie, Moscow (1965), pp. 160–175.

A MATERIALS-TECHNOLOGY INVESTIGATION OF THE CONTROL ROD BUSHES

OF REACTOR TYPE BOR-60

V. N. Golovanov, A. V. Povstyanko,
V. S. Neustroev, V. M. Kosenkov,
E. P. Klochkov, and V. K. Shamardin

Further study of the behavior of the various parts of the core is needed to ensure a high degree of reliability and work capability in fast reactors. This includes the compensating-rod bushes [1, 2]. For this reason, an investigation was carried out into a bush type KS-1 of reactor BOR-60, irradiated in the third row of the core to a maximum neutron flux of $16.5 \cdot 10^{26} \text{ m}^{-2}$ (E > 0.1 MeV) and then removed from the reactor when the compensating rod jammed.

Bush type KS-1 takes the form of a hexagonal tube made of Kh18N10T steel, measuring 44 mm over the key, with a cylindrical bore of 42 mm. The distributions of flux and temperature throughout the height of the bush during irradiation in the reactor are given in Fig. 1.

Geometry of Hexagon and Swelling of Material after Irradiation

External inspection of the upper part of the bush revealed parts with highly modified shapes. The centers of the faces were markedly concave with respect to the ribs, starting from center of the core up to a level of z = +170 mm. A reduction in the cross-sectional area of the bush was observed at a level of z = +140 mm when checking the bore, bringing it to the diameter of the compensating rod. The size of the hexagonal bush was measured at three points beneath the key, across the faces of the hexagon for the three pairs of faces B—E, A—D, and C—F along the part from z = —70 to z = +250 mm (Fig. 2).

The swelling of the material of the KS-1 bush was determined by reference to the perimeter of the hexagon and the height of the core (see Table 1). A high degree of uniformity in the swelling of the material of the rib (12.1–19.3%) and of the face (5.6–16.7%) was observed at a level of z = +80 mm, corresponding to the greatest change in shape.
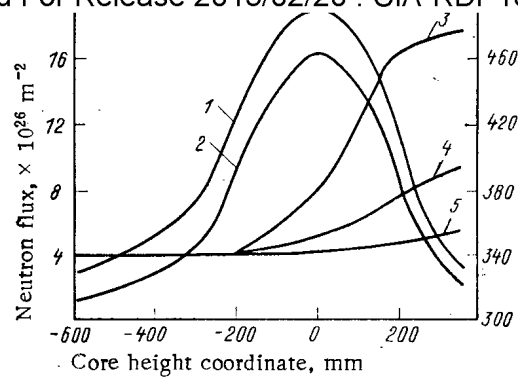
853

Fig. 1. Variation in neutron flux and temperature throughout the height of bush type KS-1 (from the center of the core) when irradiated in a BOR-60 reactor: 1) neutron flux E > 0; 2) neutron flux E > 0.1 MeV; 3) temperature of outer surface of hot face of bush; 4) temperature of inner surface of hot face; 5) temperature of outer surface of cold face.
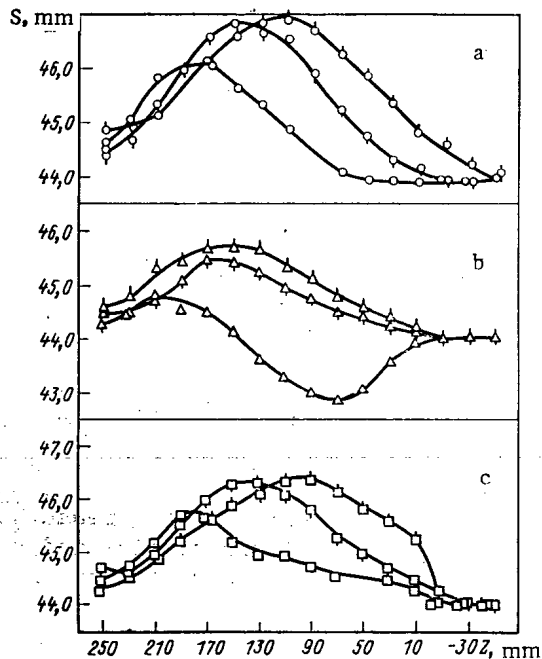

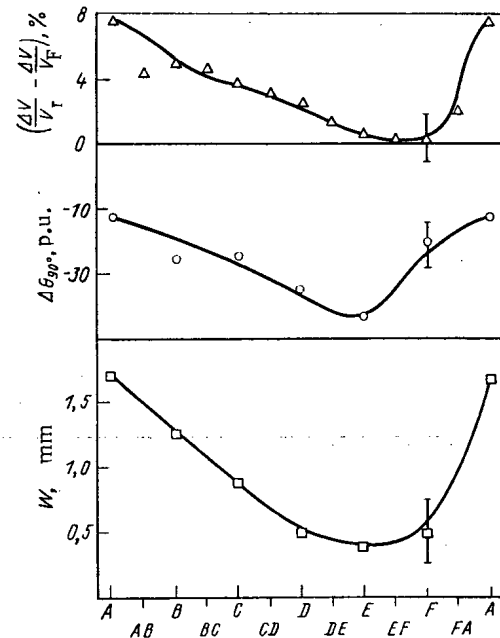Fig. 2. Dimensions below key (s) of hexagonal bush type KS-1 throughout the height of the core (z) for three pairs of faces: a) B–E; b) A–D; c) C–F.

Fig. 3. Variation in dimensions of swelling of rib $\Delta V/V_r$ and face $\Delta V/V_f$, residual stresses ($\Delta\theta_{90}°$) and bending of the face (W) about the periphery of a hexagonal bush type KS-1 (z = +80 mm).

TABLE 1. Swelling of Material of Hexagonal Bush Type KS-1 Throughout Height of Core

	Swelling $\Delta V/V$, %					
z, mm	face A	rib AB	face B	rib BC	face C	rib CD
+140	11,6	16,8	15,2	21,0	14,7	20,3
+80	5,4	12,4	11,0	18,5	15,4	19,3
+20	5,1	13,1	6,0	10,0	6,6	13,2

854

According to the investigation, the "jamming" of the compensating rod was caused by swelling of the steel. The centers of the faces (especially face A) were concave, leading to a constriction of the bore. We found that the swelling was nonuniform about the periphery of the bush. This implied that a similar nonuniformity existed throughout the section of the bush walls, since the temperature of the outer surface was considerably higher than that of the inner surface (see Fig. 1). The nonuniform thickness of the wall of the bush about its periphery (1 mm at the center of the face rising to 3 mm at the rib) and the non-uniformity of the swelling about the periphery and section of the wall lead to the appearance of stress and a corresponding bending moment that was at its maximum in the center of the face and was directed towards the center of the hexagon. These stresses in their turn must have given rise to a radiation-induced creep and bending of the faces of the hexagon.

The conditions of operation are bound to have an effect on the changes in shape of the bush. Two materials-technology assemblies were found in the neightborhood of the SU-3 bush during the course of the first four microruns and the temperature of two faces of the bush hardly exceeded that of the incoming coolant (see Fig. 1). A considerably difference must have existed between the swelling of the "hot" and "cold" faces of the bush, according th existing data on the relationship of the swelling of steel mark Cr18Ni10Ti to neutron flux levels and temperature [3] for a neutron flux of $5 \cdot 10^{26}$ m^{-2} (E > 0.1 MeV). Since the first swellings took place more rapidly at the cold surface, an additional stress will arise after the gap between assemblies is taken up and the bending of the bush will take place relative to the cold face.

These ideas are confirmed by comparing the changes in three characteristics about the periphery of the hexagon: the difference in swelling between the rib and the center of the face, the residual macrostresses in the center of the face, and the bending of the plane of the face (Fig. 3). In fact, face A experiences the minimum swelling (see Table 1), due to which the difference between the swelling at the center of the face and the adjoining ribs is a maximum and the residual stress a minimum.

Our investigations of the control rod bush of a BOR-60 reactor shows that the change in shape of the bush in cross section is mainly determined by the nonuniformity in the thickness of the wall, the temperature gradient about its periphery and section, the swelling, and radiation-induced creep of the steel.

LITERATURE CITED

1. D. Michel and H. Smith, "Properties of reactor alloys after neutron or particle irradiation," ASTM STP-570, Am. Soc. Testing Mater., 156 (1975).
2. V. A. Krasnoselov, V. M. Kosenkov, E. M. Loboda, et al., "A materials technology study of the compensating rod bush of reactor type BOR-60 after irradiation at $1.6 \cdot 10^{23}$ neutrons/cm^2 (E > 0.1 MeV)," At. Énerg., 44, No. 3, 228-231 (1978).
3. N. P. Agapova, Vopr. At. Nauki Tekh., Ser. At. Mater., No. 4(15), 12 (1982).

QUANTITATIVE ESTIMATES OF THE ENERGY OF PULSED X RAYS BACKSCATTERED
BY AIR

V. D. Kosarev and V. P. Mukhin   UDC 539.171:539.12

The advantages of devices using the backscattering of x rays [1-3] are responsible for their wide application in automatic control systems of various objects.

Frequency, amplitude, and start—stop x ray measuring devices have been adequately studied and described [2, 3]. At the same time there is no adequate theoretical basis for stroboscopic measuring devices [4] based on the relation between the energy flux density of backscattered gamma rays recorded during a time interfal (gate) and a measurable parameter. In particular, the air background has a substantial effect on the results of measurements of the characteristics of an object under study in devices employing the backscattering of x rays.

In analyzing x-ray measuring systems people generally consider the characteristics of the field of an instantaneous point monochromatic isotropic radiation source specified by a delta function [1, 5], since a pulse of any shape and length can be represented by superposing data for instantaneous sources [1].

To obtain quantitative estimates of pulsed x rays backscattered by air (air background) we assume that the source S and the detector D coincide and are located in an infinite air medium (Fig. 1). Here R is the radius of the front of the x-ray pulse, and ΔR is the thickness of the air layer from which backscattered rays enter the gate of length Δt ($\Delta t = 2\Delta R/c$), where c is the speed of light. The source radiates x rays of energy E_0 into a unit solid angle. The radiation backscattered from air is estimated in the single-scattering approximation, since multiple scattering of γ rays can be neglected within a mean free path [5].

We estimate the backscattering from a layer of air by using the well-known formulas for backscattering from a spherical interface between two media [3]. In an air medium this surface can be taken as a hemisphere (Fig. 1) with the detector and radiator at its center, and a vacuum between O and R. For a displacement of this boundary by ΔR we obtain the energy flux density of radiation at the detector which was backscattered from the layer of thickness ΔR.

$$E_{\text{u}}(\Delta R) = E_0 A_e \frac{1-\cos \Psi_0}{R^2} \left[1 - \frac{\exp(-2\mu_0 \Delta R)}{\left(1 + \frac{\Delta R}{R}\right)^2} \right] \exp(-2\mu_0 R), \tag{1}$$

where A_e is the energy albedo of air; μ_0, is linear absorption coefficient for the radiation; and ψ_0, angle of collimation.

For a short gate length ($\Delta R/R \ll 1$) we expand the exponential in the square brackets and retain the first two terms. Then Eq. (1) takes the form

$$E_{\text{u}}(\Delta R) = E_0 A_e \frac{2\mu_0 \Delta R (1-\cos \Psi_0)}{R^2} \exp(-2\mu_0 R). \tag{2}$$

For a known geometry and a constant energy E_0 the air density was the greatest effect on backscattering from air. To estimate this effect for normal incidence and backscattering (Fig. 1) and an infinitely thick scatterer we can write the albedo in the form [6]

$$A_e = \frac{d\sigma}{d\Omega} \frac{n_e}{2\mu_0}, \tag{3}$$

where $d\sigma/d\Omega$ is the differential Compton scattering cross section per electron, and n_e is the concentration of free electrons in air.

Expressing n_e in terms of the running density ρ of air, the linear absorption coefficient μ_0 in terms of the absorption coefficient $\mu(0)$ at the initial density ρ_0, and substituting these values into (2), we obtain

0038-531X/85/5904-0856$09.50
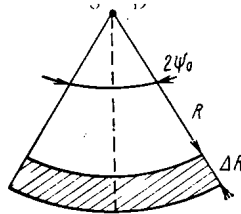
Fig. 1.   Geometry of the problem.

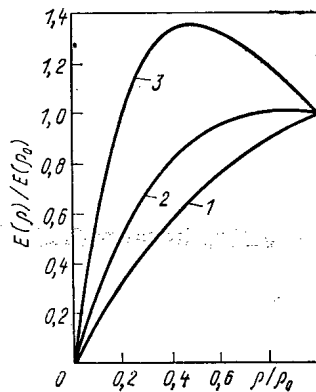Fig. 2   Fig. 3

Fig. 2.   X-ray energy flux density in air as a function
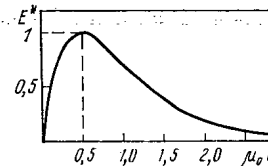of air density for $\mu(0)R$ equal to 1) 0.3; 2) 0.6; 3) 1.0.

Fig. 3.   Dependence of energy flux density of radiation
scattered in air on the normalized distance to the air
layer.

$$E_B(\Delta R) = Bx \exp\left[-2\mu(0)\,xR\right], \tag{4}$$

where $B = E_0 \dfrac{d\sigma}{d\Omega} \dfrac{ZN_A \Delta R \rho_0 (1-\cos\psi_0)}{MR^2}$; $\quad x = \rho\rho_0^{-1}$;

N_A is Avogadro's number, Z is the average atomic number of the scattering medium, and M is
the average atomic mass of the gases making up the air.

We normalize (4) to $E_B(z)$ for the initial conditions $[\mu_0 = \mu(0)$ or $\rho = \rho_0]$:

$$E_B^* = \frac{E_B(\rho \leqslant \rho_0)}{E_B(\rho = \rho_0)} = \frac{\rho}{\rho_0} \exp\left[2\mu(0)\,R\left(1 - \frac{\rho}{\rho_0}\right)\right]. \tag{5}$$

Figure 2 shows E_B^* as a function of ρ/ρ_0 calculated with Eq. (5) for several normalized
distances $\mu(0)R$. In this case the variation of $\mu(0)$ is related to the variation of the
initial energy E_0 of the photons.

Figure 2 shows that the larger the displacement of the gate along the time axis rela-
tive to the main pulse (the larger R), and the lower the energy E_0 (decrease of $\mu(0)$), the
greater the effect of the air density on the energy of the rays recorded in the gate. The
change of energy between 50 and 200 keV is affected less than the change of R. This property
can be used to construct devices which can not only measure air density more accurately, but
also more importantly, can measure the density of the scattering medium in a localized re-
gion.

To determine the value of x for which E_B is maximum, we set the derivative of Eq. (4)
with respect to x equal to zero. This gives $\mu_0 R = 0.5$ as the condition for a maximum.

Substituting this value into Eq. (2), we find the maximum value of the energy of the
backscattered x rays recorded in the gate by the detector. Normalizing Eq. (2) to this
maximum, we obtain

$$E^*(\mu_0 R) = \frac{E_B(\mu_0 R)}{E_{B\max}(\mu_0 R)} = 2\mu_0 R \exp\left[1 - 2\mu_0 R\right]. \tag{6}$$

If we take $\mu_0 R$ as a parameter, Eq. (6) is completely normalized, and is convenient
for practical applications since all quantities in it are dimensionless (Fig. 3).   The

857

energy of the radiation backscattered from a layer of thickness ΔR (air background in the gate) is maximum for $\mu_0 R = 0.5$ for all values of the energy and any position of the gate on the time axis ($t = 2R/c$). The increase in background for $\mu_0 R < 0.5$ is a result of the fact that the volume of the air layer for a fixed ΔR increases with increasing R (Fig. 1). With a further increase in R the absorption of the backscattered radiation in the near layers begins to matter. With an increase in the energy E_0 of the quanta their mean free path in the scattering medium increases, and consequently the maximum backscattering occurs from more distant layers of air.

Analysis of the results obtained shows that the energy E_B of γ rays backscattered from a layer of air (energy of the background of pulsed x-rays from air in the gate E_B) is determined not only by the energy E_0 of the primary radiation and the angle of collimation ψ_0, as for integral estimates [3], but also by the location of the gate t(R) on the time axis relative to the radiated pulse, i.e., by the position of the air layer in space from which the backscattered radiation is recorded by the detector in the gate.

LITERATURE CITED

1. L. Ya. Morgovskii and F. L. Gerchikov, "Time characteristics of a backscattered x-ray pulse close to the interface between two media," At. Énerg., 51, 185–187 (1981).
2. I. K. Zykov and S. V. Varyushchenko, Ionizing Radiations in Aeronautical and Space Technology [in Russian], Atomizdat, Moscow (1975), p. 128.
3. B. P. Bulatov and N. F. Andryushin, Backscattering of Gamma Radiation in Radiation Technology [in Russian], Atomizdat, Moscow (1971), p. 240.
4. F. L. Gerchikov and V. D. Kosarev, "A local approach to the determination of the coordinates of an interface," At. Énerg., 47, 57–58 (1979).
5. V. A. Klimanov, S. A. Konovalov, V. A. Kochanov, et al., Propagation of Ionizing Radiations in Air [in Russian], Atomizdat, Moscow (1979), p. 213.
6. R. Stephenson, Introduction to Nuclear Engineering, McGraw-Hill, New York (1954).

COMPARISON OF THE EXPERIMENTAL AND THEORETICAL VALUES OF THE EFFECTIVE
ATTENUATION FACTORS OF RADIATION IN MONODISPERSE ABSORBERS

V. M. Zhdanova, V. I. Kostenko,
I. V. Krivolutskaya, and G. K. Potrebenikov

UDC 539.122:541.182

The problem of calculating the effective attenuation factors of radiation (x-rays) and neutrons in disperse absorbers has been considered in [1-7] in connection with the investigation of the shielding properties of disperse materials, in order to take account of the structures of ores and powdered specimens in nuclear-physics methods of analysis in the development of α-absorption dispersion analysis.

Theoretical estimates of the effective attenuation factors for monodisperse absorbers with spherical particles of the disperse phase [1-5] can be verified experimentally.

The fundamental assumption in the calculation of the effective attenuation factor μ' is the one relating to the law of distribution p(k) of the number of particles k of the disperse phase that are intersected by a quantum (a neutron) as it passes through a plane layer of disperse absorber of thickness L. For a binomial distribution $p(k) = C_N^k p^k (1 - p)^{N-k}$, k = 0.1, ..., N, $N = LD^{-1}$, p = 1.5 V (D is the diameter of the particles, V is the volume fraction of the disperse phase), the following expression was obtained in [1]:

$$\mu' = \mu^H - \frac{1}{D} \ln \{1 - 1.5V [1 - K(\mu D)]\};$$

$$K(\mu D) = \frac{2}{\mu^2 D^2} [1 - (1 + \mu D) \exp(-\mu D)],$$

(1)

where $\mu = \mu^A - \mu^H$; μ^A and μ^H are the linear attenuation factors of the α-radiation in the materials of the disperse phase and the in the dispersion medium, respectively. When $N = 1.5LD^{-1}$, p = V [2], and

Specimens of Disperse Absorber

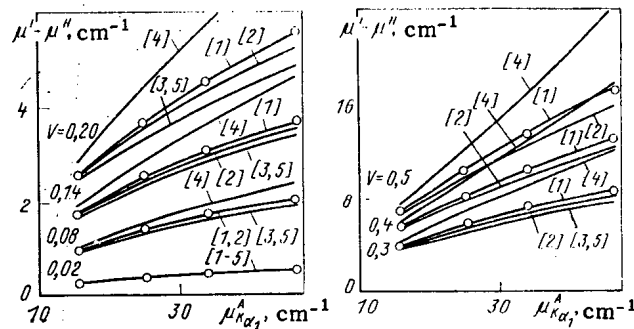| V	Av. CSS particle diameter, cm	Height of specimen, cm
0,020	0,0408	1,890
0,080	0,0408	0,900
0,140	0,0408	0,900
0,200	0,0408	0,490
0,300	0,0408	0,494
0,400	0,0323	0,311
0,500	0,0323	0,200

Fig. 1. Comparison of the experimental data (points) with the calculated data (curves); the square brackets indicate the source in the literature cited.

$$\mu' = \mu^H - \frac{1.5}{D} \ln \{1 - V [1 - K (\mu D)]\}. \tag{2}$$

For a Poisson distribution $[p(k) = \nu^k e^{-\nu} (k!)^{-1}$, $\nu = 1.5\ VL$, $k = 0.1, \ldots]$, we can find from (1) or (2), to within V when $V \ll 1$, the expression [3]

$$\mu' = \mu^H + \frac{1.5V}{D} [1 - K (\mu D)]. \tag{3}$$

Leman et al. [4] obtained an expression for the mass effective attenuation factor. The corresponding expression for a linear effective attenuation factor has the form

$$\mu' = \mu^H (1 - V) - \frac{\rho}{\rho_A D} \ln \left\{ 1 - 1.5V \frac{\rho_A}{\rho} [1 - K (\mu^A D)] \right\}, \tag{4}$$

where ρ_A and ρ are the density of the material of the disperse phase and the average density of the disperse absorber, respectively.

From expression (4), to within V when $V \ll 1$, we can obtain [5]:

$$\mu' = \mu^H (1 - V) + \frac{1.5V}{D} [1 - K (\mu^A D)]. \tag{5}$$

The values of the effective attenuation factors, calculated from the relations (1)-(5), may differ considerably and must be experimentally verified. In the present study we obtained experimental values of the effective linear attenuation factors of the characteristic x-ray radiation of the K-series of Ba, Pr, Sm, and Ho in specimens of disperse absorbers with spherical particles of the disperse phase (cast steel shot, CSS [8]) in a slightly absorbent dispersion medium (a mixture of starch and castor oil). The experimental apparatus was assembled on the basis of the "Mineral-3" roentgenoradiometric analyzer sensor in an arrangement with dual excitation: a ^{170}Tm radioisotope source excites the characteristic x-ray radiation of the intermediate target; this radiation is used to excite the characteristic x-ray radiation of the main target, which passes through the absorber being investigated and is recorded by a scintillation detector.

The theoretical estimates (1)-(5) correspond to an experiment with a broad monodirectional beam of radiation which must at the same time be sufficiently closely collimated to

859

reduce the contribution made to the recorded effect by the radiation scattered in the absorber. In order to satisfy both of these requirements, we placed the cylindrical absorber between two slit collimators and rotated it during the measurements. The operating regime of the apparatus was so chosen as to record all the lines of the K series. The diameter of the specimen of disperse absorber was 3.280 cm, the relative mean-square deviation of the distributions of the volume fraction of the particles of the disperse phase according to size was less than or equal to 16%, ρ_A = 7.3 g/cm^3, the density of the dispersion medium was 1.21 ± 0.03 g/cm^3. The remaining parameters are shown in Table 1.

The experimental values of the effective attenuation factors were determined as the average of three absorber specimens for each value of the volume fraction of the disperse phase. The experimental (mean square) error of these average values was less than or equal to 1.5%, and the experimental error of the linear attenuation factors was $\mu^H \leqslant 0.3\%$. The values of μ^H for the K series radiation of Ba, Pr, Sm, and Ho were 0.308, 0.277, 0.253, and 0.228 cm^{-1}, respectively.

Figure 1 shows a comparison of the experimental data with data calculated by formulas (1)-(5). In the calculation it was assumed that the slit collimators did not ensure monodirectionality of the radiation, and therefore we introduced a correction for the nonmonochromaticity of the characteristic radiation. The values of μ^A were calculated with due regard for the composition of the material of the CSS.

As can be seen from Fig. 1, the experimental data are in good agreement with those calculated by formula (1) for the absorbers investigated. For a small volume fraction of the disperse phase (V $\leqslant$ 0.08), the divergence between the experimental data and those calculated by formulas (3) and (5) does not exceed 3%.

LITERATURE CITED

1. A. G. Khislavskii, X-Ray Spectrum Rapid Methods of Analysis of Polymer Materials [in Russian], Khimiya, Leningrad (1976).
2. W. Berrus, Nucleonics, 16, No. 1, 91 (1958).
3. L. I. Shmonin, "Attenuation of a straight beam of gamma rays in a nonuniform layer of absorber," in: Physics [in Russian], Kazakhstan State Univ., Alma-Ata (1970), p. 71.
4. E. P. Leman, A. A. Tamrazyan, and V. A. Artsybashev, "Effective attenuation factors of gamma quanta in heterogeneous media with a binomial law of distribution of the nonuniformities," Dokl. Akad. Nauk Arm. SSR, 67, No. 1, 51-55 (1978).
5. V. A. Artsybashev and E. P. Leman, "Effective attenuation factors of photons in heterogeneous media," At. Énerg., 44, No. 1, 93-94 (1978).
6. Guidebook on Radiation Shielding for Engineers [in Russian], Vol. 2, Atomizdat, Moscow (1973).
7. G. K. Potrebenikov, "Investigation of a mathematical model of a disperse absorber, used in the α-absorption method of dispersion analysis," Defektoskopiya, No. 4, 74-79 (1982).
8. GOST 11964-66, Technical shot made of brass and steel [in Russian].

POSSIBILITY OF DETECTING SODIUM BOILING IN THE BN-600 REACTOR

BY MEANS OF NEUTRON NOISE

V. N. Efimov, S. N. Eshchenko,
A. A. Minakov, and Yu. I. Leshchenko

UDC 621.039.514

Early diagnosis of the presence of sodium in a fast-reactor fuel assembly is highly important as far as prevention of the spreading of this anomaly to the detriment of the entire core is concerned. One effective method of surveillance is analysis of the neutron-flux or reactivity noise.

Experience from a study of the sodium-boiling phenomenon in the BOR-60 reactor indicates that neutron-flux noise is basically the result of the emergence of a vapor phase accompanied by the formation of bubbles, their migration through the core and ensuing condensation, and also the periodic change of vapor phase (of oscillations), whereupon the boiling signal/noise ratio exceeds 20 dB [1].

The results given are typical of reactors with a small core, where the reactivity effects induced by sodium boiling in an individual assembly are fairly considerable. In a large reactor, neutron-physics monitoring and sodium-boiling diagnostics have their own peculiarities and complexities. In contrast to small-size reactors, the sign of the reactivity effect in the presence of local overheating and boiling can vary from section to section of the core. A considerable effect is produced on their control and safety rods.

For analyzing changes in the integral and local neutron fluxes in the presence of a fuel-assembly blockage, computer and experimental studies were carried out on BOR-60. As the basis for the computer scheme, we took a cylindrical two-dimensional model of the reactor in RZ geometry. Computing was carried out with the NF-6 programming complex, which had been developed for executing the two-dimensional neutron-physics studies [2]. For direct calculations we used a 26-group diffusion approximation, and for the assessment according to the perturbation theory we used the 6-group diffusion approximation (BNAB-78 library of constants).

In studies other than the change in reactivity we determined the response of the local neutron-flux detectors (NFD) made of rhodium. In BOR-60 the detectors were located in an experimental assembly at core-center level, and in the top section they were located at the level of the baseplate of the rotating sample. On the basis of the calculations for the
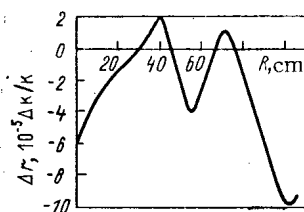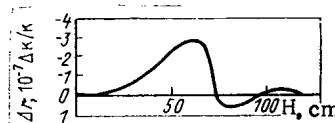

Fig. 1   Fig. 2

Fig. 1. Changes in reactivity in the case of the total destruction of a single fuel assembly as a function of the distance from the core center to the fuel assembly concerned.

Fig. 2. Changes in reactivity in the presence of a vapor bubble in a fuel assembly with a volume of 1 cm^3 as a function of the distance to the lowest extremity of the core.
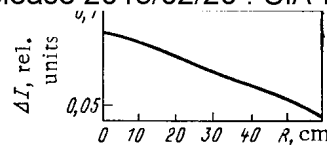
861

Fig. 3. Relative change in the signal from a rhodium NFD for the case of the complete destruction of a single fuel assembly in the sixth row: R) distance between the NFD and the axis of the anomalous fuel assembly.

change in neutron-flux density in the presence of local overheating we calculated the relative change in the signal DPZ

$$\frac{\Delta I}{I} = \sum_{i=1}^{26} \sigma_i \frac{\Delta \varphi_i}{\varphi_i} \delta_i,$$

where $\Delta I/I$ is the relative change in the signal NFD; $\Delta \varphi_i/\varphi_i$, relative change in the neutron flux of the ith group; δ_i, proportion of neutrons in the i-th group; and σ_i, (n, γ) capture cross section for ^{132}Rh and the neutrons of the i-th group.

In the case of the assessment of the change in reactivity and local changes in neutron flux, agreement between the calculated neutron spectrum and the actual one is of prime importance; in the calculations of the neutron spectra pertaining to 13 energetic groups, the maximum divergence from the experimental results was found to be 35% [3]. To assess the accuracy of the calculations on the BOR-60 we also performed experiments on the local change in temperature in the core. For a rise of 70°C in the temperature of the coolant in a single fuel assembly we obtained the following results (the first figure refers to the calculated value, the second to the experimental one): the change in reactivity, $\Delta k/k$ was $0.33 \cdot 10^{-5}$, $(0.4 \pm 0.05) \cdot 10^{-5}$, the relative change in signal NFD was 0.026, 0.015 ± 0.003 (at the core center), and was 0.078, 0.081 ± 0.016 (at the uppermost extremity of the core). The calculated results agree satisfactorily with the experimental ones. This makes it possible to use the method to assess the effects in the case of the destruction of a BN-600 fuel assembly.

As a result of the calculations that have been carried out, it is established that the effect of the total destruction of a single fuel assembly as a function of its location in the core varies in the range of $(-10-2) \cdot 10^{-5}$ $\Delta k/k$ (Fig. 1). From Fig. 1 it is evident that there exist regions where practically no void effect prevails. Calculations also show that there is a change of sign for the void effect with core height in certain fuel assemblies (Fig. 2) where, despite the small effect of the complete removal of sodium, considerable changes in reactivity are possible in the case of the partial destruction of an assembly.

One can use the data obtained to assess the characteristic neutron-flux noise when sodium boils. On the basis of the results of the experiments in the BOR-60 [1], we shall assume a boiling mechanism where the change in vapor volume amounts to ±20% of the volume of a single fuel assembly. Then the amplitude of the neutron-flux pulsation will be 0.04–0.72% of the nominal value, depending on where the boiling occurs.

Preliminary experimental studies on BN-600 neutron noise have made it possible to attain a standard deviation of 0.06% in the noise over the frequency range 0.1-10 Hz. A comparison of this value with the calculated one indicates that the amplitude of the noise due to boiling is lower than the background noise level in 20% of the fuel assemblies but higher than that in 80% of them. Hence it follows that the system for recording boiling by means of the usual neutron chamber will not be effective enough.

Among the calculations, we also determined the changes in the signals from NFD, which were placed above the endcaps of the BN-600 fuel assemblies, for the case of the complete destruction of a single assembly located in the sixth row of the core (Fig. 3). Analysis shows that, with the assumed boiling mechanism, in any fuel assembly the amplitude of the signal from a NFD installed on the bottom plate of rotating samples, due allowance having been made for their dynamic characteristics, is 0.25-0.51%. This means that, with one such probe, one can monitor coolant boiling at any point in the core. For recording weaker boiling, several local probes will be required.

As far as comprehensive basis for a monitoring system using NFD is concerned, it will be necessary to carry out further research work in rigs and on fast power reactors. However,

862

principle of devising effective sodium boiling noise diagnostic systems.

LITERATURE CITED

1. K. A. Aleksandrov. V. A. Afanas'ev, and V. N. Efimov, Basic Results of Research Work on the BOR-60 Reactor into the Diagnosis of Sodium Boiling in the Core. Atomic Science and Technology Questions. Physics and Technology of Nuclear Reactors Series [in Russian], No. 3 (25), (1982), pp. 44-49.
2. P. N. Alekseev and S. A. Bikineeva, Modules of the NF-6 Complex for the Multigroup Finite-Difference Calculation of the Flux Density and Worth of Neutrons in Nuclear Reactors in Two-Dimensional XY and RZ Geometry [in Russian], Preprint, NIIAR P-37 (445), Dimitrovgrad (1980).
3. N. R. Nigmatullin and G. I. Gadzhiev, The Change in Neutron Spectra in the BOR-60 Reactor [in Russian], Preprint, NIIAR P-15 (309), Dimitrovgrad (1977), p. 15.

EXPERIMENTAL DETERMINATION OF A UNIVERSAL EXCITATION FUNCTION

OF CHARACTERISTIC X RAYS BY A BEAM OF PROTONS IN A MASSIVE TARGET

V. F. Volkov, V. N. Sinitsyn,   UDC 535.33/34:539.183:539.184
and A. N. Eritenko

The registration intensity of characteristic x rays (CXR) excited by protons (ions) in a massive composite target can be written in the form [1, 2]

$$I_A^s = k \frac{N_A \rho}{A_A} c_A \omega_q^A P_\alpha R_s (E_{\max}) \sigma_A (E_{\max}) Q (\xi_0^A, a_{0,s}^A),$$ (1)

where k is the registration efficiency; N_A, Avogadro's number; ρ, density of the target; c_A and ω_q^A, concentration and fluorescent yield of the q-th level of element A of atomic mass A_A; P_α, probability of the radiation of a photon; $R_s(E_{\max})$, linear range of an ion in the target for an energy $E_{\max} \simeq 1.05 (m_p/m_e) E_q^A$, where m_p and m_e are respectively the proton and electron masses; E_q^A, binding energy of electrons of the q-th shell of element A; and $\sigma_A(E_{\max})$, ionization cross section of the q-th shell of element A for $E_{\max}$.

The universal function $Q(\xi_0^A, a_{0,s}^A)$ depends on two parameters, and has the form

$$Q (\xi_0^A, a_{0,s}^A) = \int_{\xi_q^A}^{\xi_0} \eta (\xi) \xi^{1/2} \exp \left\{ -a_{0,s}^A \left[1 - \left(\frac{\xi}{\xi_0^A} \right)^{3/2} \right] \right\} d\xi,$$ (2)

where

$$\xi_0 = E_0/E_{\max}; \quad a_{0,s}^A = \mu_{mi} R_{ms} = \sum_j c_i \frac{\sqrt{Z_j}}{A_j} \tilde{a}_j \Big/ \sum_j c_i \frac{\sqrt{Z_j}}{A_j};$$

$$\tilde{a}_j = \mu_{mi}^j R_{mj} (E_0); \quad \xi_q = E_q^A/E_{\max} = \text{const} (E_0 Z);$$

μ_{mi} and μ_{mi}^j are the mass absorption coefficients of the sample and element j for the radiation being analyzed, $\eta(\xi) = \sigma_A(\xi)/\sigma_A(E_{\max})$, $\sigma_A(\xi)$ is the ionization cross section, R_{ms} and R_{mj} are the mass ranges of a proton in the sample and in element j, and Z_j is the atomic number of the element.

The relative intensity of the CXR of element A has the form

$$\varkappa_A = \frac{I_A^s}{I_A^e} = \frac{c_A}{c_A^e} \frac{R_{ms}}{R_{me}} \frac{Q (\xi_0^A; a_{0,s}^A)}{Q (\xi_0^A; a_{0,e}^A)},$$ (3)

where I_α^e is the intensity of the CXR of element A from a standard sample with a concentration of the element equal to c_A^e. It was shown in [2] that $R_{ms}/R_{me} = \sum_j c_j^e \frac{\sqrt{Z_j}}{A_j} \Big/ \sum_k c_k \frac{\sqrt{Z_h}}{A_h}$, and therefore it follows from (3) that
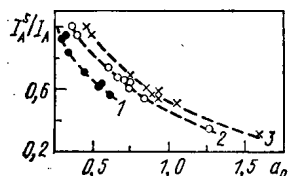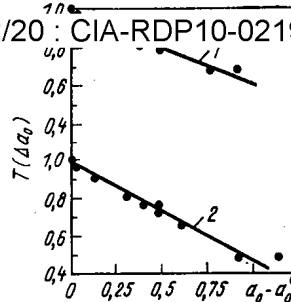
Fig. 1   Fig. 2

Fig. 1. Experimental dependence of the relative intensity $\varkappa_A$ of the K_α line on a_0 for proton energies of 1) 0.8; 2) 1; 3) 1.18 MeV.

Fig. 2. Experimental dependence of the universal excitation function on Δa_0 for proton energies of 1) 1.0; 2) 1.18 MeV.

$$T(\xi_0^A, a_{0,s}^A), a_{0,e}^A = \frac{Q(\xi_0^A, a_{0,s}^A)}{Q(\xi_0^A, a_{0,e}^A)} = \frac{\varkappa_A}{c_A} c_A^e \frac{\sum_k c_k \frac{\sqrt{Z_k}}{A_k}}{\sum_j c_j^e \frac{\sqrt{Z_j}}{A_j}}. \tag{4}$$

Numerical calculations showed that for $a \leqslant 2$, $Q(\xi_0, a_0) = Q(\xi_0, 0) \exp[-B(\xi_0) a_0]$, where $\beta = 0.325\xi_0^{0.085}$, and consequently

$$T(\xi_0^A, a_{0,s}^A, a_{0,e}^A) \simeq \exp[-\beta(\xi_0^A)(a_{0,s}^A - a_{0,e}^A)]. \tag{5}$$

For small values of the exponent of the exponential in Eq. (5)

$$T(\xi_0^A, \Delta a_0, e) \simeq 1 - \beta(\xi_0^A) \Delta a_0. \tag{6}$$

Thus, by measuring the relative intensity of lines for samples of known composition (for example, single-component samples can be used as standards) it is possible to determine the universal function $T(\xi_0, \Delta a_0)$. It is obviously necessary to choose the lines of elements for which there are no effects of selective excitation.

With this in mind we chose samples of Ni—Mn, Ni—Fe, and Ni—Fe—Mo alloys of various compositions. We recorded the K_α line of nickel. The CXR were excited by a beam of protons with energies of 0.795, 0.999, and 1.178 MeV. The experimental arrangement was described in [3]. $\varkappa_A$ depends exponentially on $a_{0,s}^A$ (Fig. 1).

Within the experimental and spectral processing errors the function $T(\xi_0^A, \Delta a_0)$ is linear, as follows from formula (6) (Fig. 2). It can be used to develop specific variants of the determination of the composition of samples, allowing for the influence of matrix effects on the intensity of the CSR.

LITERATURE CITED

1. V. F. Volkov, A. N. Eritenko, and Yu. A. Malykhin, "Dependence of the intensity of x-ray radiation excited by protons (ions) on ion energy and the target thickness," At. Energ., 48, 43-44 (1980).
2. V. F. Volkov and A. N. Eritenko, "Intensity of characteristic x rays excited by ions in massive composite samples," in: Proceedings of the Eleventh All-Union Conference on the Physics of the Interaction of Charged Particles with Crystals [in Russian], Moscow State Univ. (1982), pp. 509-512.
3. V. F. Volkov, V. N. Sinitsyn, and P. A. Lysenko, "Apparatus and methods for x-ray spectral analysis," in: Mashinostroenie, No. 24, (1980), pp. 186-189.

864

A DATA BANK ON THE METHODS OF MATERIALS TESTING IN REACTORS

N. V. Markina, A. V. Rudkevich,
and E. E. Lebedeva
UDC 621.039:62-30

The problems of reactor materiology require high quality in regard to methodological and metrological aspects of experiments for obtaining reliable information.

Owing to the specific aspects of reactor testing [1, 2], when a new method is worked out one must always use the experience obtained in testing either in the reactor itself or in shielded chambers for samples of previously irradiated materials.

The lack of information on the existing methodological developments often leads to the duplication of experiments or to additional experiments. In the case of reactor testing, such experiments are particularly expensive and require much time so that the efficiency of scientific research work is importantly affected. All these details have evoked interest in building an automatic data bank for the accumulation and systematization of information on reactor testing techniques, with their specific features properly taken into account.

Main Purpose of the Data Bank. Since the efficiency of methods to be developed should be increased and the metrological reliability of investigations should be improved [3], the various methods of reactor testing must be put into a systematic order. These problems are of prime importance as they mean obtaining representative, reliable experimental results suitable for comparison.

The development of an automatic data bank is the most promising way of storing the available information and of putting it into systematic order. The advantages of this means of information storage and processing have been repeatedly evaluated in the specialized literature [4, 5]. As far as the methods of reactor testing are concerned, a data bank makes it possible to generalize the experience gathered in research work, to develop a common representation of the totality of available testing methods, to establish the problems which have not yet been methodologically ensured, to provide a universal, formalized description of the methods employed, which description is required for developing criteria of comparison to develop criteria for the comparison of various methods, to make metrological inspections of methodical safeguards, and to optimize the number of new developments.

Besides that, the particular use of a data bank is associated with certain solutions adopted for necessary methodological developments on the basis of the previously reached development level.

When a databank is available, any researcher can make decisions on new methodological developments since he has at his disposal full information (in the form of descriptions, quantitative data, documentation lists, etc.) on the existing methods of studying interesting properties of materials, and, in addition, information on the evaluation of, firstly, the suitability of the methods for a particular proble and, secondly, the specific features of the methods (e.g., errors and ranges of parameters to be measured).

Data Model. The selection of a conceptual data model is the most important problem to be solved in the development of any new data processing system. The selection depends upon the classification of the subject field and the procedures required for access to the data. The known feature-dependent classification of reactor testing methods is based upon the arrangement of the subject field in accordance with the type of investigations (before the reactor, inside the reactor, behind the reactor), the goal of the work, and the properties to be studied or the conditions and the type of the irradiation [3]. This classification assumes symmetric access to the data, i.e., feasibility of a search (or determination): search for the methods of studying a particular property, designation of a particular group of methods with respect to their purpose, and methods corresponding to a particular class of tests and certain goals.

865

In addition, access to such details of methods as parameters to be measured, precision of the measurements, organization or developer of the method, reactor, etc. must be possible and a search for methods with given features must be feasible.

Fully symmetric access can be obtained only by a relation model of data. Though in the actual development of data banks, relation techniques have not yet been widely introduced [6], the corresponding theoretical problems have been solved rather well [7, 8]. Furthermore, in proportion to the development of the methodological safeguards, the bank must be expanded by introducing new characteristics. All these points have lead to the decision that a relation model must be adopted when the data bank is being built up.

In information systems the main points of the information are often divided into concepts, objects, properties of objects, characteristics of properties, etc. A hierarchy of concepts is constructed on the basis of such a subdivision. Thus, a measurement method can be related to characteristics (features) of the method, the precision of measurements, i.e., to characteristic features of the measuring technique, etc. However, in real problems it is usually not necessary to establish such a hierarchy [9]. Therefore a data base is built up on the basis of one terminal set the elements of which correspond to concepts, objects, properties in the subject field, and values of properties.

Problems of the Interaction with the Data Bank. The design of the bank provides for using a model of the subject field, represented in the data bank, by a final user who is not a specialist in the field of information processing.

The data bank is designed for a final user who must only indicate what to do without laying down conditions how to do it. Thus, the means of the interaction with the data bank do not involve procedures. One of the most promising modes of interaction with the data bank is based on a dialogue in a limited natural language. But such a dialogue is hard to achieve and requires large computational capacities. Furthermore, for the user of a data bank a response in the traditional form of tables and graphs is fully acceptable and often even more suitable. Therefore a formalized language based on calculus in terms of relations is used in a data bank.

The basic idea of the proposed approach to the communication with the data bank is associated with time-sharing in the inputting of questions and their description and also with the development of specialized nonprocedural languages for describing the question and the form of the instructions for the bank. The dialogue is designed for two categories of users in material research: a subscriber submitting questions and an instructing party inputting changes of the data or additions to them. The subscriber works with a more or less specific dialogue which can be started by the computer and uses previously determined types of questions formulated as a system of predicates containing parameters. During the dialogue, the subscriber inputs the parameter values whereupon the values of the variables are searched and the answer to a question is outputted. The instructing party inputs and corrects data by using previously prepared instruction patterns. In the course of the dialogue, the computer inquires for parameter values in accordance with the scheme given by the relation to be processed.

This interaction scheme provides for an efficient replenishing of the model with new information without need for studying special problems of programming and information theory, an operational search for information, operational redesigning of the model of the subject field (inclusion of new relations, removal and correction of old relations), operational changes in the vocabulary of the model, and the possibility of converting information represented by the model for the evaluation of this information and its generalization.

The data bank design described was put into practice in a BÉSM-6 computer. At the present time the data bank contains information on about 300 reactor testing methods developed. The library of inquiries includes about 20 descriptions. The preparation and inputting of one new description requires 5-20 min. The time of an answer to an inquiry depends upon the complexity of it and the load on the computer and varies between 30 sec and 3-4 min.

This data bank can be used for tests of materials in reactors and for research on irradiated materials housed in shielding chambers.

866

LITERATURE CITED

1. V. A. Tsykanov and B. V. Samsonov, The Technique of Irradiating Materials in Reactors with a High Neutron Flux [in Russian], Atomizdat, Moscow (1973).
2. Collections of Reports of the All-Union School on Research Techniques in Reactors [in Russian], Dimitrovgrad (1978).
3. V. A. Kuprienko, N. V. Markina, and V. A. Tsykanov, "State and development of the work on the improvement of radiation testing," At. Énerg., 55, No. 4, 208 (1983).
4. K. Date, Introduction to Data Base Systems [Russian translation], Nauka, Moscow (1980).
5. L. V. Kokoreva and I. I. Malashinin, The Planning of Data Banks [in Russian], Nauka, Moscow (1984).
6. B. V. Kristal'nyi, G. N. Radkovskii, A. A. Raskina, et al., "Some Problems of the Facto-graphic Search (Specific Features, State, Tendencies)," Vopr. Inf. Teor. Praktiki, No. 46, 5 (1983).
7. V. P. Dribas, Relation Models without Data [in Russian], Beloruss. State Univ., Minsk (1982).
8. E. Codd, ACM Trans. Database Systems, 4, No. 4, 397 (1979).
9. V. S. Lozovskii, "Extension data base on the basis of semantic nets," Izv. Akad. Nauk SSR, Ser. Tekh. Kibern., No. 5, 23 (1982).

INFLUENCE OF THE POSITION OF THE GROUP OF ELEMENTS OF THE CONTROLLING

AND SHIELDING SYSTEM UPON THE INTEGRAL NEUTRON FLUX THROUGH THE SIDE

SURFACE OF THE JACKET OF THE VVÉR-440 (WATER—WATER POWER) REACTOR

L. N. Bogachek, K. A. Gazaryan,   UDC 621.039.512.44
A. M. Luzhnov, V. V. Lysenko,
A. S. Makhon'kov, V. V. Morozov,
A. I. Musorin, V. I. Pavlov,
E. S. Saakov, V. D. Simonov,
and S. G. Tsypin

Measuring systems which are based on detectors mounted outside a reactor are widely employed for determining integral and differential characteristics of the energy distribution in the core of a nuclear reactor [1].

An output meter was mounted on the first block of the Armenian Atomic Power Station [2]. The sensor of the output meter is located under the reactor jacket near the geometrical axis of the reactor (see Fig. 1). The goal of the present work is a quantitative evaluation of the influence of the elements of the controlling and shielding system of the boron concentration in the coolant on the readings of the output meter.

The experimental data listed in Table 1 were obtained in the first half of the second operating period of the first block of the Armenian Atomic Power Station. The measurements were made at various reactor output values which were determined from the thermal balance

TABLE 1. Results of the Experiment

Position (cm) of the sixth group of ele-ments	Concn. (g/kg) of boric acid in the cool-ant	Thermal output (MW) of the re-actor	Readings (rel. units) of the out-put meter referred to the thermal
60	5,6	500	1,000
85	2,5	1188	0,993
143	6,4	459	0,947
176	3,0	1195	0,909
230	3,4	1199	0,876
248	6,8	477	0,849
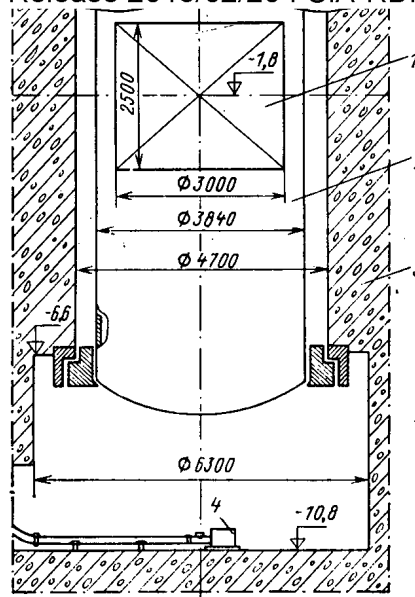
Fig. 1. Position of the output meter: 1) core; 2) reactor;
3) shield; 4) sensor of output measurements.
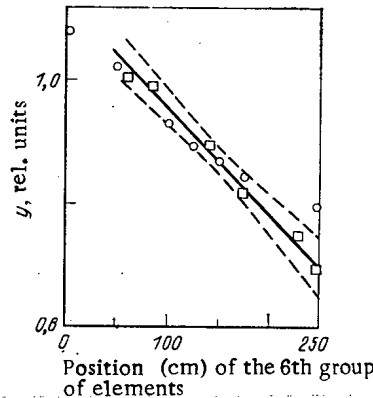

Position (cm) of the 6th group
of elements

Fig. 2. Comparison of the experimental results with
the calculated results: □) readings of the output
meter referred to the thermal output of the reactor;
—) regression line of the readings of the output
meter referred to the thermal output of the reactor
in dependence upon the position H_6 of the sixth
group of elements of the controlling and shielding
system with y = 0.9278 — 0.00083 (H_6 — 157.2); ○) cal-
culated integral neutron flux through the side surface
of the reactor (0.95 confidence level).

[3]. An analysis of the resulting data has shown that the ratio of the counting rate of the
output meter to the thermal power of the reactor does not depend (within the error limits of
the experiment) upon the boron concentration of the coolant but changes noticeably when the
group of elements of the controlling and shielding system are rearranged (see Fig. 2).

The radiation field in the zone of the sensor of the output meter is generated mainly
by neutrons which have passed through the side surface of the reactor into the gap between
the jacket and the concrete shield (see Fig. 1) and which have experienced a few scattering
deflections. The neutrons which have left the core in downward direction are suppressed by
a 3-m water layer [2]. Taking into account this detail and the experimental results, it was
assumed that a particular thermal rating, a change in the position of the group of elements
of the controlling and shielding system will substantially influence the integral neutron
flux through the side surface of the reactor jacket. This effect has been theoretically
predicted a long time ago [4] but quantitative estimates have not been made for a water—

868

water power reactor. In the case under consideration, when the position of the group of elements of the controlling and shielding system was changed from 60 to 250 cm (the elements were completely pulled out), the counting rate normalized to the output and, hence, the integral neutron flux through the side surface decreased by 15%.

Calculations have confirmed that such an important effect is possible. The BIPR-5 program [5] was used to calculate the energy distribution corresponding to various positions of the group of elements of the controlling and shielding system at nominal parameters of the coolant and the reactor output of the first block of the Armenian Atomic Power Station. Thereafter, ray analysis was used to calculate for each energy distribution the integral neutron flux through the external side surface of the reactor jacket, the side surface being delimited by the height of the core. The relaxation length within the core was 10.7 cm and 8 cm outside the core (see Fig. 2).

Thus, it was shown by experiments and calculations that a change in the position of the group of the elements of the controlling and shielding system from half immersion to total pull-out (at an unchanged reactor output) reduces the integral neutron flux through the reactor side surface by 10-15%. A change in the concentration of boric acid in the coolant from 2.5 to 6.8 g/kg only insignificantly affected the integral flux.

The authors thank V. A. Voznesenskii and A. N. Kamyshan for useful discussions of the results and for their support of the present work.

LITERATURE CITED

1. A. M. Luzhnov, V. V. Morozov, N. S. Orekhova, and S. G. Tsypin, "Use of detectors mounted outside the reactor for controlling the output level and the energy distribution," At. Tekh. Rubezhom, No. 8, 19 (1984).
2. L. N. Bogachek, K. A. Gazaryan, V. V. Lyenko, et al., "Correlation-dispersion method of measuring the output of a water—water power reactor," At. Énerg., 50, No. 6, 420 (1981).
3. F. Ya. Ovchinnikov, L. I. Golubev, V. D. Dobrynin, et al., Exploitation Conditions of Nuclear Water—Water Power Reactors [in Russian], Atomizdat, Moscow (1979).
4. S. Glasstone and M. Edlund, Principles of the Theory of Nuclear Reactors [Russian translation], IL, Moscow (1954).
5. D. M. Petrunin, E. D. Belyaeva, and I. L. Kireeva, BIPR-5 — a Program for Calculating Three-Dimensional Fields of Energy Release and Fuel Burnout in Single-Group Diffusion Approximation for Nuclear Water—Water Power Reactors [in Russian], Preprint of the Inst. of Atomic Energy, No. 2518, Moscow (1975).

MODEL OF CRATER FORMATION UNDER ION BOMBARDMENT

V. P. Zhukov and A. V. Demidov   UDC 621.039.531

The formation of craters on the surface of materials irradiated by high-energy ions is attracting a great deal of attention; its mechanism, however, remains unclear. The dimensions of the craters formed depend in a complicated manner on the parameters of irradiation. For example, when the surface of Au was bombarded with 125-keV Bi^+ ions the average crater diameter was equal to $\sim$4.6 nm, while when a Ge surface was bombarded by 20- and 40-keV Te^+ and Te_2^+ ions the crater diameters reached 10-20 and 20-40 nm, respectively [1].

It is difficult to explain such large crater sizes on the basis of the traditional model of a cascade of atomic collisions, since its dimensions ($\sim$5 nm) are much smaller than the dimensions of the craters [1]. A more accurate model was given in [2], where the solid is approximated by a continuous medium and the concept of a shock wave is used, though the maximum crater diameter predicted by this model is still ten times smaller than the observed diameter [1]. Moreover, the mechanism assumed for the ejection of matter is doubtful from the viewpoint of the physics of shock waves [3]. Larger crater dimensions are predicted by the model in [4], where the problem under study is likened to the well-known problem of the impact of a meteorite against the surface of a planet [3]. This approach, however, is valid only for an extremely small penetration depth of the ion, when the probability of the formation of a crater reaches 100%, in contrast to the probability observed in practice, which is equal to $\sim$1%.

A more accurate analysis [5] of the peak displacement in the approximation of a continuous medium showed that the evolution of this peak can be approximated by the evolution of a spherical explosion wave with a central cavern and an outgoing plastic shock wave. In the light of the correspondence established between the peak displacement and the microexplosion it is appropriate to analyze crater formation as being the result of the development of a subsurface displacement peak on the basis of the physics of subsurface (underground) explosions [6].

The mechanics of an underground explosion that leads to the formation of a crater is, unfortunately, quite complicated, and the analysis can be carried out only with significant simplifications. When the charge is placed at a moderate depht, the plastic shock wave emerges to the surface, causing the formation of a dome and a reflected rarefaction wave, whose interaction with the shock wave can cause spallation of part of the material on the surface. As soon as the rarefaction wave reaches the cavern, a higher velocity is imparted to the material lying above it and accelerated growth of the cavern begins in the direction toward the surface. When the energy of the explosion occurring at a moderate depth is high enough, the dome formed breaks apart (fragments) and is ejected to the outside in the form of fragments, which leads to the formation of a crater whose diamter can be several times larger than the characteristic diameter of the cavern formed by an explosion in an unbounded medium. When the explosion occurs at a small depth, the connecting strip separating the cavern from the surface can be ejected even before the onset of the interaction between the reflected rarefaction wave and the cavern, and then the crater diameter is approximately equal to the cavern diameter. Thus the existence of these two mechanisms of crater formation gives rise to the existence of some optimal depth for placing the charge at which the dimensions of the crater are maximum; this is confirmed by the experimental data.

These ideas are useful in evaluating the size of the crater formed when the material is dispersed by the bombarding ions. Taking into account the hardness of the medium, the following semiempirical formula relating the mass of the charge to the dimensions of the crater is obtained [6]: $q = Kh^3[A + B(r/h)^3]$, where q is the mass of the charge; h is the depth of the charge; r is the radius of the visible crater; $K \approx 2$ kg/m^3; A = 0.4 and B = 0.6 are empirical coefficients, which are virtually independent of the properties of the medium. Taking into account the fact that a 1-kg charge is equivalent to an energy of $3 \cdot 10^{22}$ keV, we obtain the following relation for estimating the diameter of the crater: $d = 2[(3 \cdot 10^{-23} E/K - Ah^3)/B]^{1/3}$.

Under bombardment by ions giving rise to peak displacement at a depth of ∿10 nm, when the energy of the primary knocked-out atom is E = 100 keV, the diameter of the crater will be equal to 100 nm, which is in agreement with the experimental data for Ge. In the case of Au the diameter of the crater is quite close to the computed diameter of the cavern (∿5 nm [5]) and is apparently formed by the subsurface peak displacement. If, on the other hand, this peak displacement is located at a depth ≤ 20 nm (which is comparable to the diameter of the shock wave at the moment that plastic flow ceases [5]), then only the elastic wave emerges onto the surface and the crater is not formed. We note that a crater may also not be formed in the case of a nearly surface cascade of displacements, when the conditions for the formation of a shock wave are not met. When the crater is approximated by a hemisphere with a diameter d, the dispersal of the material is proportional to E [2, 4].

In spite of the fact that the formula used is much too simplified, since it does not lead to the correct limiting transitions accompanying the formation of the peak displacement at small and large depths, the estimates obtained indicate that the model of a subsurface explosion could be useful in giving a quantitative description of the process of crater formation.

LITERATURE CITED

1. D. Thompson, "High density cascade effects," Radiat. Eff., 56, 105-150 (1981).
2. Y. Kitazoe and N. Hiraoka, "Hydrodynamical analysis of nonlinear sputtering yields," Surf. Sci., 111, 381-394 (1981).
3. Ya. B. Zel'dovich and Yu. V. Raizer, Physics of Shock Waves and High-Temperature Hydrodynamic Phenomena, Academic Press.
4. G. Carter, "A semiquantitative approach to ion impact induced shock processes in solids," Radiat. Eff. Lett., 50, 105-109 (1980).
5. V. P. Zhukov and A. V. Demidov, "Calculation of displacement peaks in the continuous-medium approximation," At. Energ., 59, No. 1, 29-33 (1985).
6. The Physics of Explosions [in Russian], Nauka, Moscow (1975).

ANALYSIS OF THE EFFECTIVENESS OF MONITORING OF THE ENERGY LIBERATION
FIELD IN REACTORS BASED ON CONDITIONAL DISTRIBUTION LAWS

V. A. Vlasov, P. I. Popov,
and V. V. Postnikov

The energy-liberation field $\xi(r)$ in reactors is often controlled with the use of the reconstructed (estimated) values $\hat{\xi}_i$ of a random field $\xi(r)$ at the points $r_i (i = 1, 2, \ldots, m$ [1, 2]; the values of $\xi(r)$ are evaluated according to the indications $\eta_1, \ldots, \eta_n$ of sensors used for discrete monitoring with the help of a computer [2]. The efficiency of operational control of the energy-liberation field is analyzed below as a function of the accuracy with which it is monitored, taking into account the characteristics of the thermotechnical reliability of the active zone of the reactor using normally distributed random quantities. The normal distribution law is used in the practice of ensuring the thermotechnical reliability of the active zone of reactors [2]. It is recommended that the probability $R(t)$ that at each time t the true values $\xi_i = \xi(r_i)$ of the field do not exceed their critical values $\xi_{cr.i}$ be used as its quantitative characteristic [3]. The inequality $\xi_i < \xi_{cr.i}$ is equivalent to the inequality $v_i > 0$, where $v_i = \xi_{cr.i} - \xi_i$; in addition, $\xi_{cr.i}$ can also be a random quantity, evaluated with some error. In what follows, we shall study v with the coordinates $V_i (i = 1, 2, \ldots, m)$. In reality, v is never known because of the errors in the estimation of ξ_{cri}, ξ_i.

Assume that at time t the density distributions $p_v(x_1, \ldots, x_m, \beta_1, \ldots, \beta_l)$ and $p_\xi(y_1, \ldots, y_m, \beta_1, \ldots, \beta_l)$ of the vectors v and ξ with the coordinates $\xi_i (i = 1, 2, \ldots, m)$, where $\beta_1, \ldots, \beta_l$ have the meaning of control parameters (for example, the positions of the regulating organs), are known. The values of $\beta_1, \ldots, \beta_l$ can be chosen starting from the

871

optimization of a given functional J, depending on $p_\xi(y_1, \ldots, y_m, \beta_1, \ldots, \beta_l)$ and characterizing the goal of the control action, under the condition that $R(t) \geqslant R_{adm}$, where R_{adm} is the admissible value of the level of thermotechnical reliability. The functional J can be taken, for example, as the average value J_0 of the total power of the reactor.

At each time t the distributions $p_\xi(y_1, \ldots, y_m, \beta_1, \ldots, \beta_l)$ and $p_V(x_1, \ldots, x_m, \beta_1, \ldots, \beta_l)$, are refined with the help of the observed vector η with the coordinates $\eta_1, \ldots, \eta_n$, i.e., these distributions are conditional. Therefore the conditional value t of the level of thermotechnical reliability of $J_y(t)$ and the conditional value of $R_y(t)$ of the functional J can be calculated at each time t. The problem of controlling the field lies in selecting the values of the control parameters at each t such that $J_y(t)$ assumes a maximum value, the condition $R_y(t) \geqslant R_{adm}$ is satisfied, and other restrictions on $\beta_1, \ldots, \beta_l$ of a structural or regulating character also hold. Thus the field is indirectly controlled from the vector ob observations η correlated with it.

Variation of the control parameters involves a change in the observed values $\eta_1, \ldots, \eta_n$, which affects $R_y(t)$, $J_y(t)$. Therefore, in order to make the correct choice of control parameters the dependences of the observed values on $\beta_1, \ldots, \beta_l$, obtained on the basis of modeling of the physical properties of the reactor, must be known. Finding the conditional distribution laws $p_\xi(y_1, \ldots, y_m, \beta_1, \ldots, \beta_l)$ $p_{Vvy}(x_1, \ldots, x_m, \beta_1, \ldots, \beta_l)$ in the general case is a laborious computational operation. For a normal joint distribution law of all random quantities studied, the conditional distribution laws for V, ξ are also normal [4]. The optimal linear estimates of the coordinates of the vectors V and ξ summarize all information about these laws incorporated in η [5]. The optimal linear estimates of the coordinates of the vectors V and ξ are conditional mathematical expectations of these coordinates, and the conditional covariational matrices of the vectors are independent of η [4]. Thus for the normal distribution law the most accurate monitoring of the field is an intermediate operation for finding the conditional distribution laws of the vectors V and ξ and correspondingly $R_y(t)$ and $J_y(t)$. The statistical interpolation, used for reconstructing the energy-liberation field [2], is equivalent to searching for the conditional mathematical expectation of random quantities.

Finding the optimal values of the control parameters, even under the conditions of a normal distribution law is a laborious operation, because of the large dimensions of V and . We shall therefore begin the analysis of the control efficiency with the analysis of the admissible value of the observed energy liberation in one fuel channel of the reactor.

Let the control parameter at the beginning of the analysis be the mathematical expectation μ of energy liberation ξ_T in the channel; in addition, ξ_T and its critical value $\xi_{T \cdot cr}$, are monitored with random errors ε_T and ε_{cr}, respectively, so that the observed values are equal to $\eta_T = \xi_T + \varepsilon_T$, $\eta_{T \cdot cr} = \xi_{T \cdot cr} + \varepsilon_{cr}$. The observed values η_T, $\eta_{T \cdot cr}$ are assumed to be arbitrary unbiased estimates of ξ_T, $\xi_{T \cdot cr}$, obtained as a function of the vector of measurements η. Under the assumption that the vector θ with the coordinates ξ_T, $\xi_{T \cdot cr}$, ε_T, ε_{cr} is distributed according to the normal law with a known covariation matrix $\bar{K}$ and known mathematical expectations of the coordinates $M[\xi_T] = \mu$, $M[\xi_{T \cdot cr}] = \mu_{cr}$, $M[\varepsilon_T] = M[\varepsilon_{cr}] = 0$, the vector θ with the coordinates η_T, $\eta_{T \cdot cr}$, $\nu_T = \xi_{T \cdot cr} - \xi_T$, linearly related to θ_T, also has a normal distribution law with known mathematical expectations $M[\eta_T] = \mu$, $M[\eta_{T \cdot cr}] = \mu_{cr}$, $M[\nu_T] = \mu_{cr} - \mu$ and a known covariation matrix K, which can be calculated from the matrix $\tilde{K}$.

The conditional distribution law ν_T is the normal distribution with mathematical expectation μ_{vy} and mean-square deviation σ_{vy}, so that the level of thermotechnical reliability for the channel is equal to

$$R_y^T = \Phi(\mu_{vy}/\sigma_{vy}), \tag{1}$$

where $\Phi(u)$ is the distribution function of the normal distribution of a random quantity, having unit variance and zero mathematical expectation. The unfolded form of the analytical dependence of μ_{vy}, σ_{vy} on the parameters of the distribution law of the vector θ is presented, for example, in [6]:

$$\sigma_{vy}^2 = \sigma_v^2 \frac{1 - \rho_1^2 - \rho_2^2 - \rho_3^2 + 2\rho_1\rho_2\rho_3}{1 - \rho_3^2}; \tag{2}$$

$$\mu_{vy} = \mu_{cr} - \mu + \lambda_{cr}(\eta_{T \cdot cr} - \mu_{cr} + \lambda_T(\eta_T - \mu)),$$

where

872

$$\rho_1 = \rho\,[\nu_T,\ \eta_{T.cr}];\quad \rho_2 = \rho\,[\nu_T,\ \eta_T];\quad \rho_3 = \rho\,[\eta_{T.cr},\eta_T];$$

$$\rho[\cdot,\cdot]$$

is the symbol for the correlation coefficient; σ_ν, σ_{cr}, σ_T are the mean-square deviations of the random quantities ν_T, $\eta_{T \cdot cr}$, η_T.

The quantity Δ_y, by which $\mu_{\nu y}$ must be changed in order for the equality $R_y^T = R_{adm}$, to hold, is calculated according to the relation (1) from the equation

$$R_{adm} = \Phi[(\mu_{\nu y} + \Delta_y)/\sigma'_{\nu y}], \tag{3}$$

where $\sigma'_{\nu y}$ takes into account the possible change in the parameters of the distribution law of the vector θ accompanying a change in the control parameter μ.

Under the assumption that when μ varies the remaining parameters of the distribution law of θ remain unchanged and the quantity $\overset{\bullet}{\eta}_T = \eta_T - \mu$ remains constant, from the expression (2) we find that the change $\Delta\mu$ in the parameter μ, for which the condition (3) holds, is equal to

$$\Delta\mu = \mu_{cr} - \mu - \varkappa\sigma_{\nu y} + \lambda_{cr}\,(\eta_{T \cdot cr} - \mu_{cr}) + \lambda_T\,(\eta_T - \mu), \tag{4}$$

where $\varkappa = \Phi^{-1}(R_{adm})$, and $\Phi^{-1}(u)$ is the function inverse to $\Phi(u)$.

The constancy of η_T is a model of the dependence of the observed value of η_T on the control parameter μ, since $\eta_T = \mu + \eta_T$.

Using this model enables the calculation of the admissible observed value

$$\eta_{cr}^T = \mu_{cr} - \varkappa\sigma_{\nu y} + \lambda_{cr}\,(\eta_{T \cdot cr} - \mu_{cr}) + (1 + \lambda_T)\,\overset{\bullet}{\eta}_T.$$

Thus the admissible observed value of energy liberation depends on the observed values $\eta_{T \cdot cr}$, η_T.

Control consists of selecting a μ at time t such that the observed value of energy liberation would be equal to η_{adm}^T. At the same time, as an analysis using a formula similar to (2) shows, the equality $M[\xi_T] = \mu_{cr} - \varkappa\sigma_{\nu y}$ will be achieved. Thus the more accurately ν_T, is monitored, the higher is the average value of energy liberation achieved with the use of the observed values for generating the control actions. When the conditional mathematical expectation of the quantity ν_T is used as the observed value, the admissible (lowest) value is constant and equal to $\varkappa\sigma_{\nu y}$.

In practice the number l of control parameters is less than the number m of fuel channels. For this reason, in the general case, it is impossible to satisfy the equality $\eta_T = \eta_{adm}^T$ for all channels simultaneously, and for an optimum choice $\beta_1, \ldots, \beta_l$ there exists an admissible value $\eta_{admi} < \eta_{admi}^T$ for each channel with which the maximum of J_0 is attained. If it is impossible to calculate the optimal values of the control parameters, then they can be determined by approximate methods, in particular, from operator experience. An approximate determination of $\beta_1, \ldots, \beta_l$ produces an additional lowering of the energy liberation in each fuel channel by δ_i. The sum $\delta_0 = \sum\limits_{i=1}^{m}\delta_i$ determines the total power of the reactor and

serves as a characteristic of the method for selecting the control parameters (in particular, operator experience), and lowering the mean-square monitoring error ν_i by $\Delta\sigma_{\nu y}$ enables increasing J_0 by a value close to

$$\Delta J_0 = m\varkappa\Delta\sigma_{\nu y}.$$

The critical values of the coordinates V are known exactly (they are equal to zero), since the vector Ψ with the coordinates $\Psi_i = \eta_{admi}^T - \eta_{admi}' - \delta_i$ is actually the vector of regulation errors [2]. The exact value of ΔJ_0 can be obtained only by taking into account the dependence of the errors in monitoring and regulation of V.

There is one other factor determining the desirability of using the procedure for reconstructing the energy-liberation field. The parameters of the distribution law ξ_T, for example, the mathematical expectation μ, may be unknown, but can be estimated from the collection of observed values $\eta_i(i = 1, 2, \ldots, n)$ [2]. Focusing on the indications in each fuel channel, it is possible to use the estimate $\hat{\mu}_{yi} = \eta_i$ of the conditional mathematical expectation of μ_{yi}; in addition the accuracy of $\hat{\mu}_{yi}$ is characterized by the quantity $\sigma_{\delta y}^2 = M[(\eta_T - \mu_y)^2]$. For example, for unknown ε_T, we have ξ_T, where $\sigma_{\delta y}^2 = \sigma_\xi^4/\sigma_\xi^2 + \sigma_\varepsilon^2$, where σ_ξ^2 and

873

ensuring the thermophysical reliability of the active zone of the reactor. The use of the entire collection of observed values substantially increases the accuracy of estimates of the unknown parameters of the distribution laws and correspondingly the accuracy of the estimation of R_y.

LITERATURE CITED

1. I. Ya. Emel'yanov, A. I. Efanov, and L. V. Konstantinov, Scientific—Technical Foundations of Nuclear-Reactor Control [in Russian], Énergoizdat, Moscow (1981).
2. E. V. Filipchuk, P. T. Potapenko, and V. V. Postnikov, Control of the Neutron Field of a Nuclear Reactor [in Russian], Énergoizdt, Moscow (1981).
3. A. O. Klemin, L. N. Polyanin, and M. M. Strigulin, Thermohydraulic Calculation and Thermotechnical Reliability of Nuclear Reactors [in Russian], Atomizdat, Moscow (1980).
4. T. Anderson, Introduction to Multidimensional Statistical Analysis [Russian translation], Fizmatgiz, Moscow (1963).
5. V. A. Vlasov and P. I. Popov, "Forecasting of the values of random quantities and estimation of unknown parameters," in: Automation of the Control of Technological Processes [in Russian], No. 2, Atomizdat, Moscow (1977), pp. 69–72.
6. V. A. Vlasov and P. I. Popov, "Peculiarities of estimation from dependent random values," ibid., pp. 72–76.

MONTE CARLO CALCULATION OF THE FIELD GRADIENT OF γ RAYS

M. P. Panin

The radiation field behind a shield of complex geometric form is distinguished by considerable spatial inhomogeneity. In connection with this, it is of interest, in investigating the field, to determine not only the functionals of the field but also their derivatives. In the present work, an algorithm is proposed for the direct calculation of the gradients of the photon flux density, the energy flux, and the photon radiation dose by the Monte Carlo method.

To estimate the gradient of the γ-ray flux density at the point of detection r^*, use is made of the well-known local estimate [1] for a point detector $F_i(r_i, r^*, \mu)$ depending on the point of collision r_i and the corresponding cosine of the scattering angle μ. If the flux density Φ is the mathematical expectation of this estimate, its gradient will be

$$\nabla\Phi = M \nabla F_i. \tag{1}$$

Differentiating the local estimate F_i with respect to the spatial variable r^*, an explicit expression for ∇F_i in terms of the differential scattering cross section $\sigma_s(\mu)$ and the optical thickness τ between the points r_i and r^* is obtained

$$\nabla F_i = F_i \left[-2\frac{r^* - r_i}{|r^* - r_i|^2} + \frac{\nabla \sigma_s(\mu)}{\sigma_s(\mu)} - \nabla\tau \right]. \tag{2}$$

For the second term in this formula, it is found that

$$\frac{\nabla \sigma_s(\mu)}{\sigma_s(\mu)} = \frac{\nabla\mu}{\sigma_s(\mu)}\frac{d\sigma_s}{d\mu}, \quad \nabla\mu = \frac{\Omega - \mu\omega}{|r^* - r_i|}, \tag{3}$$

where Ω is the direction of photon motion before collision; ω is the direction to the detector r^* from point r_i. Using the Compton model of scattering, it may be shown that

$$\frac{1}{\sigma_s}\frac{d\sigma_s}{d\mu} = \frac{3E'^2 + E^2 + 2EE'(\mu - 1) + 2\mu E'}{E' + E^2(1 - \mu) + E\mu^2}. \tag{4}$$

Here and below, E and E' are the photon energies before and after scattering, expressed in units of m_0c^2.
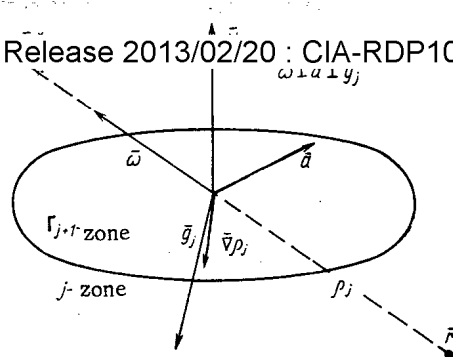
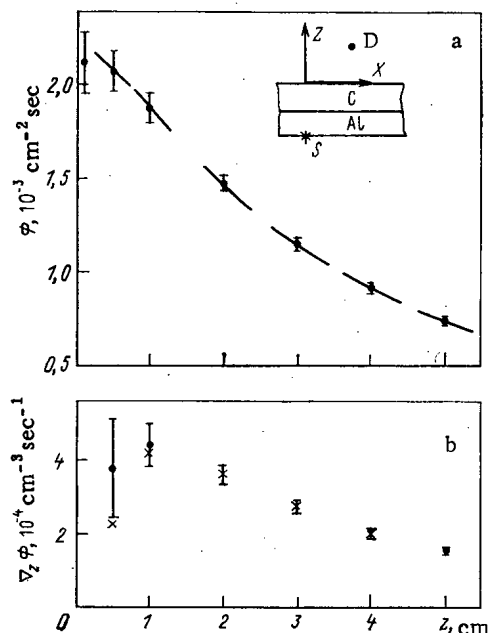Fig. 1. Diagram for determining the direction of
the vector $\nabla \rho_j$.

Fig. 2. Dependence of the photon flux density (a)
and z projection of the gradient of the photon flux
density (b) on the distance to the barrier surface.
Displacement of the detector D along the X axis by
4 cm; source energy S = 0.1 MeV. The filled circles
correspond to results of calculation by the Monte
Carlo method and the crosses to estimates of the
derivative by the quadratic approximation; the line
segments show the value of $\nabla_z \Phi$.

Now consider the calculation of $\nabla \tau$. Suppose that the optical thickness is formed by
the sum of n zones, each of which has the length l_j and the cross section σ_j^i for energy E'.
Then

$$\nabla \tau = \sum_{j=1}^{n} \sigma_j' \nabla l_j + \sum_{j=1}^{n} l_j \nabla \sigma_j'. \tag{5}$$

The first term in this formula is transformed to a form more expedient for calculation by
expressing the length l_j in terms of the distance ρ_j from the point of collision r_i to the
point of intersection of the zone boundaries of the photon trajectory $l_j = \rho_j - \rho_{j-1}$. The
result obtained is

$$\sum_{j=1}^{n} \sigma_j' \nabla l_j = \sum_{j=1}^{n-1} (\sigma_j' - \sigma_{j+1}') \nabla \rho_j + \sigma_n' \omega, \tag{6}$$

where the summation is taken over the intersecting zone boundaries. To calculate this sum,
it is necessary to determine not only the distance ρ_j for each point of intersection but
also the vector normal N_j of the zone boundary at these points in constructing the estimate
in the detector.

875

orthonormalized triad of vectors $\omega \perp a \perp g_j$ is constructed at the point of intersection of the j-th boundary (Fig. 1), as follows

$$a = [\omega N_j]/|[\omega N_j]|, \quad g_j = [\omega a]/|[\omega a]|.$$

$$(7)$$

Since the vector a belongs to plane Γ, which is tangential to the zone boundary and perpendicular to ω, small displacements of the detector position along this vector do not change the distance ρ_j. Displacement along ω also does not change ρ_j. Then $\nabla \rho_j$ coincides in direction with the vector

$$g_j = (\omega \lambda_j - N_j)/|\omega \lambda_j - N_j|.$$

$$(8)$$

The expression within the summation sign in Eq. (6) may now be completely determined since

$$\nabla \rho_j = \rho_j \sqrt{1 - \lambda_j^2}/\lambda_j|r^* - r_i|.$$

$$(9)$$

To calculate $\nabla \sigma'$ in Eq. (5), the following relation is used

$$\nabla \sigma' = \frac{d\sigma}{d\mu}(E') \nabla \mu$$

$$(10)$$

together with Eq. (3) for the gradient of the cosine of the scattering angle. The value of $d\sigma/d\mu$ as a function of the energy is calculated in advance on the basis of the constants of [2] and tabulated.

Analogously to the estimate in Eq. (2) for the gradient of the photon flux density, the estimate is constructed for the gradient of the photon energy flux density $\nabla \tau_i$, and also the gradient of the photon-radiation dose ∇D_i, taking into account that

$$\nabla I_i = E' \nabla F_i - F_i E'^2 \nabla \mu,$$
$$\nabla D_i = I_i \nabla \mu d\sigma_a/d\mu + \sigma_a \nabla I_i.$$

$$(11)$$

Here the calculation of the dose gradient requires tabulation of the derivatives of the energy absorption cross section $d\sigma_a/d\mu$.

Note, however, that the use of estimates in the form in Eqs. (2) and (11) is limited to the case when the detector is outside the scatterer, on account of the singularity of type ln r of the first term in the square brackets in Eq. (2).

As an illustration of the use of this algorithm, the results of calculating the flux density Φ of the scattered photon radiation and the corresponding gradient ∇Φ beyond an infinite plane two-layer barrier (aluminum and carbon; each layer is of thickness 0.5 d.s.p. with respect to the normal) are shown in Fig. 2. The energy of a point semiisotropic source of unit power at the barrier surface is 0.1 MeV. In Fig. 2a, an inclined line segment shows the projection of the gradient on the Z axis $\nabla_z \Phi$ calculated from the given algorithm for each value of Φ(z). The quantitative reliability criterion of these results may be taken to be coincidence of the theoretical values of $\nabla_z \Phi$ with $\partial \Phi/\partial z$, estimated from the set of points of Φ(z) obtained. This comparison is shown in Fig. 2b, where the approximate values of the derivative are obtained by plotting an approximating quadratic polynomial from three adjacent points. It is evident that both results coincide satisfactorily within the limits of statistical error of the calculation, and this confirms the effectiveness of the algorithm.

Including a calculation procedure for the gradient ∇Φ in the program increases the calculation time by approximately 30-35%. The relative statistical errors for ∇Φ are higher than for Φ, as a rule, and this difference increases as the detection point approaches the scatterer (barrier).

LITERATURE CITED

1. M. Kalos, "On the estimation of flux at a point by Monte Carlo," Nucl. Sci. Eng., 16, 111-117 (1963).
2. E. Storm and H. Israel, "Photon cross sections from 1 keV to 100 MeV for elements Z = 1 to Z = 100," Nucl. Data Tables, A7, 565-681 (1970).

CHANGING YOUR ADDRESS?

In order to receive your journal without interruption, please complete this change of address notice and forward to the Publisher, 60 days in advance, if possible.

(Please Print)

Old Address:

_____
name

_____

_____
address

_____
city

_____
state (or country)   zip code

New Address

_____
name

_____

_____
address

_____
city

_____
state (or country)   zip code

_____
date new address effective

_____
name of journal

THE LANGUAGE OF SCIENCE

Plenum
PUBLISHING CORPORATION

233 Spring Street, New York, New York 10013

How To Comply With The New Copyright Law

RUSSIAN JOURNALS IN THE PHYSICAL AND MATHEMATICAL SCIENCES

AVAILABLE IN ENGLISH TRANSLATION

ALGEBRA AND LOGIC
Algebra i Logika
Vol. 23, 1984 (6 issues) $360

ASTROPHYSICS
Astrofizika
Vol. 20, 1984 (4 issues) $420

AUTOMATION AND REMOTE CONTROL
Avtomatika i Telemekhanika
Vol. 45, 1984 (24 issues) $625

COMBUSTION, EXPLOSION, AND SHOCK WAVES
Fizika Goreniya i Vzryva
Vol. 20, 1984 (6 issues) $445

COSMIC RESEARCH
Kosmicheskie Issledovaniya
Vol. 22, 1984 (6 issues) $545

CYBERNETICS
Kibernetika
Vol. 20, 1984 (6 issues) $445

DIFFERENTIAL EQUATIONS
Differentsial'nye Uravneniya
Vol. 20, 1984 (12 issues) $505

DOKLADY BIOPHYSICS
Doklady Akademii Nauk SSSR
Vols. 274-279, 1984 (2 issues) $145

FLUID DYNAMICS
Izvestiya Akademii Nauk SSSR,
Mekhanika Zhidkosti i Gaza
Vol. 19, 1984 (6 issues) $500

FUNCTIONAL ANALYSIS AND ITS APPLICATIONS
Funktsional'nyi Analiz i Ego Prilozheniya
Vol. 18, 1984 (4 issues) $410

GLASS AND CERAMICS
Steklo i Keramika
Vol. 41, 1984 (6 issues) $590

HIGH TEMPERATURE
Teplofizika Vysokikh Temperatur
Vol. 22, 1984 (6 issues) $520

HYDROTECHNICAL CONSTRUCTION
Gidrotekhnicheskoe Stroitel'stvo
Vol. 18, 1984 (12 issues) $385

INDUSTRIAL LABORATORY
Zavodskaya Laboratoriya
Vol. 50, 1984 (12 issues) $520

INSTRUMENTS AND EXPERIMENTAL TECHNIQUES
Pribory i Tekhnika Éksperimenta
Vol. 27, 1984 (12 issues) $590

JOURNAL OF APPLIED MECHANICS AND TECHNICAL PHYSICS
Zhurnal Prikladnoi Mekhaniki i Tekhnicheskoi Fiziki
Vol. 25, 1984 (6 issues) $540

JOURNAL OF APPLIED SPECTROSCOPY
Zhurnal Prikladnoi Spektroskopii
Vols. 40-41, 1984 (12 issues) $540

JOURNAL OF ENGINEERING PHYSICS
Inzhenerno-fizicheskii Zhurnal
Vols. 46-47, 1984 (12 issues) $540

JOURNAL OF SOVIET LASER RESEARCH
A translation of articles based on the best Soviet research in the field of lasers
Vol. 5, 1984 (6 issues) $180

JOURNAL OF SOVIET MATHEMATICS
A translation of Itogi Nauki i Tekhniki and Zapiski
Nauchnykh Seminarov Leningradskogo Otdeleniya
Matematicheskogo Instituta im. V. A. Steklova AN SSSR
Vols. 24-27, 1984 (24 issues) $1035

LITHOLOGY AND MINERAL RESOURCES
Litologiya i Poleznye Iskopaemye
Vol. 19, 1984 (6 issues) $540

LITHUANIAN MATHEMATICAL JOURNAL
Litovskii Matematicheskii Sbornik
Vol. 24, 1984 (4 issues) $255

MAGNETOHYDRODYNAMICS
Magnitnaya Gidrodinamika
Vol. 20, 1984 (4 issues) $415

MATHEMATICAL NOTES
Matematicheskie Zametki
Vols. 35-36, 1984 (12 issues) $520